ETH zürich

Master Thesis

Design and characterization of a two sample setup for photon shaping

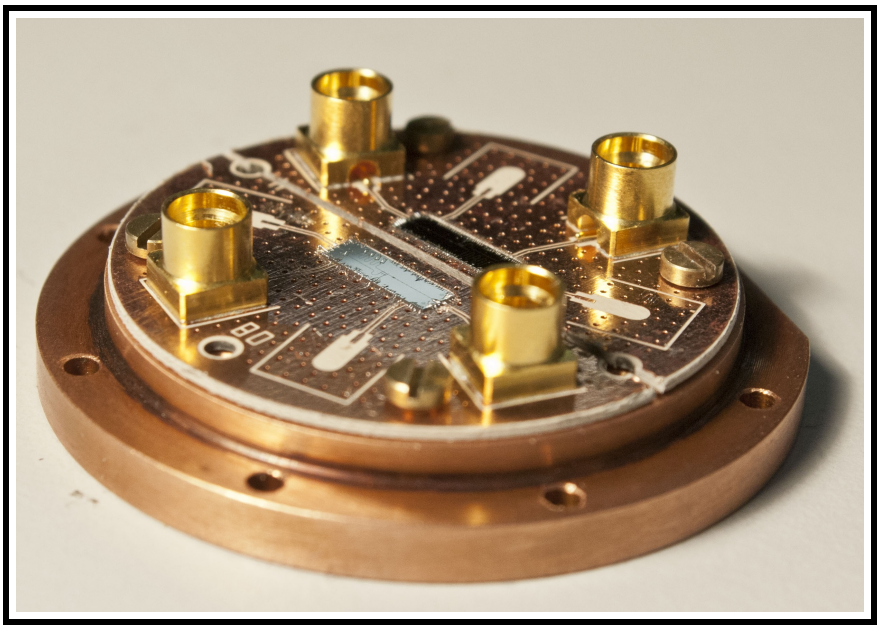

Department of Physics
Laboratory for Solid State Physics
Quantum Device Lab
March 28, 2014

Author
Lukas Huthmacher

Supervisor
Marek Pechal

Principal Investigator
Prof. Dr. Andreas Wallraff

Abstract

One of the most challenging problems in quantum communication is the reliable quantum state transfer between distant nodes of a network. As it turns out, photons serve well for transmitting quantum states over large distances. It is therefore necessary to find a way to control the interactions between light and matter to map quantum states from a solid state system to a single photon and vice versa [1]. In this work we present a setup for realizing efficient quantum state transfer in a CQED system consisting of two samples connected by a one-way coaxial cable link. Besides the development and characterization we introduce a method for photon shaping using a microwave-induced tunable second-order coupling between qubit and resonator. We use simulations to show that we can theoretically reach 90.5 % of state transfer efficiency within our setup. Finally we show that we can shape single photons using the described method as well as an alternative first-order coupling scheme. The results show that the setup allows for the realization of quantum state transfer between the two samples.

Contents

1 Introduction

In 1981 Richard P. Feynman gave a talk at the First Conference on the Physics of Computation at MIT, stating that it is not possible to simulate arbitrary quantum mechanical systems efficiently using classical computers [2]. Instead he proposed to use quantum phenomena to build a computer capable of performing simulations of such systems, giving a first idea of a simple quantum computer.

Only a few years later David Deutsch presented the concept of a universal quantum computer which can not only simulate the classical Turing machine, but also any arbitrary quantum computer [3]. He also gave a first example of a simple algorithm which is more efficient than the corresponding algorithm for a classical computer, using the fact that a quantum bit (qubit) in contrast to a classical bit can not only exist in the state zero or one but in any arbitrary superposition of these to states. This so-called Deutsch algorithm determines whether a function acting on one bit is constant or balanced.

Based on these theoretical foundations several algorithms were developed in the following years, which solve specific problems more efficiently than any known classical algorithm. For example the Deutsch-Jozsa algorithm [4], which is a multidimensional version of the Deutsch algorithm presented in [3] or Grover's algorithm for searching unstructured databases, leading to a quadratic speedup compared to the best classical algorithm [5].

The most famous example is Shor's factorization algorithm, providing a method to efficiently factorize integers [6]. It offers an exponential speedup in comparison to any known classical algorithm, affecting the security of today's public-key cryptography, since state of the art encryption schemes like RSA are based on the difficulty of factorizing large numbers [7].

Fortunately there are also quantum cryptography protocols which offer secure key distribution over public quantum channels, like the BB84 [8] or the E91 protocol [9].

Other important steps for quantum communication were the proposal of super dense coding by C. H. Bennett and S. J. Wiesner, which provides the ability to send two bits of classical information using only one quantum channel [10], as well as the quantum teleportation protocol [11].

For the physical realization of a quantum computer a system needs to fulfill the five so-called DiVincenzo criteria plus two additional ones regarding the possibility to transmit information, given by [12]:

1. A scalable physical system with well characterized qubits
2. The ability to initialize the state of the qubits
3. Long relevant decoherence times with respect to the gate operation time
4. A universal set of quantum gates
5. A qubit-specific measurement capability
6. The ability to interconvert stationary and flying qubits
7. The ability to faithfully transmit flying qubits between specified locations

Several candidates for the physical realization of such systems have been proposed and investigated during the last decades including trapped ions [13], photons [14], nuclear spins in molecules [15], quantum dots [16], and superconducting circuits [17].

In analogy to cavity quantum electrodynamics (QED), where a system of an atom interacting with a cavity-field is analyzed [18], the Quantum Device Lab at the ETH Zurich focuses on superconducting qubits coupled to a transmission line resonator. In this case the superconducting qubit can be seen as a tunable artificial atom and the transmission line resonator acts as the cavity. This so-called Circuit QED offers a nice controllable system, which allows to manipulate, selectively read-out and couple qubits using photons in the resonator [19–22].

One other important aspect of Circuit QED is the fact that it gives rise to the possibility of quantum state transfer between distant nodes, which is crucial for realizing quantum networks [1]. Thanks to the strong coupling of the qubit to the microwave filed in the resonator which in turn can be coupled efficiently to propagating modes in a coaxial cable, we have a natural way of transferring the state of the stationary two level system into a flying qubit, which enables fast state transfer.

Using shaped photons is one possibility for highly efficient state transfer between distant nodes in a quantum network [23]. The basic idea is to use a photon wavepacket with a symmetric time shape to achieve high absorption rates due to time-reversal symmetry of the process.

In this Thesis a possible way for shaping such photons is discussed with the goal of realizing an experiment, where a photon is shaped and emitted in one sample and subsequently reabsorbed in a second sample. After a basic description of the principles of superconducting qubits and circuit QED in Section 2, the photon shaping method used in this thesis will be discussed in Section 3. In the following the measurement setup along with some theoretical estimations of the system dealt with is presented in Section 4, where we also briefly summarize reflection measurements. After a short summary of the sample design used in this experiments together with some lifetime estimations in Section 5 we look at numerical simulations of the carried out experiments, giving an idea about expected results (Sec. 6). Finally in Section 7 the experiments and their results are discussed.

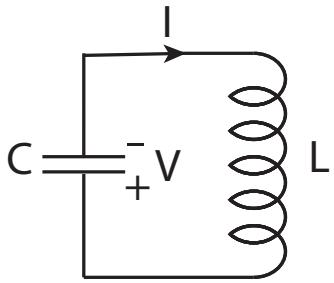

Figure 1: Circuit diagram of a LC oscillator.

2 Superconducting qubits and Circuit QED

2.1 Superconducting qubits

Superconducting qubits are electronic circuits made out of superconducting materials and therefore have greatly reduced losses due to electrical resistances. Superconductivity is a phase where the electrons feel an attractive interaction due to virtual phonons which is stronger than the Coulomb repulsion [26], leading to states formed by bosonic electron pairs, so-called Cooper pairs.

To excite a Cooper pair a certain minimal energy is needed. If this energy is higher than the thermal energy of the ion lattice in the conductor, the Cooper pairs cannot be scattered by the lattice and thus flow without dissipating energy. This corresponds to a perfect conductor with zero electrical resistance. As the thermal energy needs to be very low, the second order phase transition into the superconducting state usually occurs only close to the absolute zero point (0 K).

To understand how superconducting electronic circuits can form artificial atoms we first review the basic properties of electronic harmonic oscillators.

2.1.1 Electronic harmonic oscillator

A conventional electronic LC oscillator consists of two basic elements: capacitor and inductor (see Fig. 1). This system is characterized by the charge on the capacitor $Q = C\,V$ and the flux $\Phi = L\,I$ through the inductor, which are linked by the equations of motion $\dot{Q} = I$ and $\dot{\Phi} = -V$. These can be described as Hamilton's equations from the Hamiltonian

$$H = H_{el} + H_{mag} = \frac{CV^2}{2} + \frac{LI^2}{2} = \frac{Q^2}{2C} + \frac{\Phi^2}{2L}, \tag{1}$$

by taking Q and Φ as the canonical conjugate variables.

Comparing this Hamiltonian with the Hamiltonian of the mechanical harmonic oscillator, the Capacitance C can be regarded as a 'mass', which is moving in a potential of curvature $\frac{1}{L}$, or the other way around. Using this analogy one defines the quantum mechanical operators as

$$\hat{\Phi} = \Phi, \qquad \hat{Q} = -i\hbar\frac{\partial}{\partial\Phi}. \tag{2}$$

These fulfill the following commutation relation

$$[\hat{\Phi}, \hat{Q}] = i\hbar. \tag{3}$$

Therefore, the Hamilton operator of the system is given by

$$\hat{H} = \frac{\hat{Q}^2}{2C} + \frac{\hat{\Phi}^2}{2L} = -\frac{\hbar^2}{2C}\frac{\partial^2}{\partial\Phi^2} + \frac{1}{2L}\Phi^2. \tag{4}$$

Using creation and annihilation operators one gets the well known expression for a harmonic oscillator

$$\hat{H} = \hbar\omega\left(\hat{a}^\dagger\hat{a} + \frac{1}{2}\right), \tag{5}$$

with $\omega = \frac{1}{\sqrt{LC}}$ being the resonance frequency and the creation and annihilation operators given by

$$\begin{aligned} \hat{a}^\dagger &= \frac{1}{\sqrt{2\hbar Z_C}}\left(Z_C\hat{Q} + i\hat{\Phi}\right), \\ \hat{a} &= \frac{1}{\sqrt{2\hbar Z_C}}\left(Z_C\hat{Q} - i\hat{\Phi}\right), \end{aligned} \tag{6}$$

where $Z_C = \sqrt{\frac{L}{C}}$ denotes the characteristic impedance of the oscillator.

In the end individual control of each energy level as well as the corresponding transitions is needed. This means that the electronic harmonic oscillator as such is not sufficient for building a artificial atom, as it only provides equally spaced energy levels. Therefore, an anharmonicity in the energy level spacing is required. This can be realized by introducing a loss free, non-linear inductance to the system using a so-called Josephson junction.

2.1.2 Josephson Junction

A Josephson junction consists of two superconducting layers that are separated by a small insulating layer, which provides a weak coupling between the former ones. In 1962 B.D. Josephson theoretically predicted that Cooper pairs can tunnel through this barrier and thus produce a supercurrent through the junction [24]. There are two equations describing the dynamics of this so-called Josephson effect [25]

$$I = I_0 \sin\delta, \tag{7}$$

$$V = \frac{\Phi_0}{2\pi}\dot{\delta}. \tag{8}$$

Where $\delta = \delta_2 - \delta_1$ denotes the phase difference between the two superconductors which can also be regarded as a normalized magnetic flux $\delta = 2\pi\frac{\Phi}{\Phi_0}$. Here, $\Phi_0 = \frac{h}{2e}$ denotes the flux quantum and I_0 is the critical current of the junction. If a current $I > I_0$ is applied to the junction also single electrons start to tunnel through the barrier and a voltage drop over the junction occurs.

In combination with the induction law these equations show that the Josephson junction acts as a non-linear inductor, where the Josephson inductance is given by

$$L_J = \frac{V}{\dot{I}} = \frac{\Phi_0}{2\pi I_0}\frac{1}{\cos\delta} \equiv L_{J0}\frac{1}{\cos\delta}, \tag{9}$$

L_{J0} denoting the specific Josephson inductance.

Integrating VI over time gives the (specific) Josephson energy

$$E_J = \int VIdt = \frac{\Phi_0 I_0}{2\pi}\cos\delta \equiv E_{J0}\cos\delta. \tag{10}$$

2.1.3 Qubit types

The combination of the loss free, non-linear inductance with an electronic harmonic oscillator gives rise to a energy level spectrum with different transition frequencies between the various energy levels, as required for realizing an artificial atom.

Besides the non-linear inductance, a Josephson junction also provides a capacitance C_j which can be used in designing the qubits. This leads to various possibilities for circuits that can be used as a qubit. One can distinguish three basic designs [27] (Fig.2):

Phase qubit The Phase qubit consists of a Josephson junction biased by a current source. The bias current is chosen to be close to the critical current I_0 leading to a large non-linearity in the inductance of the Josephson junction. Here, the potential is defined by the phase difference δ between the two parts of the junction and the conjugate variable is given by the charge on the capacitance C_j. This leads to a so-called washboard potential, which is tilted according to the ratio I/I_0. In the wells of this potential non-degenerate energy levels can be found, defining the qubit.

Flux qubit In the flux qubit design both sides of the Josephson junction are connected via a superconducting wire acting as a inductor and thus forming a superconducting loop. To bias the qubit an external flux is applied using another inductance, implementing a transformer. In this system the free parameters are the flux Φ through the superconducting loop and the charge Q on the capacitance C_j. The qubit is operated in a region where the potential has two degenerate wells, using the symmetric and anti symmetric combination of the wavefunctions in these wells.

Charge qubit The charge qubit consists of a Josephson junction in series with a capacitor and is biased by a voltage. The capacitance C_j of the junction together with the capacitor define a so-called island where the number of charges N_g on the capacitor can be varied using the bias voltage. This design is also called Cooper pair box and will be discussed in more detail in the following, as the currently used design in the Quantum Device Lab is a modification of this version.

2.1.4 Cooper pair box

The Cooper pair box as shown in Figure 3 consists of an island which is coupled to a reservoir of charges through the Josephson junction. As mentioned, this design allows to store Cooper pairs on the island and the physics is the same as for a particle in a box potential.

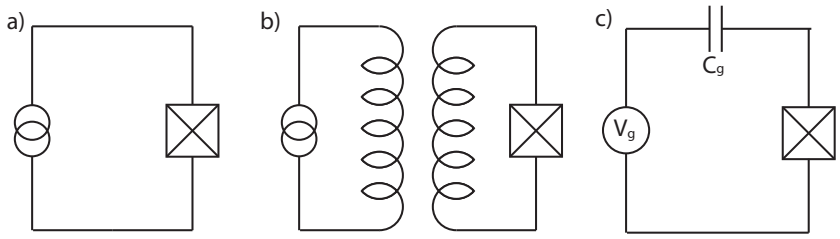

Figure 2: The basic types of superconducting qubits: a) the current biased phase qubit, b)the flux biased flux qubit and c) the charge biased charge qubit.

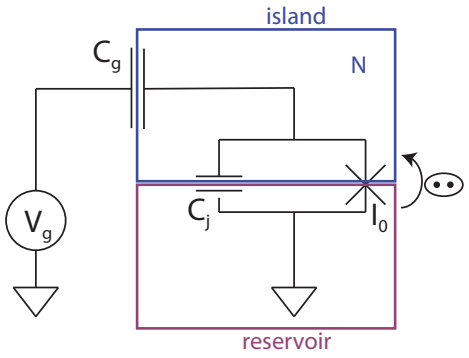

Figure 3: Schematic drawing of the Cooper pair box.

The number of Cooper pairs on the island with respect to charge neutrality is a discrete variable which is given by

$$N = \frac{Q}{2e}. \tag{11}$$

By varying the voltage V_g applied to the gate Capacitor C_g one can change the polarization charge on the gate capacitor N_g, which is in contrast to N a continuous variable given by

$$N_g = \frac{C_g V_g}{2e}. \tag{12}$$

The electrostatic energy in such a system is given by

$$H_{el} = \frac{(2e)^2(N - N_g)^2}{2C_\Sigma} = 4E_C(N - N_g)^2, \tag{13}$$

where $C_\Sigma = C_j + C_g$ denotes the total capacitance of the island and $E_C = \frac{e^2}{2C_\Sigma}$ denotes the charging energy. The corresponding first four energy levels can be seen in Fig. 4a).

By raising V_g from $N_g = 0$ a degeneracy at $N_g = 1/2$ is reached and a Cooper pair will tunnel from the reservoir onto the island to minimize the energy of the system. Thus it is possible to alter N by varying N_g.

In addition to the electrostatic energy there is also a magnetic term corresponding to the Josephson energy given in Eq. (10).

$$H_{mag} = -E_{J0}\cos\delta \approx -\frac{\Phi_0 I_0}{2\pi}\left(1 - \frac{1}{2}\left(\frac{\Phi}{\Phi_0}2\pi\right)^2 + ...\right) \approx \frac{1}{2}\frac{\Phi^2}{L_{J0}}. \tag{14}$$

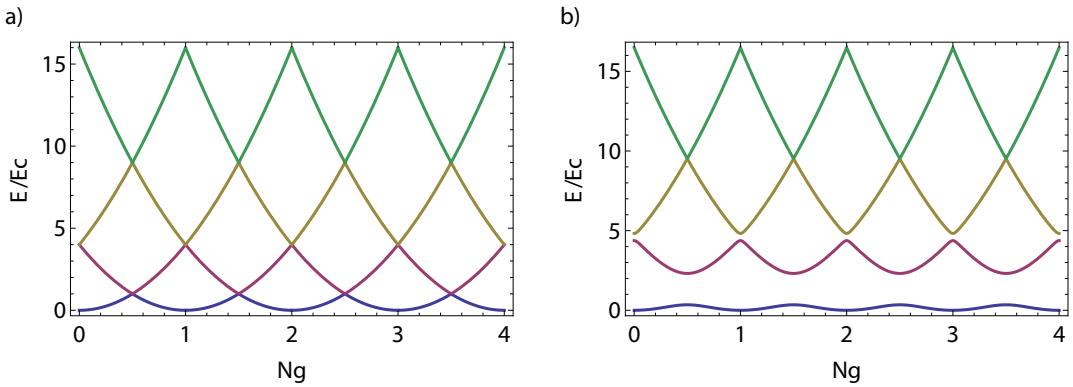

Figure 4: The first four energy levels for a) E_J=0 and b) $E_J/E_C = 10$.

This leads to the Cooper pair box Hamilton operator

$$\hat{H} = E_C \left(\hat{N} - N_g\right)^2 - E_{J0} \cos\hat{\delta}, \tag{15}$$

with

$$\left[\hat{\delta}, \hat{N}\right] = i. \tag{16}$$

Noting that the cosine can be written as

$$\cos\hat{\delta} = \frac{1}{2}\left(e^{i\hat{\delta}} + e^{-i\hat{\delta}}\right) \tag{17}$$

and using the basis transformation

$$|\delta\rangle = \frac{1}{\sqrt{2\pi}} \sum_N e^{iN\delta} |N\rangle \tag{18}$$

we find that this operator acts on a number state as

$$e^{\pm i\hat{\delta}} |N\rangle = |N \mp 1\rangle . \tag{19}$$

This allows us to write the Hamilton operator in the number basis

$$\hat{H} = \sum_N \left(E_C (N - N_g)^2 |N\rangle \langle N| - \frac{E_{J0}}{2} (|N\rangle \langle N+1| + |N+1\rangle \langle N|) \right). \tag{20}$$

Equivalently the Hamilton operator can be written in the phase basis using

$$\hat{N} = \frac{\hat{Q}}{2e} = -i\hbar \frac{1}{2e} \frac{\partial}{\partial\hat{\phi}} = -i \frac{\partial}{\partial\hat{\delta}}, \tag{21}$$

leading to

$$\hat{H} = E_C \left(-i\frac{\partial}{\partial\hat{\delta}} - N_g\right)^2 - E_{J0} \cos\hat{\delta}. \tag{22}$$

In this basis it is possible to solve for the exact solution of the Schroedinger equation, where the energy eigenstates $\Psi_n(\delta) = \langle\delta|\Psi_n\rangle$ are given by Mathieu functions.

The Hamilton operator of the Cooper pair box shows, that the Josephson coupling lifts the degeneracy between the energy levels as presented in Fig. 4b), the separation scales proportional to E_J. This gives the required tunable atom and the two lowest states can be used to define qubit ground and excited state.

To make the artificial atom even more flexible, we can go one step further by using a superconducting quantum interference device (SQUID) loop, which means to connect two Josephson junctions in parallel. This gives rise to the advantage that the phase difference is tunable by applying an external magnetic field, allowing to tune the Josephson energy and thus the energy splitting. The tunable Josephson energy is given by

$$E_J = E_J^{max} \left| \cos\left(\pi \frac{\Phi_{ext}}{\Phi_0} \right) \right|, \tag{23}$$

where Φ_{ext} is the flux through the SQUID loop due to the applied external magnetic field.

Two state approximation It is sometimes convenient to consider only the two state approximation for the Cooper pair box, as the first two levels define our qubit. In order to do so we substitute the operators in Eq. (15) by

$$\hat{N} = \begin{pmatrix} 0 & 0 \\ 0 & 1 \end{pmatrix} = \frac{1 - \hat{\sigma}_z}{2}, \tag{24}$$

$$\cos\hat{\delta} = \frac{\hat{\sigma}_x}{2}. \tag{25}$$

Neglecting the term only dependent on N_g the Hamilton operator in this approximation is given by

$$\hat{H} = -\frac{E_C}{2}(1 - 2N_g)\hat{\sigma}_z - \frac{E_J}{2}\hat{\sigma}_x \tag{26}$$

and one gets an avoided crossing between the two states (Fig. 5).

The Energy level diagrams of the Cooper pair box show that it is quite sensitive to fluctuations in the gate voltage, or equivalently in the number of charges N_g on the gate capacitor. In experiments this leads to dephasing as the energy difference between the different states strongly depends on the continuous variable N_g. For specific gate voltages, leading to $N_g = 0.5 + n,\ n \in \mathbb{Z}$, the energy levels have a zero slope, meaning that linear noise in the gate voltage cannot lead to dephasing in this so-called sweet spot.

However the system can still be perturbed by higher order noise, which could drive the qubit away from the sweet spot, resulting in dephasing of the qubit states. To minimize the effect of such fluctuations one has to reduce the charge dispersion by modifications of the qubit design.

2.1.5 Transmon qubit

The strength of the modulation of a single energy level by changes in the offset charge N_g depends on the ratio between Josephson and charging energy. The idea of the transmon design is to lower the charging energy compared to the Josephson energy by introducing a large capacitance in parallel to the SQUID loop [28] (Fig. 6).

This effectively flattens out the energy level dependence on N_g (Fig. 7) and the spacing between the first two levels can be approximated by [28]

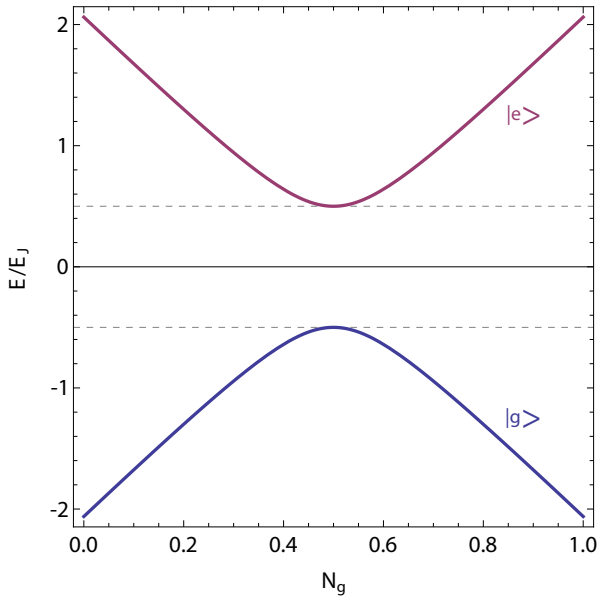

Figure 5: Ground (blue) and excited (red) state of the qubit in the two state approximation ($E_C/E_J = 4$).

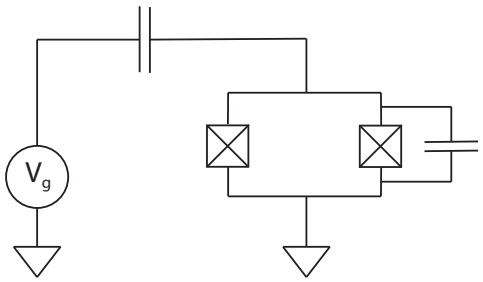

Figure 6: In the transmon design an additional capacitance lowers the charging energy to get rid of charge noise.

$$E_{01} \approx \sqrt{8E_J E_C} - E_C. \tag{27}$$

Unfortunately this comes for the price of the anharmonicity being reduced ($|E_{01} - E_{12}| \ll E_{01}$). This makes it harder to address specific transitions individually, which is important for manipulating the qubit.

The peak-to-peak charge dispersion ϵ_m and the relative anharmonicity α_r are defined as [28]

$$\epsilon_m = E_m(N_g = 1) - E_m(N_g = 0.5), \tag{28}$$

$$\alpha_r = \frac{E_{12} - E_{01}}{E_{01}}, \tag{29}$$

where $E_n(N_g)$ denotes the energy of level n at N_g starting from $n = 0$ for the ground state and $E_{n,n+1}$ gives the energy difference between the levels n and $n + 1$ at $N_g = 0.5$. Nevertheless it is possible to find a regime were the influence of voltage fluctuations

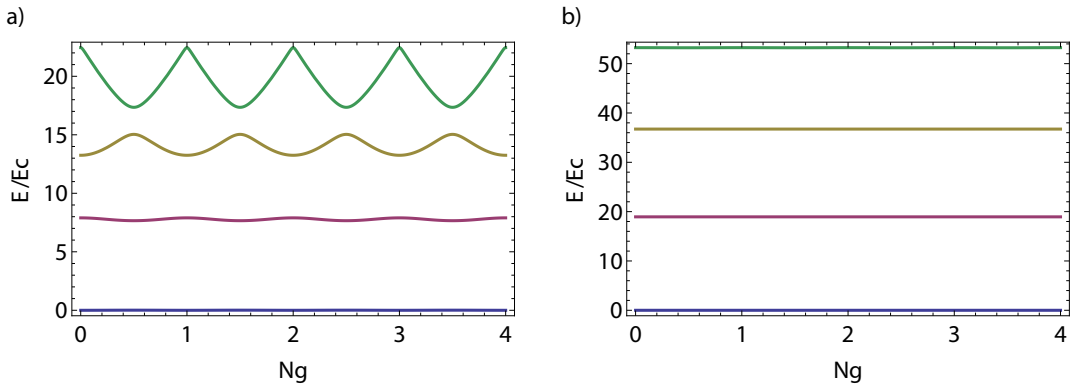

Figure 7: The first four energy levels of the transmon qubit for a) $E_J/E_C = 10$ and b) $E_J/E_C = 50$.

is significantly reduced but the anharmonicity is still high enough to adress individual transitions, as illustrated in Fig. 8.

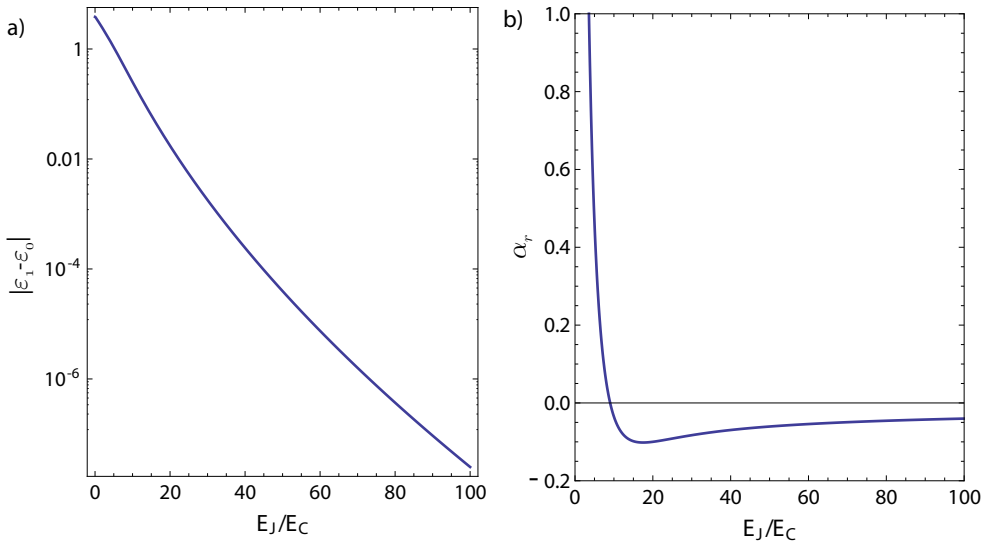

Figure 8: a) The dependency of the charge dispersion between the ground and the excited state on E_J, determining the dephasing of a $|g\rangle + |e\rangle$ superposition state. b) The relative anharmonicity with respect to E_J/E_C at $N_g = 0.5$.

2.1.6 Driving the qubit

By applying microwave pulses of controllable amplitude, length and phase to the qubit it is possible to control the qubit state. In terms of the Hamiltonian (Eq. (26)) this means to couple a voltage to the gate capacitor, which can be described by substituting $N_g = N_g^0 + N_g(t)$, where $N_g(t)$ describes the applied drive. For simplicity we assume $N_g^0 = 1/2$ and $N_g(t) = A\cos(\omega_d t + \phi)$, thus the Hamiltonian is given by

$$\hat{H} = \hbar\Omega\cos(\omega_d t + \phi)\hat{\sigma}_z - \frac{\hbar}{2}\omega_q\hat{\sigma}_x, \tag{30}$$

where $\Omega = E_C A$ gives the drive strength and ω_q is the qubit frequency. Transforming $\hat{H}$ into the eigenbasis $\{|0\rangle + |1\rangle\,, |0\rangle - |1\rangle\}$ of the non-driven Hamiltonian (applying a $\pi/2$ rotation around the y-axis) leads to

$$\hat{H} = \hbar\Omega \cos(\omega_d t + \phi)\hat{\sigma}_x + \frac{\hbar}{2}\omega_q \hat{\sigma}_z. \tag{31}$$

Using the unitary transformation $\hat{U} = e^{i\frac{\omega t}{2}\hat{\sigma}_z}$ we can go into the reference frame rotating at frequency ω, by using

$$\hat{H}_r = \hat{U}\hat{H}\hat{U}^\dagger + i\hbar\frac{\mathrm{d}\hat{U}}{\mathrm{d}t}\hat{U}^\dagger. \tag{32}$$

Choosing $\omega = \omega_d$ now allows to see how the qubit state changes relative to the applied field. In the rotating frame the Hamiltonian is given by

$$\begin{aligned}\hat{H}_r &= \frac{\hbar}{2}\Omega\left(\cos\phi\,\hat{\sigma}_x + \sin\phi\,\hat{\sigma}_y\right) + \frac{\hbar}{2}(\omega_q - \omega_d) \\ &= \frac{\hbar}{2}\vec{M}\cdot\vec{\sigma},\end{aligned} \tag{33}$$

with $\vec{M} = (\Omega\cos\phi, \Omega\sin\phi, \omega_q - \omega_d) \equiv (\Omega_x, \Omega_y, \omega_q - \omega_d)$. Thus we can induce rotations about all axes using phase, amplitude and frequency of the applied drive.

2.2 Circuit QED

In quantum optics the studies of interactions between atoms and electromagnetic fields in high quality cavities, so-called cavity QED, lead to observation of various phenomena and also to applications in quantum information processing [18].

As the interaction strength between an atom and the free space vacuum field is weak, the idea of caity QED is to reduce the mode volume and therefore increase the field strength by placing the atom inside a high quality cavity. This leads to an altered spontaneous emission rate of the atom as the cavity supports only a discrete number of modes. If the resonance frequency of the cavity is far detuned from the transition frequency of the atom the spontaneous emission is inhibited [29], whereas if the cavity is on resonance with the atom the spontaneous emission is enhanced by the Purcell effect [30]. Besides this, the vacuum fluctuations inside the cavity also induce a shifting of the atomic levels known as the Lamb shift [31].

The idea of realizing a cavity QED system on a chip, using the qubit as an artificial atom and a one-dimensional transmission line resonator was proposed in 2004 [19] and has first been realized by A. Wallraff et al. [20] in Yale.

2.2.1 Jaynes-Cummings Hammiltonian

In circuit QED photons are coupled to the qubits by connecting the qubit to a coplanar transmission line resonator. Such a transmission line resonator can be realized in an on chip architecture and approximately be treated as a one-dimensional resonator. In the picture of lumped elements one deals with a chain of infinitesimally small capacitances and inductances, which can be approximated by a simple LC circuit, if the system is

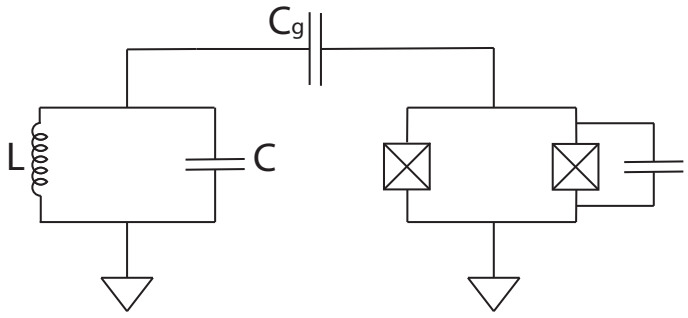

Figure 9: A transmon capacitively coupled to a harmonic oscillator.

considered to be close to resonance. This approximation is justified as later only systems where the qubit is far detuned from all but one mode of the resonator are considered.

If the qubit is now capacitivly coupled to the resonator (Fig. 9) the Hamiltonian of the system can be approximated by

$$\hat{H} = \frac{\hat{Q}^2}{2C} + \frac{\hat{\Phi}^2}{2L} - \frac{E_C}{2}(1 - 2(N_g + N_g^{qm}))\hat{\sigma}_x - \frac{E_J}{2}\hat{\sigma}_z, \tag{34}$$

where N_g^{qm} denotes the quantum fluctuations of charge on the gate capacitor. The first two terms describe the harmonic oscillator approximated by the total capacitance C and the total inductance L and the other two are given by the two state approximation of the qubit (Eq. (26)).

We can express the quantum fluctuations of the charge on the gate capacitor by writing $\hat{V} = \hat{Q}/C$ in terms of the creation and annihilation operators (Eq. (6)), which gives

$$N_g^{qm} = \frac{C_g}{2e}\hat{V}^{qm} = \frac{C_g}{2e}\sqrt{\frac{\hbar\omega_r}{2C}}(\hat{a}^\dagger + \hat{a}). \tag{35}$$

Now choosing $N_g = \frac{1}{2}$ leads to

$$\hat{H} = \hbar\omega_r\left(\hat{a}^\dagger\hat{a} + \frac{1}{2}\right) + \frac{E_C}{2}\frac{C_g}{e}\sqrt{\frac{\hbar\omega_r}{2C}}(\hat{a}^\dagger + \hat{a})\hat{\sigma}_x + \frac{E_J}{2}\hat{\sigma}_z, \tag{36}$$

where we now introduce the qubit raising and lowering operators $\hat{\sigma}^+$ and $\hat{\sigma}^-$, defined as

$$\hat{\sigma}^+ |g\rangle = |e\rangle\,, \qquad \hat{\sigma}^- |e\rangle = |g\rangle\,, \qquad \hat{\sigma}_x = (\hat{\sigma}^+ + \hat{\sigma}^-). \tag{37}$$

Using the new operators and applying the rotating wave approximation where high frequency oscillations are neglected, we end up with the full Hamiltonian

$$\hat{H} = \hbar\omega_r\left(\hat{a}^\dagger\hat{a} + \frac{1}{2}\right) + \hbar g\left(\hat{a}^\dagger\hat{\sigma}^- + \hat{a}\hat{\sigma}^+\right) + \frac{\hbar}{2}\omega_q\hat{\sigma}_z, \tag{38}$$

with coupling constant $\hbar g = \frac{C_g}{C_\Sigma}e\sqrt{\frac{\hbar\omega_r}{2C}}$ and qubit frequency $\omega_q = E_J/\hbar$.

In this context applying the rotating wave approximation removes terms which do not conserve the total number of excitations, meaning they would either excite or destroy excitations in both the qubit and the resonator. This approximation holds as long as $|\omega_r - \omega_q| \ll \omega_r + \omega_q$ and $g \ll \omega_r, \omega_q$.

Considering a transmon qubit the two state approximation is no longer sufficient and one has to take higher levels into account. In this case the Jaynes-Cummings Hamiltonian is given by [28]

$$\hat{H} = \hbar \sum_i \omega_i \left|i\right\rangle \left\langle i\right| + \hbar\omega_r \hat{a}^\dagger \hat{a} + \hbar \sum_i g_{i,i+1} \left(\left|i\right\rangle \left\langle i+1\right| \hat{a}^\dagger + h.c. \right), \tag{39}$$

now written in the basis of the uncoupled transmon states $|i\rangle$.

The interaction term of the Hamiltonian shows that we can swap excitations between resonator and qubit states, if the system is in the strong coupling limit $g \gg \kappa, \gamma$ where the coupling is much stronger than the photon decay rate κ and the decay rate of the qubit γ. In this case the two subsystems cannot be seen as individual systems anymore but hybridize and form so-called dressed states. This can be seen by diagonalizing the Jaynes-Cummings Hamiltonian in the two state approximation, where it has an analytic solution. The interaction term only couples the states $|e, n\rangle$, $|g, n+1\rangle$ such that the Hamiltonian (Eq. (38)) can be written in this basis, given by the matrix

$$\begin{pmatrix} \frac{\hbar}{2}(\omega_r(2n+1)+\omega_q) & \hbar g\sqrt{n+1} \\ \hbar g\sqrt{n+1} & \frac{\hbar}{2}(\omega_r(2(n+1)+1)-\omega_q) \end{pmatrix}, \tag{40}$$

which has the eigenvalues

$$E_{1/2} = \hbar\omega_r(n+1) \pm \frac{\hbar}{2}\sqrt{\Delta^2 + 4g^2(n+1)}, \tag{41}$$

where $\Delta = \omega_q - \omega_r$. The corresponding eigenvectors are then given by

$$\begin{aligned} |-, n\rangle &= \sin\theta_n \left|e, n\right\rangle + \cos\theta_n \left|g, n+1\right\rangle, \\ |+, n\rangle &= \cos\theta_n \left|e, n\right\rangle - \sin\theta_n \left|g, n+1\right\rangle, \end{aligned} \tag{42}$$

where

$$\tan\theta_n = \frac{2g\sqrt{n+1}}{\sqrt{\Delta^2 + 4g^2(n+1)} + \Delta}. \tag{43}$$

In the special case that the qubit and the resonator are on resonance $\Delta \approx 0$ these two eigenstates reduce to

$$\begin{aligned} |-, n\rangle &= \frac{1}{\sqrt{2}} \left(\left|e, n\right\rangle + \left|g, n+1\right\rangle \right), \\ |+, n\rangle &= \frac{1}{\sqrt{2}} \left(\left|e, n\right\rangle - \left|g, n+1\right\rangle \right). \end{aligned} \tag{44}$$

These so-called polariton states which are separated by $2\hbar g\sqrt{n+1}$ (see Fig. 10a)) can experimentally be seen in a resonant vacuum Rabi mode splitting [32].

2.2.2 Dispersive regime

In the case where the qubit is far detuned from the resonator, such that $g \ll |\Delta|$, we are in the dispersive limit. In that case excitations cannot be exchanged between the qubit

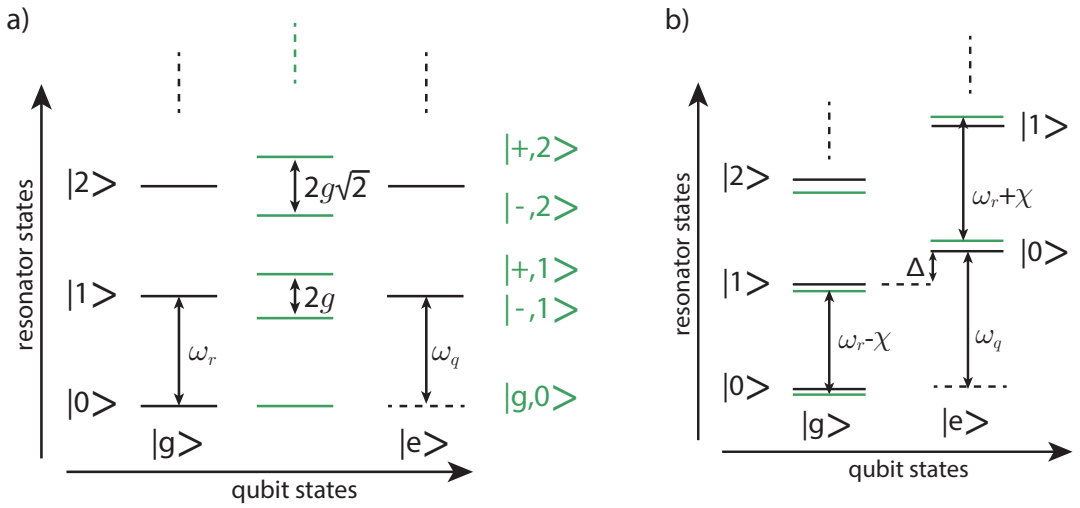

Figure 10: The bare (black) and dressed (green) states of the Jaynes-Cummings ladder a) for $\Delta = 0$, where we can observe vacuum rabi oscillations and the formation of polariton states and b) for $g \ll |\Delta|$ where the corresponding energy levels are shifted with respect to the qubit state.

and the resonator but the energy levels are subject to a shift dependent on the state of qubit or resonator, respectively. The Hamiltonian for such a decoupled system can be approximated by [19]

$$\hat{H} \approx \hbar \left(\omega_r + \frac{g^2}{\Delta} \hat{\sigma}_z \right) \hat{a}^\dagger \hat{a} + \frac{\hbar}{2} \left(\omega_q + \frac{g^2}{\Delta} \right) \hat{\sigma}_z. \tag{45}$$

The second term in this expression shows that the qubit transition frequency is shifted $\tilde{\omega}_q = \omega_q + \frac{g^2}{\Delta}$, which is due to the Lamb shift [33]. The first term explains the AC-Stark shift, as it shifts $\tilde{\omega}_q$ depending on the photon number $\hat{a}^\dagger \hat{a}$ if the resonator is assumed to be at its bare frequency. On the other hand this can be viewed as qubit dependent shift of the harmonic oscillator frequency $\tilde{\omega}_r = \omega_r + \omega_q + \frac{g^2}{\Delta} \hat{\sigma}_z$ (see Fig. 10b)).

This effect is one of the big advantages of such circuit QED systems, as it allows to perform quantum non-demolition measurements on the qubit state. This means that we can determine the qubit state by a projective measurement without disturbing it. For such measurements we can use the fact that $\hat{\sigma}_z$ is correlated with the qubit state, and therefore the shift of the resonator frequency provides information about the qubit state. This shift can be seen in amplitude as well as in phase measurements, a theoretical result of such measurements is shown in Figure 11. In practice we probe the resonator at the frequency $\omega = \omega_r - \chi$ ($\chi = \frac{g^2}{\Delta}$) corresponding to the groundstate. If the qubit is then excited into the $|e\rangle$ state the amplitude and the phase of the transmitted signal changes. Such measurements are therefore often called dispersive readout.

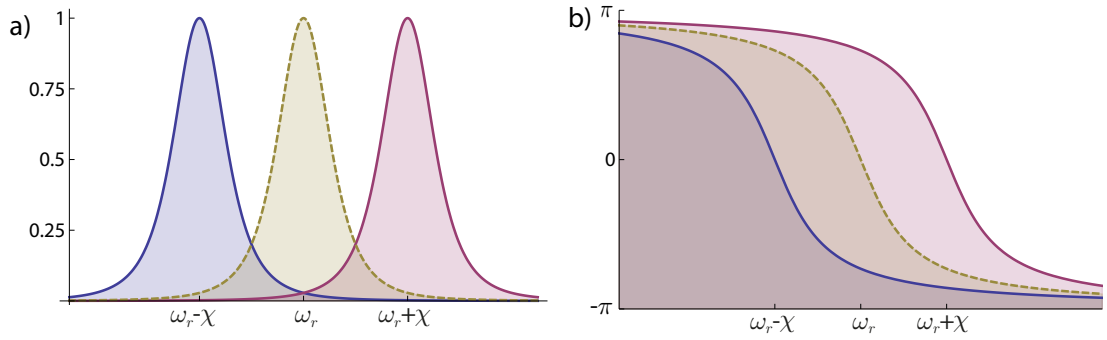

Figure 11: The dispersive shift a) of the amplitude peak of the transmission and b) of the phase shift.

3 Photon shaping

The process of photon shaping denotes the generation of single photons with given shape of its waveform. This shape is determined by the probability, that the photon emitting process takes place as a function of time. This means, if we deal with a simple spontaneously decaying two level system, the emitted photon will always have an exponentially decaying shape, as the intrinsic decay occurs randomly with a probability distribution exponential in time, with time constant T_1.

The reason for investigating ways to alter the shape of such photons lies in the possible applications for quantum communications, namely the realization of quantum networks [1]. In order to realize such networks it is crucial to achieve quantum state transfer with unit efficiency, allowing to entangle distant nodes and also teleportation of quantum states [36]. In general photons are well suited to be used as flying qubits, as they allow for fast and state preserving transfer, even over longer distances. However the spontaneous emission of a two level system is irreversible, resulting in an absorption efficiency of maximally 54% [37]. The basic idea to get to higher efficiency presented by Cirac et al. in [23] is, that the time reversed process would theoretically allow to absorb the photon with unit efficiency. This means if we could create a photon with exponentially increasing shape and apart from that equal characteristics, it would mimic the reverse of the emission and therefore be absorbed with unit probability. Thus it is necessary to alter the emission process to reach the required efficiency in coherent state transfer, as we cannot manipulate the photon and change its shape when it is already in flight. The goal is to get a photon with a symmetric time shape as this is equivalent to time reversing the process, if emitting and absorbing cavities have the same characteristics. Such a system has already been realized using atoms in optical cavities, although still limited in efficiency [38].

Photon shaping methods using circuit QED have also recently been proposed and realized, based on tunable coupling either between the resonator and the Transmission line [39, 40] or between the qubit and the resonator [41, 42]. Both use tunable SQUID loops to realize the variable coupling. In this work we choose a different method based on a tunable coupling between resonator and qubit, induced by a phase- and amplitude-modulated microwave signal [43]. In contrast to the aforementioned schemes, our method does not require tunable elements, but instead the shaping is fully controlled by the

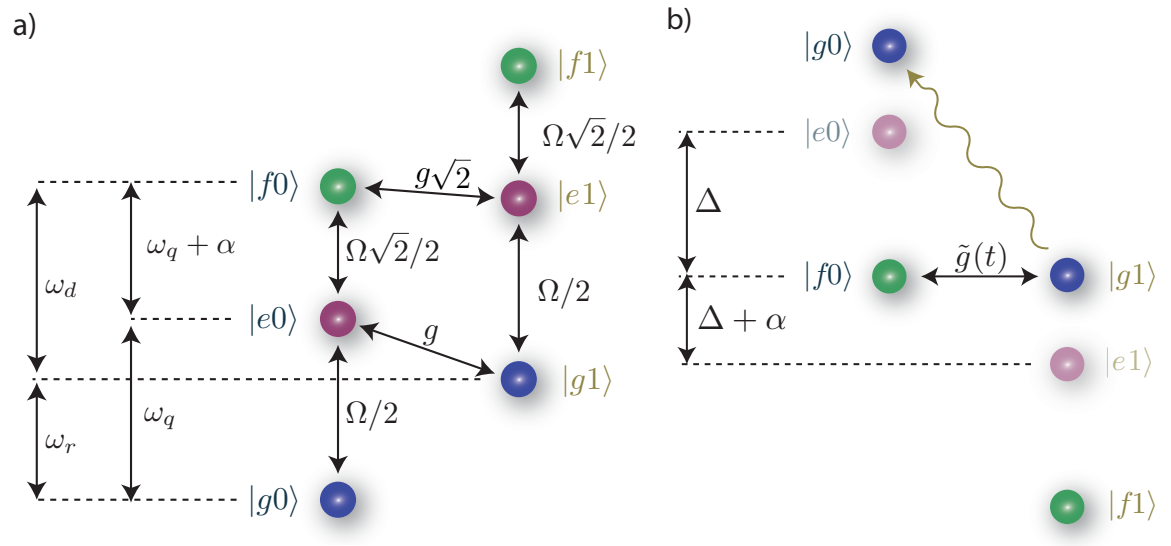

Figure 12: a) Schematic drawing of the photon shaping method, indicating Jaynes-Cummings coupling g and the applied microwave drive Ω. b) The effective coupling induced by the drive and the single photon decay shown in the rotating frame of the drive frequency.

amplitude and phase of the applied microwave drive. This has the advantage that the Josephson inductance is kept constant, which otherwise leads to frequency shifts that need to be corrected to gain full control over phase and envelope of the photon. Therefore, schemes utilizing tunable Josephson inductances require an additional tunable parameter to allow to correct for the frequency shifts.

3.1 Microwave induced second order coupling

In our scheme we make use of a second-order process, using a microwave signal to drive the transition between the $|f0\rangle$ and $|g1\rangle$ state as illustrated in Fig. 12. This introduces an effective coupling between the qubit and the resonator, allowing to control the emission of the photon. The system is operated in the dispersive regime $|\Delta| = |\omega_q - \omega_r| \gg g$, such that no energy is coherently exchanged between qubit and resonator in the absence of a drive. Driving the qubit at a frequency $\omega_d = 2\omega_q + \alpha - \omega_r$ given by the energy difference between the states $|f0\rangle$ and $|g1\rangle$, introduces an effective second order coupling between these states.

Using creation and annihilation operators for the transmon given by $\hat{b} = |g\rangle\langle e| + \sqrt{2}|e\rangle\langle f| + \sqrt{3}|f\rangle\langle h| + ...$, we can rewrite the transmon-resonator Hamiltonian (Eq. (39)) as follows

$$\frac{\hat{H}}{\hbar} = \omega_q \hat{b}^\dagger \hat{b} + \frac{1}{2}\alpha \hat{b}^\dagger \hat{b}^\dagger \hat{b}\hat{b} + \omega_r \hat{a}^\dagger \hat{a} + g\left(\hat{b}\hat{a}^\dagger + \hat{b}^\dagger \hat{a}\right) + \frac{1}{2}\Omega_0(t)\left(e^{i(\omega_d t - \phi(t))}\hat{b} + e^{-i(\omega_d t - \phi(t))}\hat{b}^\dagger\right), \tag{46}$$

now including the applied drive with phase $\phi(t)$ and amplitude $\Omega_0(t)$, slowly varying in time. Applying the unitary transformation $\hat{U} = e^{i\omega_d(\hat{b}^\dagger\hat{b} + \hat{a}^\dagger\hat{a})}$ we can look at the Hamilto-

nian in the reference frame rotating at the frequency ω_d, using Eq. (32)

$$\frac{\hat{H}_r}{\hbar} = \delta_q \hat{b}^\dagger \hat{b} + \frac{1}{2}\alpha \hat{b}^\dagger \hat{b}^\dagger \hat{b}\hat{b} + \delta_r \hat{a}^\dagger \hat{a} + g\left(\hat{b}\hat{a}^\dagger + \hat{b}^\dagger \hat{a}\right) + \frac{1}{2}\Omega_0(t)\left(e^{-i\phi(t)}\hat{b} + e^{i\phi(t)}\hat{b}^\dagger\right). \tag{47}$$

The transition frequencies of the qubit and the resonator in the rotating frame are given by $\delta_q = \omega_q - \omega_d = -\Delta - \alpha$ and $\delta_r = -2\Delta - \alpha$. In this rotating frame, $|f0\rangle$ and $|g1\rangle$ are resonant, whereas $|e0\rangle$ and $|e1\rangle$ are detuned by Δ and $-\Delta - \alpha$ and thus far off resonant. This allows to restrict the system to a two level subspace consisting of the states $|g\rangle$ and$|f\rangle$, by adiabatically eliminating the $|e\rangle$ states, as they are not populated by the off-resonant drive. The resulting system possesses an effective second-order coupling $\tilde{g}(t)$, which can be approximated using perturbation theory [44]

$$\tilde{g}(t) = \frac{1}{\sqrt{2}}\frac{g\alpha}{\Delta(\Delta+\alpha)}\Omega_0(t)e^{i\phi(t)}. \tag{48}$$

Using this effective Jaynes-Cummings type coupling we can write down the effective Hamiltonian of the system [43]

$$H_{eff} = \Delta_{f0g1}(t)\,|f\rangle\langle f| + \tilde{g}(t)\,|f0\rangle\langle g1| + h.c., \tag{49}$$

where only the difference between the AC stark shifts Δ_{f0g1} of the states $|f0\rangle$ and $|g1\rangle$ dependent on the drive is kept. This factor is to leading order quadratic in the drive strength ω_0 [43] and needs to be calibrated for the experiments.

As the effective coupling $\tilde{g}(t)$ is proportional to the amplitude and phase of the applied drive, it is fully tunable by the microwave drive signal. Therefore, it is now possible with this scheme to generate shaped photons by controlling the population of the $|g1\rangle$ state, which then decays into the $|g0\rangle$ state via emitting a photon. For a detailed discussion about the constraints on the drive see Sec. 6.2.

Besides the scheme that has been described above, we also realized photon shaping using a first order coupling by tuning qubit and resonator into resonance. The drive is then applied between the $|f0\rangle$ and one of the polariton states $|1,-\rangle$, $|1,+\rangle$.

4 Measurement setup

The final goal of this experiment is to emit a shaped photon and reabsorb it with another sample, realizing a state transfer between two distant nodes. Therefore two identical samples consisting of a resonator and a qubit are needed, connected in a way that it is possible to efficiently exchange a photon. To understand what happens if we couple two resonators directly, or using a transmission line, we consider some theoretical estimations.

4.1 Two directly coupled resonators

First we look at a system consisting out of two directly coupled resonators as shown in Fig. 13.

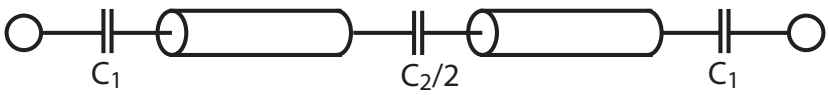

Figure 13: Two directly coupled resonators.

The resonance frequencies of a system are in general given by the divergences of the frequency dependent impedance $Z(\omega)$. To calculate the impedance of the given system we can make use of the symmetry by splitting the center capacitance into two equal capacitors, calculating the impedance by only looking at the first half of the system. In addition we consider even and odd solutions separately, leading to two distinct cases. For the odd solutions the standing waves have a voltage node at the center point between the resonators and the system can be assumed to be connected to ground, on the other hand for the even solutions the standing waves have a current node at the center point and the two halfs can be considered to be disconnected from each other, see Fig. 14.

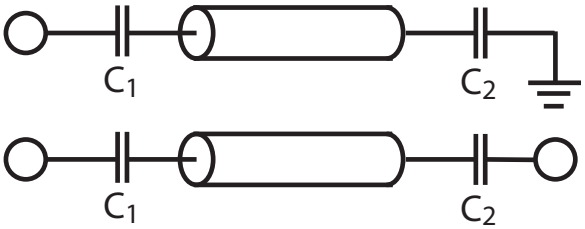

Figure 14: The two cases for two directly coupled resonators: upper one connected to ground (odd solutions), lower one to an open output (even solutions).

In general the impedance of a capacitor is given by

$$Z_C(\omega) = \frac{1}{i\omega C} \tag{50}$$

and for a lossless transmission line, which is connected to ground via an impedance Z' we get

$$Z_T(\omega) = Z' \frac{1 + i\frac{Z_0}{Z'} \tan\left(\frac{\omega}{v} l\right)}{1 + i\frac{Z'}{Z_0} \tan\left(\frac{\omega}{v} l\right)}, \tag{51}$$

where v is the propagation velocity in the transmission line, l denotes the length of the resonator and $Z_0 = 50\,\Omega$ the characteristic impedance of the line. Note that we consider the system without impedance matched $50\,\Omega$ input- and output-ports, which means that we neglect dissipation here.

4.1.1 First case: connected to ground

Looking at the impedances with respect to the point between the transmission line and C_2, denoting them Z_1 and Z_2, we get the following condition for resonances

$$\frac{1}{Z_1} + \frac{1}{Z_2} = \frac{1}{Z_{tot}} \xrightarrow{Z_{tot}\to\infty} 0 \qquad \Longrightarrow Z_1 = -Z_2. \tag{52}$$

Using Eqs. (50) & (51) leads to the following relation

$$-\frac{1}{i\omega C_2} = \frac{1}{i\omega C_1}\frac{1 - Z_0\omega C_1 \tan\left(\frac{\omega}{v}l\right)}{1 + \frac{1}{Z_0\omega C_1}\tan\left(\frac{\omega}{v}l\right)} = \frac{1 - Z_0\omega C_1 \tan\left(\frac{\omega}{v}l\right)}{i\omega C_1 + i\frac{1}{Z_0}\tan\left(\frac{\omega}{v}l\right)}. \tag{53}$$

As the left-hand side is connected to an open output we take the limit of $\omega C_1 \to 0$ and get

$$-\frac{1}{i\omega C_2} = \frac{1}{i\frac{1}{Z_0}\tan\left(\frac{\omega}{v}l\right)}. \tag{54}$$

Now we substitute ω by $\omega_r^0 + \delta\omega$ where ω_r^0 denotes the bare resonance frequency without coupling to a second resonator, leading to

$$-\frac{1}{i(\omega_r^0 + \delta\omega)C_2} = \frac{1}{i\frac{1}{Z_0}\tan\left(\frac{\omega_r^0+\delta\omega}{v}l\right)} \approx \frac{1}{i\frac{1}{Z_0}\left(\frac{\delta\omega}{v}l\right)}. \tag{55}$$

Where we used that $\omega_r^0 = v/l\,\pi$ and $\tan(x) \approx x$, for $x \ll 1$. Using some algebra we can finally find an expression for the frequency shift $\delta\omega$ due to the coupling

$$\delta\omega = -\frac{Z_0\omega_r^0 C_2}{\frac{l}{v} + Z_0 C_2}. \tag{56}$$

4.1.2 Second case: connected to an open output

In the second case the transmission line is not connected to the ground but to an open output on both sides. Thus $Z_2 \to \infty$ and we have to search for solutions where $Z_T(\omega) \to \infty$ for $Z' \to \infty$. Considering Eq. (51) this limit gives

$$Z_T(\omega) = \frac{1 + i\frac{Z_0}{Z'}\tan\left(\frac{\omega}{v}l\right)}{\frac{1}{Z'} + i\frac{1}{Z_0}\tan\left(\frac{\omega}{v}l\right)} \approx \frac{Z_0}{i\tan\left(\frac{\omega}{v}l\right)}, \tag{57}$$

from where it is obvious that $Z_T(\omega) \to \infty$ for $\frac{\omega}{v}l = n\pi$ with $n \in \mathbb{N}$.

4.1.3 Comparing with simulations

Now we can calculate the effect of the coupling on our system of two identical resonators, plugging in the values of one of our test sample for the setup, given in Table 1. The derived formulas give a resonance frequency of $\nu_r = 7$ GHz for the first even mode ($n = 1$ in Eq. (57)) and a shift of the resonance frequency of the odd mode due to the coupling of $\delta\nu_r = 229.55$ MHz (Eq. (56)).

C_1	4.84352 pF
C_2	48.4352 pF
l	0.015 m
v	2.1×10^8m/s
ω_r^0	7 GHz
Z_0	50 Ohm

Table 1: Designed values for an asymmetric resonator sample.

To check the validity of our approximations we compare the results with simulations of the system using *Microwave Office* and also using the ABCD-matrix formalism in combination with *Mathematica*.

For the simulation with *Microwave Office* the distance between the two maxima amounts to $\delta\nu_r^{sim} = 228.6$ MHz, showing that the difference between the analytical calculation and the simulation is below 0.5%. But in contrast to our approximations the resonances in the simulations are in total shifted to lower frequencies (Fig. 15), leading to a resonance frequency of $\nu_r^{sim} = 6.9861$ GHz for the bare resonance frequency. This is due to the fact that we have considered the resonator to be connected to an open output, whereas in the simulations the system is connected to ground via a 50 Ohm impedance.

For the simulation with ABCD-matrices in *Mathematica* the frequency shift is given by $\delta\nu_r^{sim} = 227.25$ MHz, which is still in good agreement with our calculations. Also here the bare resonance peak is not located at 7 GHz but at $\nu_r^{sim} = 6.976$ GHz.

In fact using the slightly shifted bare resonance frequencies as initial values in the approximation gives even better results for $\delta\nu_r$ with respect to the values of the simulations. This shows that our approximation is in good agreement with both simulations and thus the given estimate is sufficient for the regime we are interested in.

4.2 Two resonators coupled through a transmission line.

In the experiment we want to realize the transfer of a shaped photon between two separated samples, therefore we would not directly couple the two resonators, but use coaxial cable to transmit the photon. This coaxial cable acts as a transmission line between the two resonators and thus we have to consider the corresponding circuit shown in Fig. 16.

To estimate the resonances in this case, we again look for a symmetric situation which can be achieved by splitting the middle transmission line into two equally long pieces. As before we consider only one half of the symmetric circuit and distinguish the cases for odd and even solutions, which leaves us with the two circuits shown in Fig. 17.

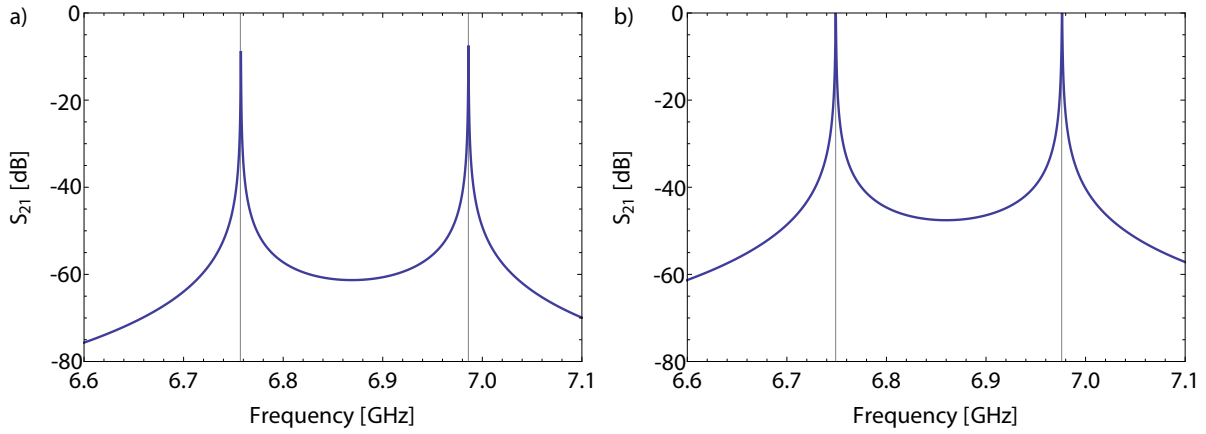

Figure 15: Simulation of two coupled capacitively resonators using: a) *Microwave Office*, b) ABCD-matrix formalism.

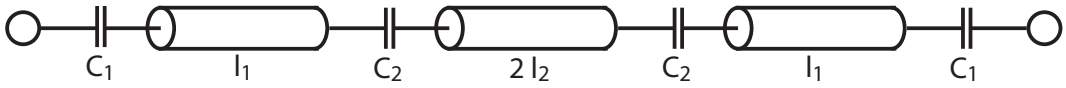

Figure 16: Two identical resonators coupled through a coaxial cable.

4.2.1 First case: connected to ground

As we have seen in the case of two directly coupled resonators the impedance of a transmission line connected to an open output is approximately given by (see Eq. (54))

$$Z(\omega) \approx -iZ_0 \cot\left(\frac{\omega}{v} l\right). \tag{58}$$

Whereas the impedance of a transmission line connected to ground can be approximated by taking the limit of $Z' \to 0$ in Eq. (51), which leads to

$$Z(\omega) \approx iZ_0 \tan\left(\frac{\omega}{v} l\right). \tag{59}$$

Therefore, calculating the impedance at the point between the first transmission line and C_2 leads to

$$-iZ_0 \cot\left(\frac{\omega}{v} l_1\right) = -\frac{1}{i\omega C_2} - iZ_0 \tan\left(\frac{\omega}{v} l_2\right). \tag{60}$$

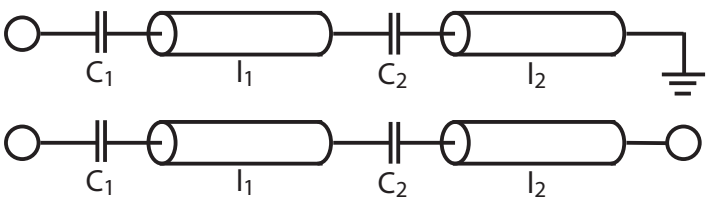

Figure 17: The two cases for two resonators coupled through a transmission line: upper one connected to ground (odd solutions), lower one to an open output (even solutions).

4.2.2 Second case: connected to an open output

In this case we calculate the impedance at the same point as for the first case, but this time the right transmission line is also connected to an open output, which gives

$$-iZ_0 \cot\left(\frac{\omega}{v} l_1\right) = -\frac{1}{i\omega C_2} + iZ_0 \cot\left(\frac{\omega}{v} l_2\right). \tag{61}$$

4.3 Comparison to measurements and simulations

This estimations show that such a system can have more resonances as the coaxial cable also acts as a resonator.

To see if we can validate the estimations we also did some measurements of such a system at 4 K in a bath of liquid Helium using a dipstick. For the measurement we used two identical, asymmetric resonators connected at the strongly coupled ports using a coaxial cable. Probing the system in transmission we found in contradiction to our expectations not only two resonance peaks around the expected position but three (Fig. 18). The first idea was that this must be due to the coaxial cable working as a third resonator with a resonance frequency right in between the other two resonances and indeed choosing a much shorter cable lead to the case of only two separated resonance peaks.

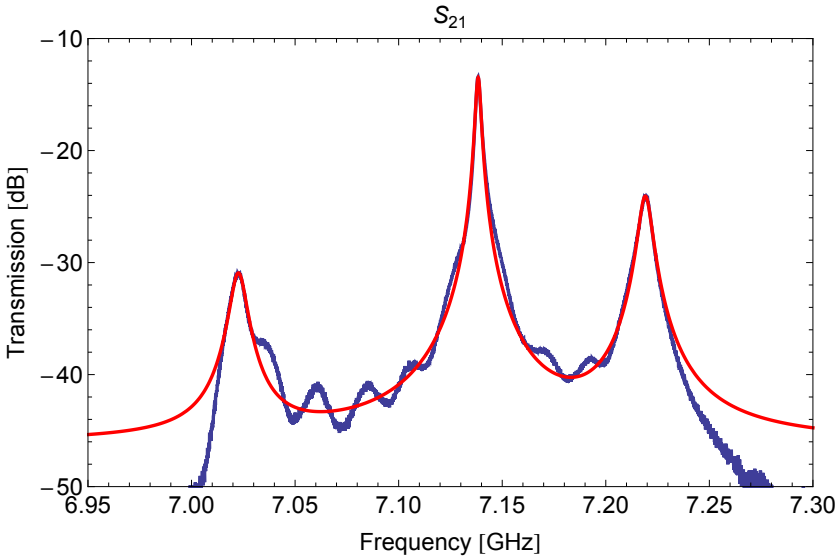

Figure 18: Measurement of two resonators connected with a coaxial cable (blue), Lorentzian fit (red).

To be able to estimate the resonance frequencies we need to know the length of the transmission lines l_1 and l_2. As we now want to be able to compare the theoretical estimation with the actual measured data, we cannot rely on the designed length and resonance frequency of the resonator, but have to find a realistic value for l_1 in terms of the measured resonance frequency.

We can estimate l_1 by comparing the measured resonance frequency of just the resonator with a simulation in *Microwave Office*, where we vary the length of the resonator such that we get the corresponding frequency. The measured resonance frequency we

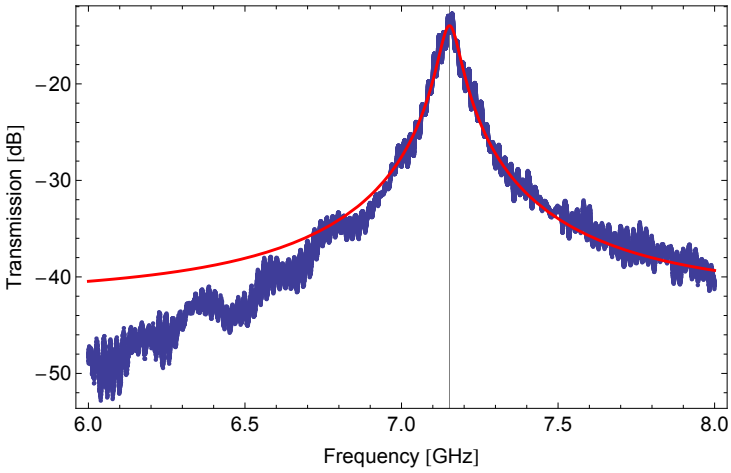

Figure 19: Lorenzian fitted to the measurement data (grey line indicates resonance frequency).

get from fitting a Lorentzian to our data and determining the maximum position is $\nu_{meas} = 7.15323$ GHz (Fig. 19).

If we now simulate the resonator connected to ground via matched 50 Ohm impedances in *Microwave Office* we can approximate the physical length by comparing the resulting resonance frequency to ν_{meas}, which gives $l_1 = 0.0141$ m.

To determine the length of the cable we measured the group delay of the cable and used this to calculate the physical length, resulting in $l_2 = 0.0749$ m.

First simulations using l_2 show that the resonances we get are lower than expected from the measurement (Fig. 18), but as l_2 is determined at room temperature and without the dipstick we have some uncertainty in the actual length of the cable. Therefore we simulate the transmission for varying l_2 using ABCD matrices in *Mathematica*. From the plot in Fig. 20 we can see that $2 \times l_2 \in [0.146\text{ m}, 0.147\text{ m}]$ would give some results comparable to the actually measured data, meaning that the resonance of the cable is around $\nu_r \approx 1.43$ GHz.

Simulations with *Microwave Office* also show that $\nu_r \approx 1.431$ GHz is a reasonable choice in comparison to the measurement data, which corresponds to $l_2 \approx 0.0734$ m. The approximated length is 1.5 mm shorter than the actual measured one, corresponding to a difference of 2%, which seems realistic as the measurements of the resonators were taken at 4 K instead of room temperature.

	$\nu_r^{(1)}$[GHz]	$\nu_r^{(2)}$[GHz]	$\nu_r^{(3)}$[GHz]	$\delta\omega_{12}$[MHz]	$\delta\omega_{23}$[MHz]
measurement	7.023	7.138	7.219	115	81
Microwave Office	7.021	7.151	7.241	130	90
Mathematica	7.021	7.151	7.242	130	89
theo. approx.	7.030	7.175	7.257	145	82

Table 2: Resulting resonance frequencies and spacing between them.

Having determined the length of the transmission line, we are now able to compare our measurements with simulations and the theoretical approximations derived earlier. The results of the simulation in comparison to theoretical approximation and measurement

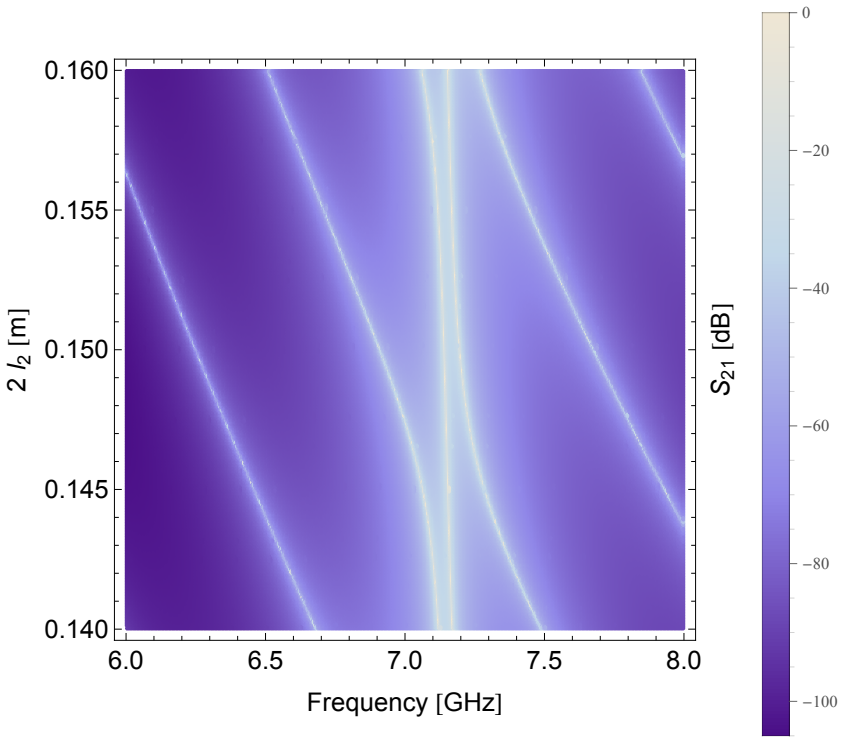

Figure 20: Transmission with as a function of frequency and l_2.

results are shown in Tab. 2. For the values of the theoretical approximation we used *Mathematica* to find the corresponding roots of the derived impedance.

Again we can see that the theoretical estimation gives in general higher frequencies. This is, as mentioned earlier, due to the fact that for our calculations we assume the circuit to be connected to an open output, whereas in the simulations it is connected to impedance matched ports.

Keeping in mind that we know the actual parameters of the measured circuit only approximately, the results show that the theoretical approximation as well as the simulations are able to describe the general behavior of the frequency spectrum and that both types of simulations give comparable results.

4.4 Circulator setup

For the planned experiment we actually want to avoid a direct coupling of the two resonators and thus a hybridization of the two systems, as we want to transmit a photon between two independent but identical subsystems. Therefore a circulator is introduced in the middle of the connecting transmission line, allowing only transfer of photons in a certain direction. This setup is chosen as it also allows to probe the whole system in reflection using only one measurement channel. A schematic drawing of the setup can be seen in Fig. 21.

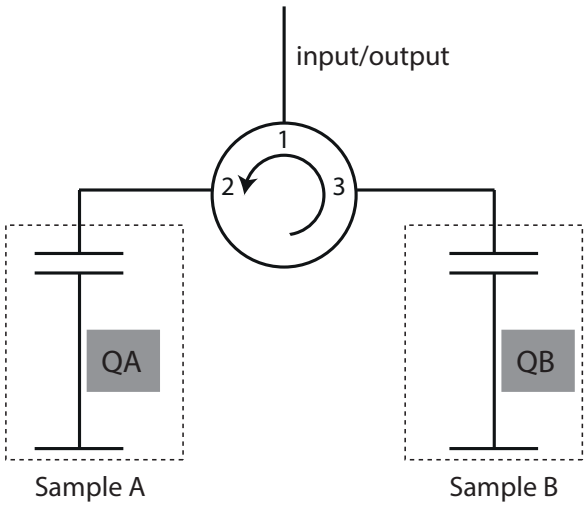

Figure 21: Circulator setup for measuring both resonators through one port.

4.4.1 Reflection measurement

Due to the chosen setup it will only be possible to measure in reflection. As this types of measurement are not very common in our laboratory we present some theoretical estimations using the input-output formalism to get an idea of what to expect.

First we look at a system as shown in Fig. 22, where a resonator coupled to a qubit is measured in reflection.

Within the input-output formalism [45], the time dependent field in the cavity is given by

$$\dot{a} = -i\omega_r a - \sqrt{\kappa} a_{in} - \frac{\kappa}{2} a - igb, \tag{62}$$

where g is the coupling constant between resonator and qubit and b describes the filed due to the qubit, given by

$$\dot{b} = -i\omega_q b - iga. \tag{63}$$

By Fourier transforming these equations we get the following matrix equation

$$\begin{pmatrix} i(\omega_r - \omega) + \frac{\kappa}{2} & ig \\ ig & i(\omega_q - \omega) \end{pmatrix} \begin{pmatrix} a \\ b \end{pmatrix} = \begin{pmatrix} -\sqrt{\kappa} a_{in} \\ 0 \end{pmatrix}. \tag{64}$$

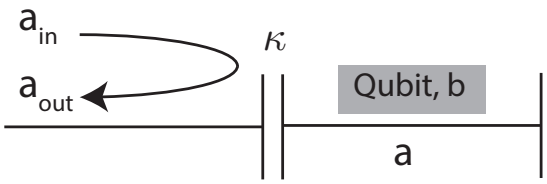

Figure 22: Reflection measurement of a resonator including one qubit.

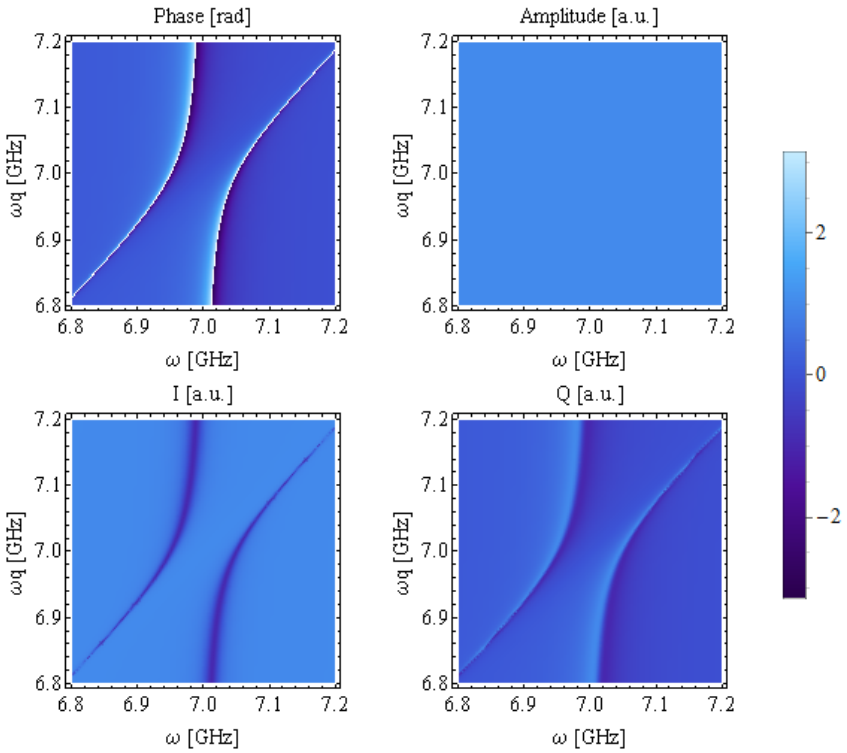

Figure 23: Simulation of reflection measurement in phase of a resonator coupled to a qubit as a function of probe signal and qubit frequency.

Using the relation between internal and external fields

$$a_{out} = \sqrt{\kappa} a + a_{in} \tag{65}$$

we can calculate the reflection coefficient

$$r = \frac{a_{out}}{a_{in}} = \frac{\sqrt{\kappa} a + a_{in}}{a_{in}} = \frac{\omega_r - \omega + \frac{g^2}{\omega - \omega_q} + i\frac{\kappa}{2}}{\omega_r - \omega + \frac{g^2}{\omega - \omega_q} - i\frac{\kappa}{2}}. \tag{66}$$

For the simulations we choose $g/2\pi = 50\,\mathrm{MHz}$, $\kappa/2\pi = 20\,\mathrm{MHz}$ and $\omega_r/2\pi = 7\,\mathrm{GHz}$, which is in the order of our sample's parameters. In order to see what to expect from a measurement we can sweep the probe frequency ω and the qubit frequency ω_q and look at the density plots of the reflected signal in phase, amplitude, I and Q. The result in Fig. 23 shows that we can clearly see an anti-crossing in phase and both quadratures but not in amplitude, which is due to the fact, that everything gets reflected. Also we can see that when crossing the resonance the phase wraps around by 2π.

Now we can look at the simulation of the actual planned measurements with the setup shown in Fig. 21. For this, we fix the frequency of the first qubit to $\omega/2\pi = 8\,\mathrm{GHz}$ and sweep the frequencies of the probe signal and the second qubit. Since the resonators in our setup will not be coupled, the phase of the measurement signal is given by the sum of the phases acquired by the signal upon reflection at both resonators individually. As presented in Fig. 24 the simulations show that it is possible to measure both resonators in reflection and that one expects a phase jump $2 \times 2\pi$ if both resonators are on resonance. Another important aspect is, that it is clearly possible to observe the crossing of only one of the qubits if the frequency of the other qubit is far detuned.

Thus we can conclude that it is possible to carry out all measurements in reflection that are required for characterization of the individual samples as well as for the actual experiments with both samples.

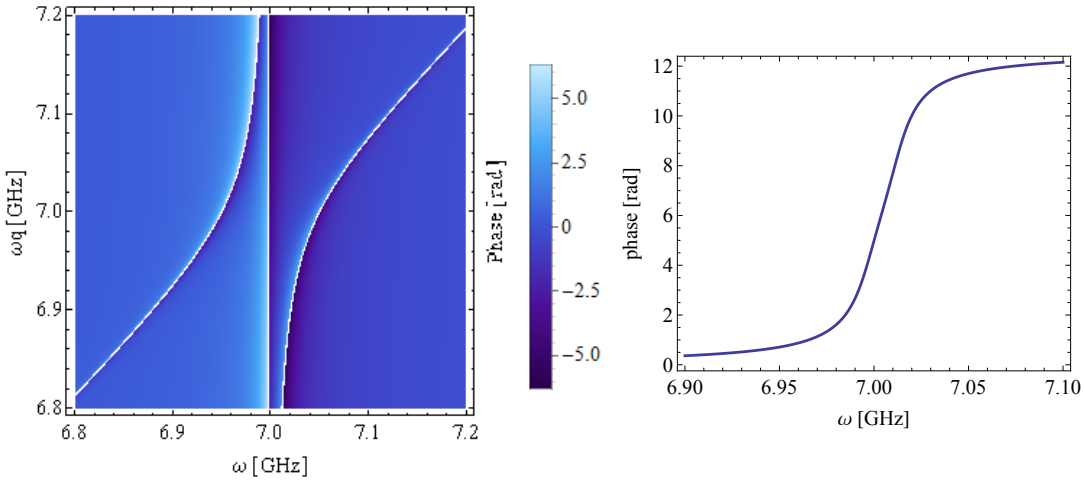

Figure 24: Simulations of reflection measurements of the actual planned setup, a) density plot of the phase of the reflected signal as a function of probe signal and qubit frequency and b) first slice of the density plot, clearly showing the phase jump of 4π.

4.4.2 Dipstick measurements

In order to check that if the circulator setup would work in principle, we first tested it in a dipstick measurement at 4 K with the two identical resonators already used for testing the coupling (see Sec. 4.3). The results show that we can see both resonators in reflection measurements if we look at the phase of the signal. For each resonator we expect a phase jump of 2π on resonance and indeed we can see a 4π phase jump if we measure in reflection as shown in Fig. 25.

4.5 Setup inside the dilution refrigerator

In order to operate systems such as those used in this experiment quantum mechanically we need to avoid dissipation, which is one reason for using superconducting materials. Another important point is, that we need to isolate our system from the environment, meaning we need to decouple the qubit from all classical elements, e.g. current sources,

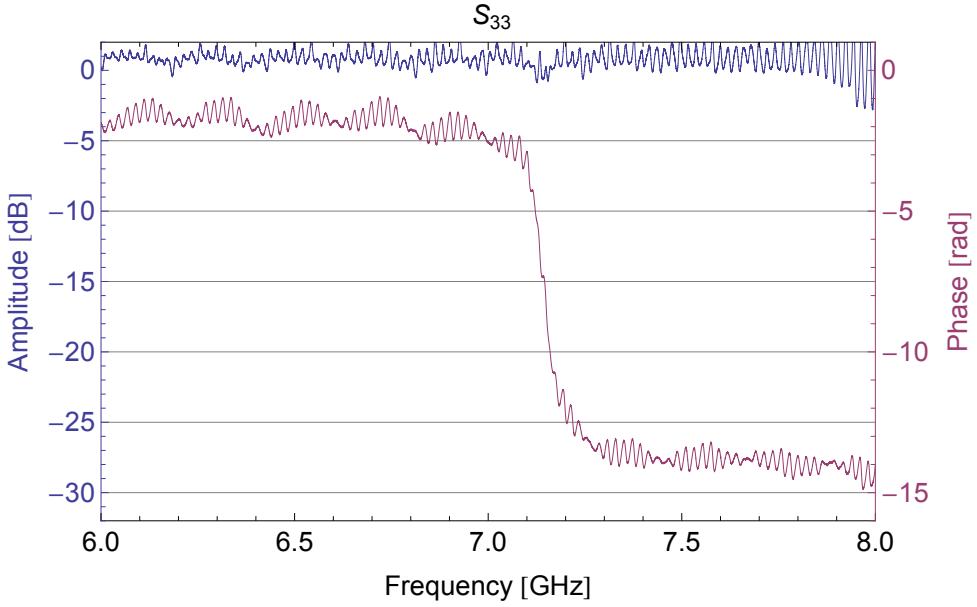

Figure 25: Phase and amplitude of the reflection measurement of the circulator setup. Clearly visible the expected phase jump of 4 π.

cables, etc. In our circuit QED design this decoupling is taken care of by the capacitative coupling of the qubit to the resonator, which acts as a resonant impedance transformer and allows to control the spontaneous emission due to vacuum fluctuations, as discussed above.

Finally we need to operate the system at low temperatures to avoid thermal excitations of the energy levels. We can estimate the characteristic temperature corresponding to $\nu_q = 8$ GHz to be $T \approx 380$ mK. To avoid thermal population of the higher energy level in the qubit we therefore need to stay well below this temperature. The thermal population can be approximated by the Bose-Einstein distribution

$$< n_{th} >= \frac{1}{e^{\frac{h\nu}{k_B T}} - 1}. \tag{67}$$

For $T = 40$ mK and $\nu_q = 8$ GHz this gives a thermal population of the $|e\rangle$ state of around $6.8 \cdot 10^{-5}$. To achieve the required temperature the whole setup needs to be placed inside a cryogen-free dilution refrigerator, which uses a pulse tube refrigerator to precool the Helium mixture. With our system we can cool the setup down to base temperatures below 40 mK.

To achieve such temperatures the wiring inside the refrigerator needs to be well thermalized at each temperature stage and the material has to be chosen such that the heat load on the lower plates is sufficiently low. Besides the thermal heat transfer of the cables we also want to reduce the Johnson-Nyquist noise due to thermal excitation of electrons inside the cables. Therefore one applies the signals at room temperature with much higher power than actually needed, such that the signal is well above the noise level. Inside the refrigerator the lines are then attenuated at different temperature stages in order to get the required low power signal at the sample. This allows to reduce the Johnson-Nyquist

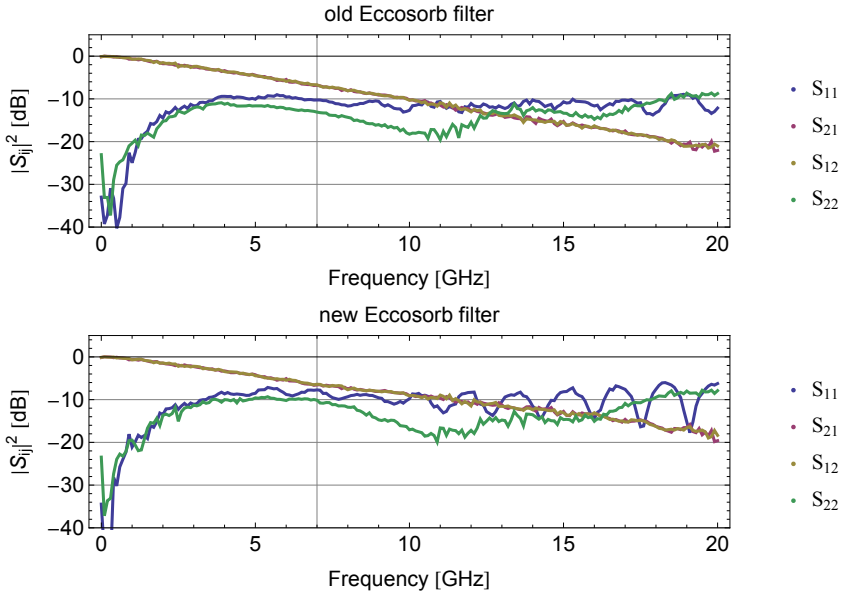

Figure 26: Comparison of the new built ECCOSORB filter and the already installed (old) one.

noise by thermalizing the center conductor and the field propagating in the coaxial cables to a low temperature. Thermally connecting the cable alone to the low temperature stages is not sufficient since it only allows us to thermalize the outer conductor due to the thermal conductance of the dielectric being very low.

In addition to the attenuators the input lines going to the sample are further attenuated by low-pass filters made out of ECCOSORB CR-124 [34], an absorptive epoxy material. In order to built these filters a piece of the dielectric in an SMA connector is replaced with ECCOSORB which has a frequency dependent attenuation, starting at 10 MHz and increasing with frequency. Thus it acts as a low pass filter serving to attenuate infrared radiation from the room temperature environment at higher frequencies, which lie outside of the working band of the standard attenuators.

To get two identical gate lines, we had to modify a former fluxline by changing some attenuators and adding an ECCOSORB filter. Several ECCOSORB filters were built to finally choose one that is closest to the filter already installed in the other gate line. In Fig. 26 VNA measurements of the new and the already installed filter are shown and it can be seen that they are in good agreement regarding their characteristics.

As the samples are very sensitive to magnetic fluxes one important part is the shielding of the samples with respect to static and slowly varying magnetic fields. Therefore the sample is surrounded by two layers of magnetic shielding made out of mu-metal with a high permeability, which effectively provides a path for the magnetic field lines leading around the surrounded area. This reduces the magnetic field by about a factor of10^4.

For the installation of the new parts for our two sample setup it is important that the circulator is placed outside of the magnetic shielding of the sample, as it contains ferrite material. This sets a lower limit for the cable length between sample and circulator, which is about 25 cm, leading to a distance of ≈ 0.5 m between the two samples. In order to ensure the thermal anchoring the circulator is mounted to the base plate using a copper plate. The mounting of the circulator can be seen in Fig. 27

The two samples are mounted on half PCBs to allow for flexibility of only changing

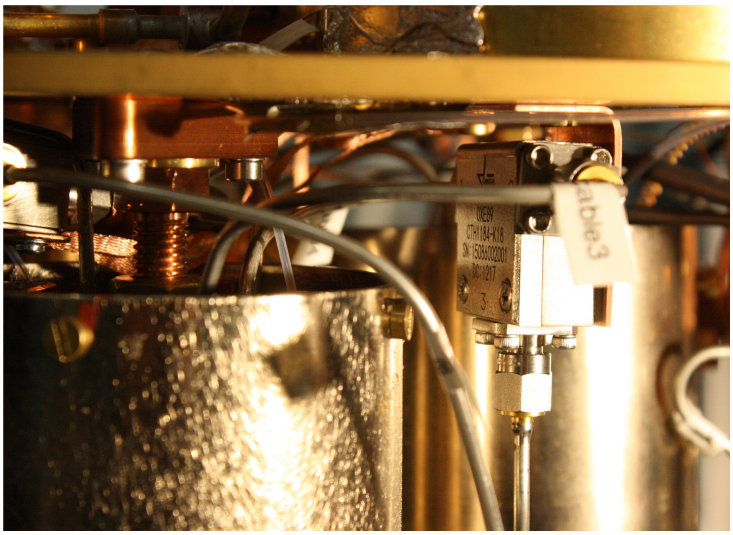

Figure 27: The circulator mounted to the base plate with the input/output line connected to port 3 and the cables connecting the samples entering the magnetic shieldings.

one of the installed samples. Below the sample holder a small and a big coil are mounted to allow control of the fluxes through each of the qubits' SQUID loops. A picture with the components of the sample holder is shown in Fig. 28.

To get a signal with a good signal to noise ratio we need to amplify the output of the resonator. This is achieved using a quantum limited Josephson Parametric Dimer amplifier (JPD) [35] that is operated at base temperature. It is mounted in its own sample holder together with a coil to realize tunability and surrounded by a single magnetic shield. Due to the narrow bandwidth it is important to accurately calibrate the amplifier such that it operates at the frequency of the output signal, at which a gain of 20 dB can be reached. Although the JPD is operated in reflection, the measurements are phase preserving.

After amplification in the JPD the signal passes through an isolator, a component consisting of a circulator with one port terminated at 50 Ω such that it transmits the signal only in one direction and thus prevents the coupling of high temperature modes to the sample and the JDP. In addition to this the isolator is followed by a bandpass filter with a bandwidth of 4-8 GHz, which also strongly attenuates signals that are outside the frequency range of our devices. After passing these two filters the signal is further amplified by a low noise high electron mobility transistor (HEMT) amplifier at the 4K plate, which provides an additional gain of 40 dB.

Besides the RF cabling also some DC lines are needed for the coils that are used to apply B-fields to the samples and the JPD as well as for the HEMT amplifier.

The complete configuration of the wiring inside the refrigerator is shown in Fig. 29.

4.6 Room temperature electronics

To be able to apply and measure microwave signals on the various in- and output-ports one also needs various components outside of the fridge. The signals are generated with Microwave Generators (MG) and then modified (attenuated, amplified, frequency-mixed) according to the port they are connected to and the planned measurements. In general attenuators are also used outside the fridge as they help to reduce standing waves due to

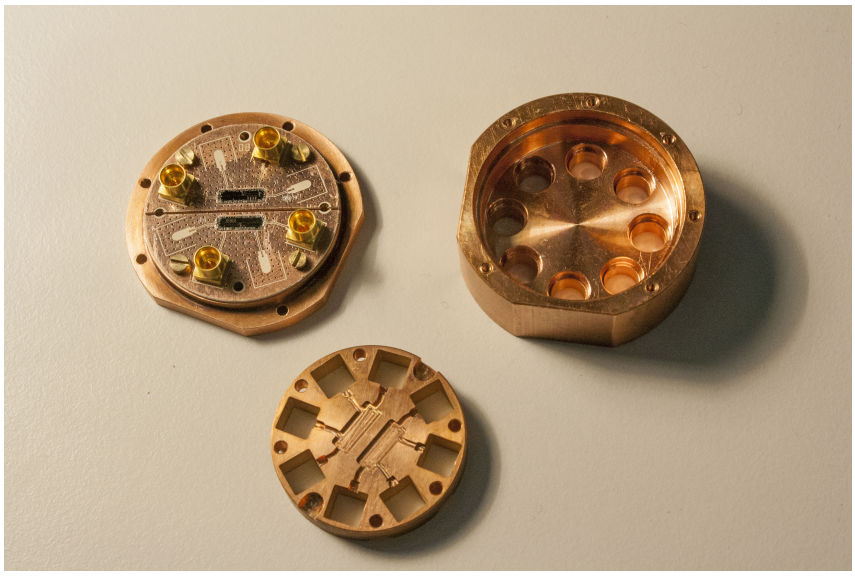

Figure 28: PCBs mounted to the bottom of the sample holder (left), upper part of the sample holder (right) and the cover for the PCBs (middle)

impedance mismatches of the various components.

As we want to measure in reflection we need to split the signal of the MG connected to the resonator input to get a phase reference signal. This is necessary because the phase of the MG is randomized as soon as we change the frequency of the applied tone.

To be able to apply arbitrary pulses to the qubit gate lines we need IQ-mixers, which modulate the signal of the local oscillator (LO) by the applied I and Q quadratures. The output of such a mixer is given by

$$\Re\left[(I(t)+iQ(t))e^{i\omega_{LO}t}\right] = I(t)\cos(\omega_{LO}t) - Q(t)\sin(\omega_{LO}t) \tag{68}$$

Choosing $I(t) = A_I\cos(\omega_{IF}t+\varphi_I)$ and $Q(t) = A_Q\cos(\omega_{IF}t+\varphi_Q)$ we get for the output signal

$$\begin{aligned} S_{RF} =& A_I\cos(\omega_{IF}t+\varphi_I)\cos(\omega_{LO}t) - A_Q\cos(\omega_{IF}t+\varphi_Q)\sin(\omega_{LO}t) \\ =& \frac{1}{2}\left[A_I\cos(\omega^+t+\varphi_I) - A_Q\sin(\omega^+t+\varphi_Q) + A_I\cos(\omega^-t-\varphi_I) - A_Q\sin(\omega^-t-\varphi_Q)\right], \end{aligned} \tag{69}$$

showing that we get two sidebands at $\omega^\pm = \omega_{LO} \pm \omega_{IF}$. It also shows that either one of the sidebands can be canceled out by choosing the phases to be $\varphi_I = 0$, $\varphi_Q = \frac{\pi}{2}$ for cancellation of the right and $\varphi_I = \frac{\pi}{2}$, $\varphi_Q = 0$ for cancellation of the left sideband.

This procedure is often referred to as upconversion, as the low frequency modulations of I and Q are mapped to the high frequency LO signal. In reality the sideband cancellation is often not perfect for the discussed phase values, therefore the signal is split after the mixer to get a signal for calibrating phase and amplitude of I and Q for each sideband. In addition also the LO leakage can be calibrated by adding a constant offset to the I and Q signals, which are generated by an Arbitrary Waveform Generator (AWG). By loading the corresponding waveform patterns into the AWG the mixer allows us to apply arbitrary shaped pulses to the gate lines. In particular we are interested in applying gaussian pulses to drive qubit transitions. Depending on the actual configuration of the gate lines and

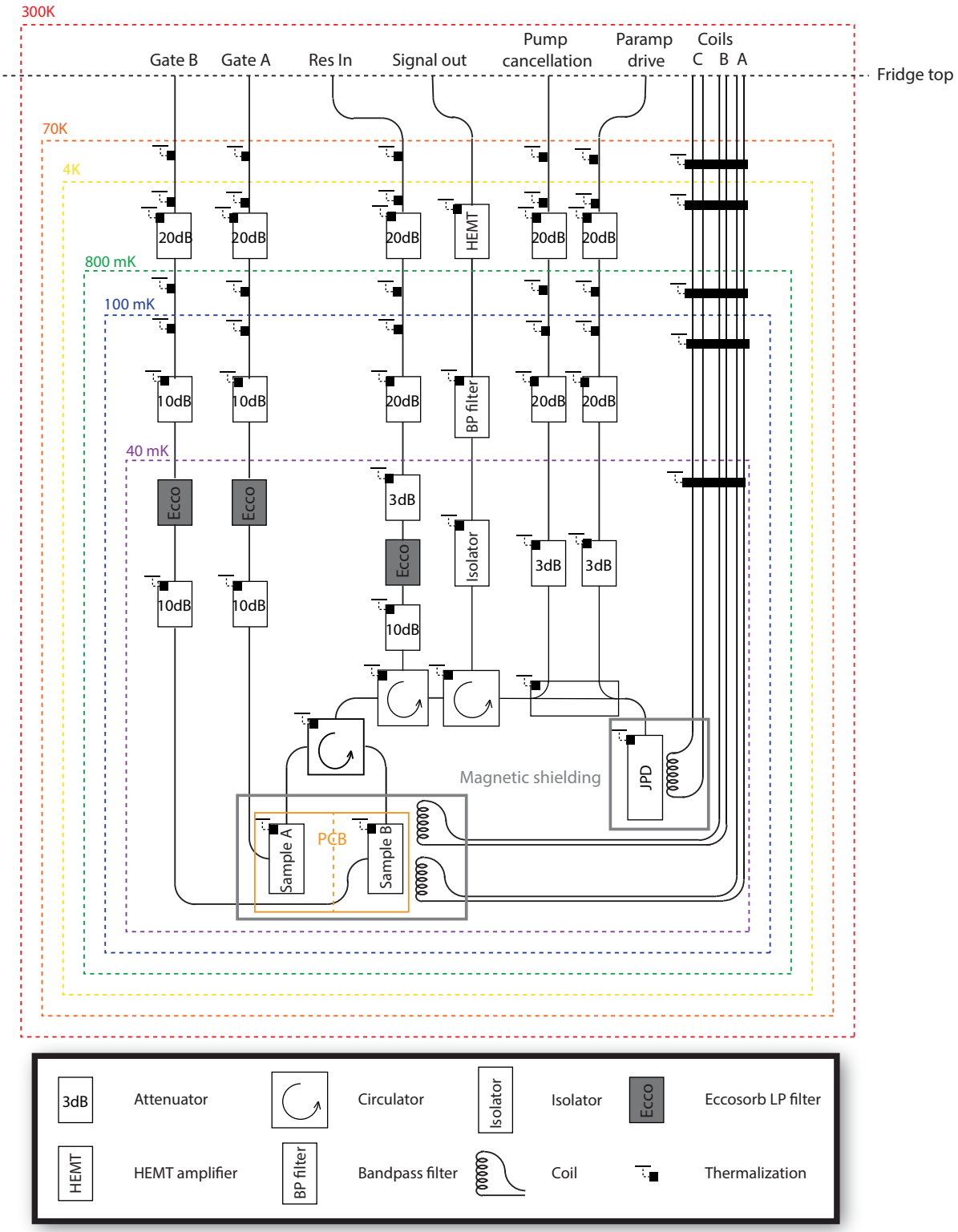

Figure 29: Wiring of all components inside the dilution refrigerator.

the sample parameters it can be necessary to amplify the signal after the mixer to get enough power to drive e.g. second order transitions in the qubit.

Besides the shaped pulses it is also possible to use markers of the AWG to gate a MG to obtain a square pulse witha few ns rise time.

In order to measure the signal coming from the fridge we need to use again an IQ-mixer to perform a downconversion of the signal to a lower intermediate frequency (IF) of 25 MHz such that the analog to digital converter (ADC) can digitize the signal at a rate of 100 MS/s. The signal is then processed by a field-programmable gate array (FPGA) programmed to average, filter and process the data according to the measurement settings chosen on the measurement computer. The whole experiment is controlled using a Labview-based program called "CleanSweep", continuously improved and extended in the laboratory. It allows to modify all the settings of the MG's and to load patterns into the AWG, as well as to choose different measurement modes, number of averages and coil voltages. To control the timing of the various components all measurements are triggered by the AWG.

As the number of MG's and measurement channels is limited we also use switches in the setup that can be set using the measurement computer. The setup that was used for the second order process with the latest samples can be seen in Fig. 30.

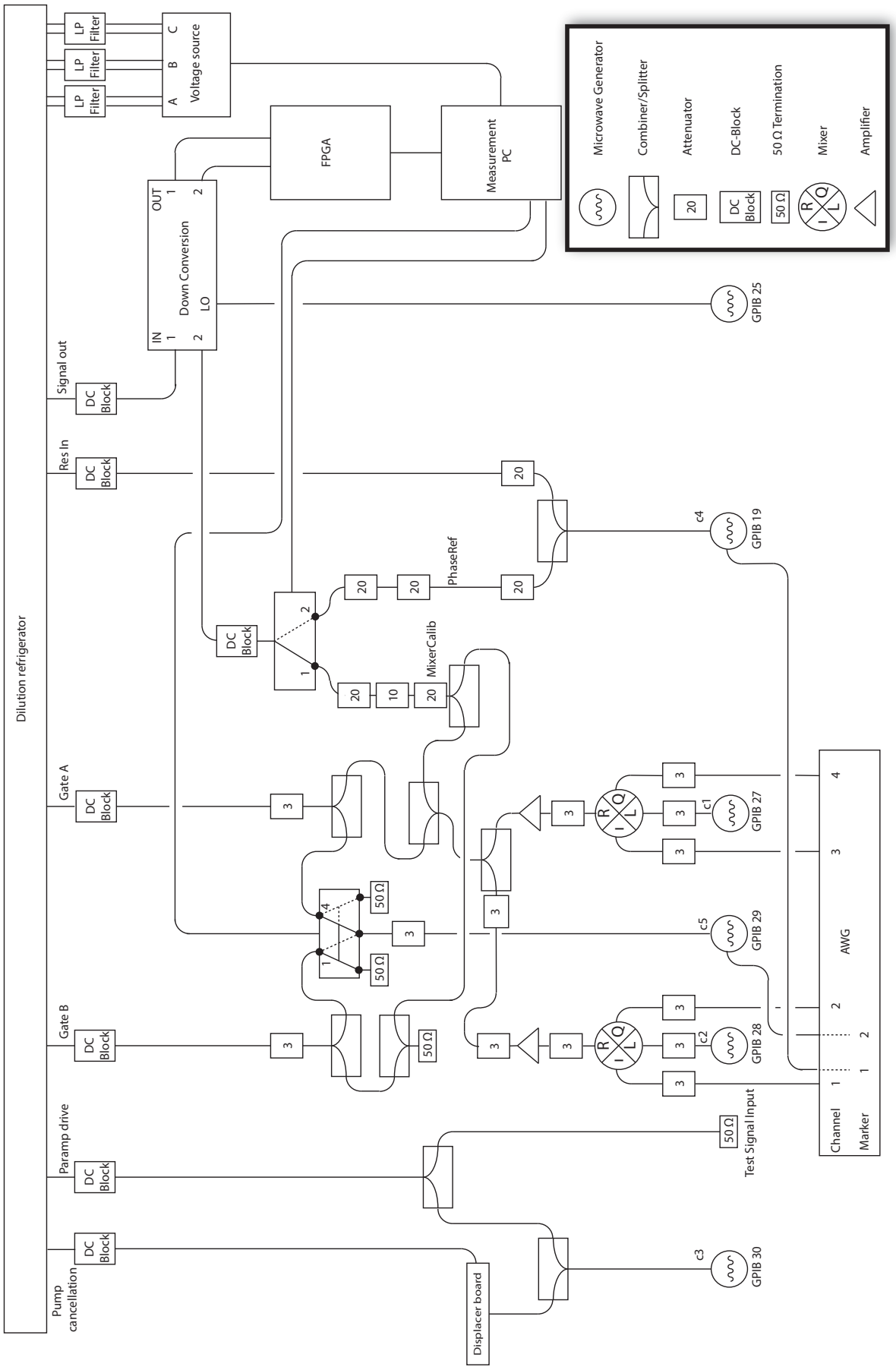

Figure 30: Wiring of all components outside the dilution refrigerator.

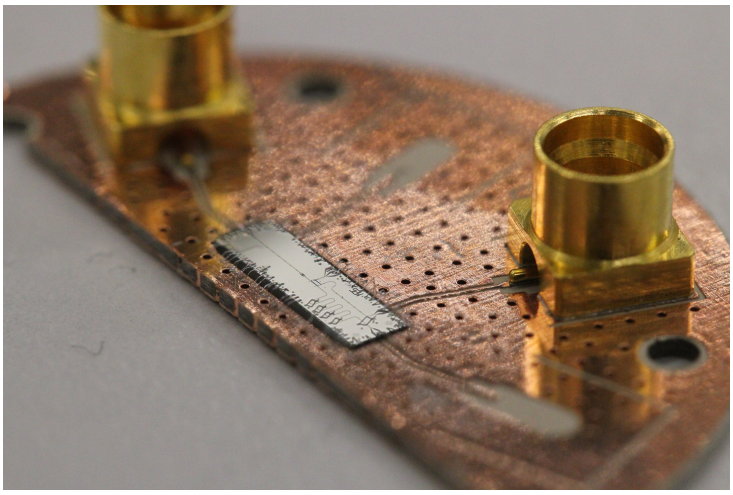

Figure 31: A sample glued and wire bonded to one half of a PCB with SMP connectors for the coaxial lines.

5 Qubit design and life time estimations

One important aspect of the experiment is the design of the samples. On one hand we need to find a design which provides the right parameters for our experiments and on the other hand the overall lifetime of the qubit states is affected by the chosen design and needs to be reasonably high. The important parameters of qubit and resonator determined by the design and fabrication are the characteristic energies E_j and E_c as well as the couplings between resonator, qubit and the control lines. Therefore, α, ω_q^{max}, κ and g are determined for each sample and cannot be altered during the experiments, at least not in the designs used here.

In general the samples in our laboratory are all fabricated by members of the group in the cleanroom facility of the ETH (Swiss federal institute of technology). Our samples are based on sapphire wafers with a niobium layer on top of it. All structures on the chip are written in optical lithography, except for the qubits, which are written in the last step using electron beam lithography and shadow evaporation of aluminum. Finally the samples are glued and wire bonded to a PCB, which provides the connections to the coaxial lines. A sample ready to be put in the setup can be seen in Fig. 31.

5.1 Resonator parameters

The chips used for the experiments presented in this thesis were all produced using the same mask for the optical lithography. Therefore, the parameters and design of the chips are the same throughout all experiments, whereas the design of the qubit was adjusted after the first run of experiments.

The design of the resonator was chosen to have a high asymmetry given by an order of magnitude difference between the two coupling capacitors. The reason for choosing this asymmetric design is that it ensures that the photon decays mostly into the readout line of our system. In addition the values of the capacitances are chosen such that the decay rate κ is high, enabling a fast photon decay. The mask design includes ports on both sides of the resonator, but since for the experiment only the strongly coupled port is required, the second port is connected to ground on the PCB using wire bonds. Besides

C_1	3.04 fF
C_2	30.44 fF
$\kappa/2\pi$	20 MHz
$\omega_r/2\pi$	7.0 GHz

Table 3: Designed parameters for the resonator.

the resonator the mask design also includes a gate line which is needed to drive the qubit and a fluxline. The latter can be used to apply flux pulses to the SQUID, allowing for fast control of the qubit frequency. As our experiments do not require such fast control, the two coils below the sample holder suffice to control the qubit frequencies. Therefore, the fluxline is also connected to ground on the PCB using wire bonds in order to minimize the fluctuations that can be induced by such control lines. The ground planes are connected using aluminum airbridges and wire bonds in such a way, that no current loop enclosing the qubit is created on the superconducting chip. A false colored picture of the chip without the qubit is given in Fig. 32a) and the designed parameters are summarized in Tab. 3.

5.2 Qubit design

The qubit design for our samples was done using the program *Maxwell 3D*, which uses finite elements for numerically solving the Maxwell equations for three-dimensional structures. The structure can be drawn directly within the program and after specifying the materials of the different layers one can set up a mesh of electric fields, which is then used for the simulations. To reliably simulate the system including the different couplings, we not only take the qubit into account, but also the surrounding area including parts of the resonator and the control lines. The parameters of the qubit are determined by the different capacitances, which can be adjusted by varying the size and shape of the different components as well as the positions and distances with respect to each other. The program returns a matrix containing the capacitances between the various parts, which allows to give an estimate for E_c and g.

5.2.1 Qubit lifetimes

As pointed out, it is important to get an estimate for the qubit lifetimes as these can be a limiting factor in the experiments. The qubit relaxation time T_1 denotes the lifetime of the $|e\rangle$ state due to decay into the ground state. There are several decay channels that contribute to this decay and it is still not fully understood how large the contributions of the various channels are. As the sample is placed inside a resonator the spontaneous emission is altered due to the Purcell effect, which leads to an additional decay rate given by [28]

$$\gamma = \kappa \frac{g^2}{\Delta^2}. \tag{70}$$

Other mechanisms that might contribute to an increasing decay rate are dielectric losses due to surface interfaces [47] as well as the tunneling of nonequilibrium quasiparticles [48], which can occur due to an uneven number of electrons or breaking of Cooper pairs due to non zero temperature.

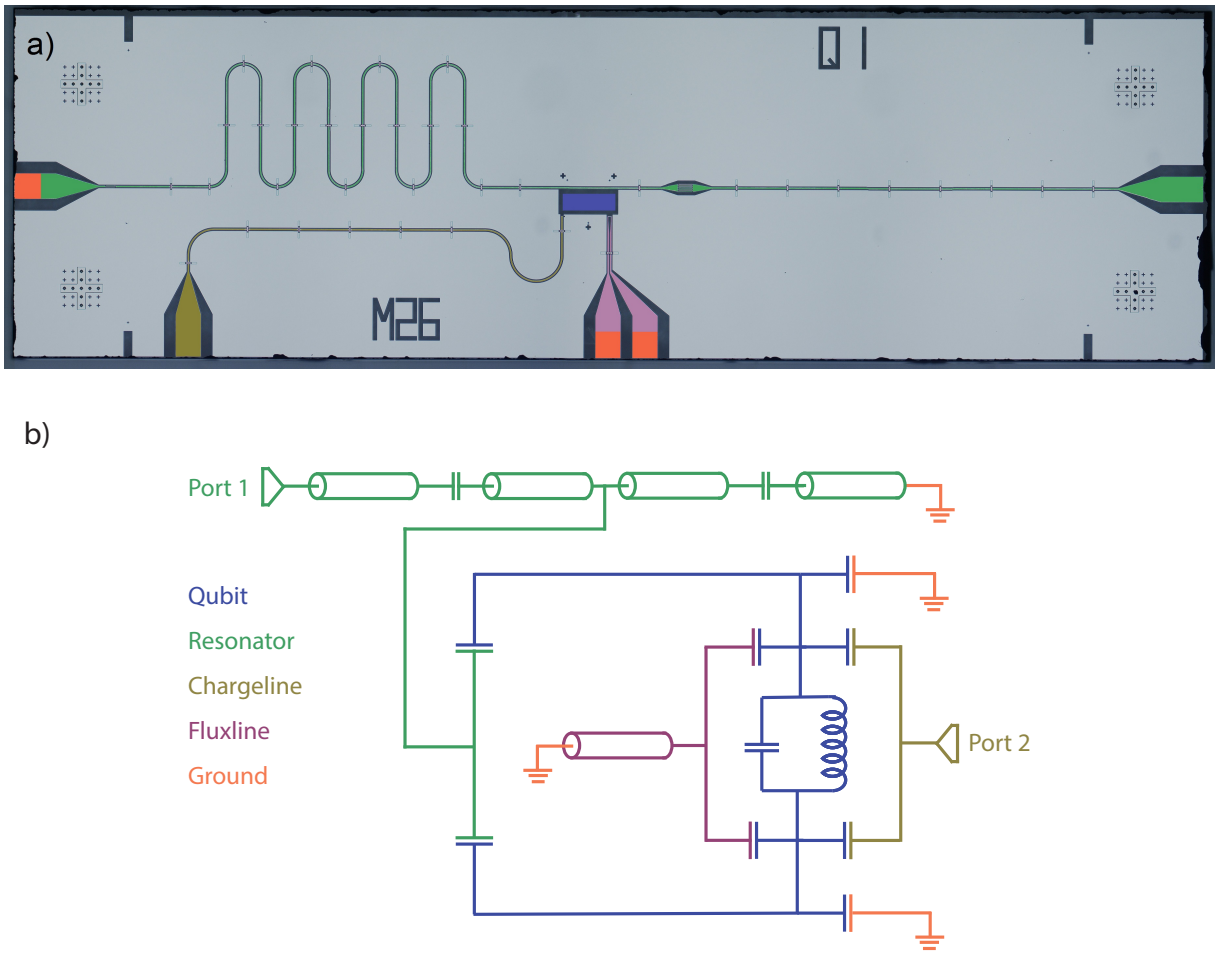

Figure 32: a) A false colored picture of the chip, where the position of the qubit is given by the blue box in the center and the orange boxes indicate which ports are connected to ground. b) The corresponding labeling of the components in combination with an equivalent circuit for the qubit resonator system used in this thesis.

Due to fluctuations of the qubit transition frequency the qubit dephases which leads to decoherence in the system. The coherence time T_2 experiences an upper bound due to the energy losses originating from the qubit relaxation, given by $T_2 \leq 2T_1$. In addition to this, several sources can induce so-called pure dephasing, for example charge and flux noises can induce variations of the qubit frequency as well as noise in the critical current [28]. Furthermore, in addition to the qubit relaxation time the quasiparticle tunneling contributes also to the dephasing time [49].

To get an upper bound for the T_1 time we started by analysing the admittance of a simplified equivalent circuit of the system to get an idea of the order of κ. We approximated the qubit as a LC harmonic oscillator and assumed the control lines to be connected to ground via a matched 50Ω impedance. Finally for the resonator we only considered the capacitative coupling. A schematic of the simplified equivalent circuit is shown in Fig. 33.

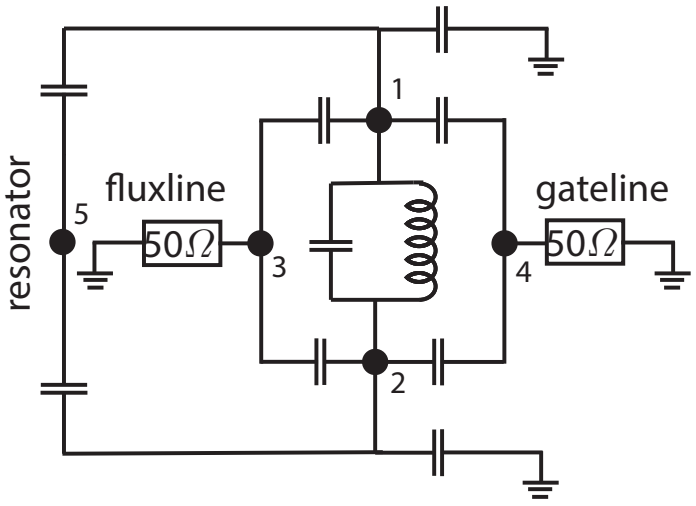

Figure 33: Simplified equivalent circuit of the qubit for estimating an upper bound on the qubit lifetime by analyzing the admittance of the circuit, taking into account the 5 marked nodes.

In order to get the admittance of the circuit we use

$$I_i = \frac{V_i}{Z_i} + \sum_{i \neq j} \frac{V_i - V_j}{Z_{ij}} = M\vec{V}, \tag{71}$$

where Z_i denotes the impedance from node i to ground and Z_{ij} the impedance between the nodes i and j. Therefore, the admittance matrix of our system is given by

$$Y(\omega_q + i\frac{\kappa}{2}) = \frac{1}{M^{-1}}. \tag{72}$$

To approximate κ we search for poles of the impedance, i.e. zeros of Y. We do this by minimizing the absolute square of the admittance at one node of the network

$$|Y_{ii}(\omega_q - i\frac{\kappa}{2})|^2, \tag{73}$$

at a given ω_q. The inductance L can be approximated by using $\omega_q = 1/\sqrt{LC}$, giving a value on the order of several nH. Therefore, we can get an estimate of the life time given by $T_1 = \frac{1}{2\pi\kappa}$. However, as we do not take the resonator into account, as well as we assume that the gate line is not connected, we exclude some prominent decay channels and thus only get a rough upper bound.

A more appropriate approximation was done using *Microwave Office* in order to simulate the equivalent circuit of the qubit including resonator and control lines, shown in Fig. 32b). Using this circuit we can simulate experimental measurements of the system by probing the two ports and look at the phase and the amplitude of the measured signals. Since this gives us an estimate for the linewidth κ of the resonances, we can again approximate the lifetime. An example for such a simulated phase measurement is given in Fig. 34.

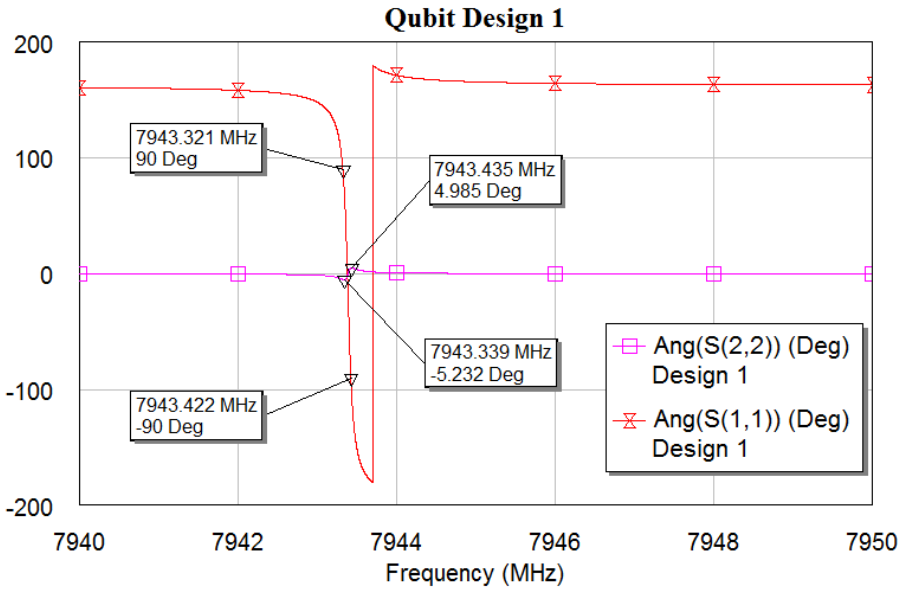

Figure 34: Example of a simulation for the equivalent circuit of qubit design 1, the linewidth for the resonator probe (port2) amounts to 101 kHz.

	Design 1	Design 2
E_c [MHz]	379	404
g [MHz]	48	39
T_1 [μs]($admittance$)	23.5	24.0
T_1 [μs]($Maxwell$)	1.58	3.00

Table 4: Designed parameters for the two different qubit designs.

Note that the SQUID loop is approximated as an inductor in the simulations. Further, the value of E_j and thus also Δ is determined by the size of the two Josephson junctions as well as their oxide layer thickness.

For the experiments presented in this thesis we used two slightly different qubit designs. The second design is chosen to have a lower resonator coupling g and also a higher maximal detuning from the resonator Δ_{max}, in order to reduce the Purcell decay rate (Eq. (70)), as this seems to be the main limitation for the relaxation time in our samples.

The simulated characteristic values of both designs as well as the lifetime approximations of both methods are summarized in Tab. 4. The difference in the two approximations of the lifetime shows, that for our samples the decay through the resonator is the limiting factor on the qubit lifetime, which is due to the fact that we have chosen a large decay rate κ of the resonator to enable for a fast decay of the single photon into the transmission line. Therefore, we could improve the theoretical T_1 time by lowering the coupling g between the qubit and the resonator.

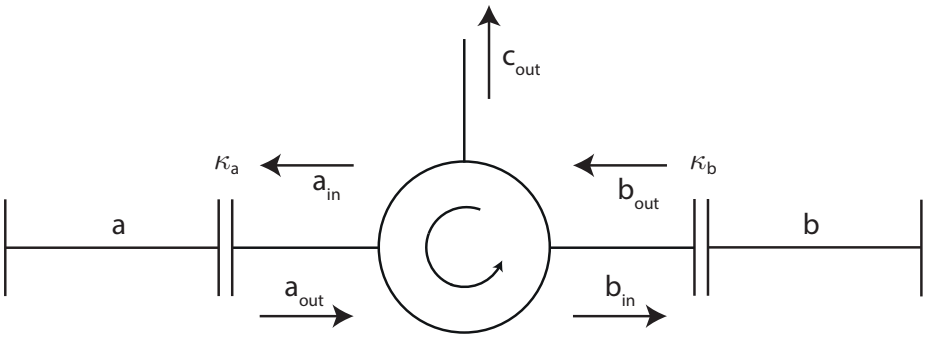

Figure 35: Circulator setup described by the fields and couplings within input-output theory.

6 Simulations with Master equation

Before realizing the setup we first performed some simulations of the system to get an idea of the possible success probabilities and their dependence on the system parameters. In a first step we looked at the system using input-output formalism to derive the interaction Hamiltonian between the two resonators.

6.1 Derivation of the Hamiltonian

We denote the fields in the the resonators with a and b, respectively, and the corresponding couplings are given by κ_a, κ_b, as shown in the Schematic in Fig. 35.

As the input for the second resonator is equivalent to the output of the first, only delayed by some time constant τ ($b_{in}(t) = a_{out}(t-\tau)$), we can assume $b_{in} = a_{out}$ as long as we can neglect losses in the cables or the circulator connecting the resonators. As there will be no microwave tone applied to the resonator a during the photon shaping, the input field is zero $a_{in} = 0$ and therefore we have

$$\begin{aligned} a_{out} &= \sqrt{\kappa_a}a, \\ b_{out} &= b_{in} + \sqrt{\kappa_b}b = \sqrt{\kappa_a}a + \sqrt{\kappa_b}b = c_{out}. \end{aligned} \tag{74}$$

The time evolution of the fields in the individual resonators is given by

$$\begin{aligned} \dot{a} &= \frac{i}{\hbar}\left[H_a, a\right] - \frac{1}{2}\kappa_a a, \\ \dot{b} &= \frac{i}{\hbar}\left[H_b, b\right] - \frac{1}{2}\kappa_b b - \sqrt{\kappa_b\kappa_a}a, \end{aligned} \tag{75}$$

where we used that $a_{in} = 0$ and $b_{in} = \sqrt{\kappa_a}a$ and H_a, H_b denote the Hamiltonian of the corresponding independent systems.

As we want to realize a perfect state transfer, nothing should be reflected at the second resonator and therefore in this simplified system we can assume that everything that would leave the system is dissipated. Later this energy will be used to excite the second qubit and thus complete the state transfer. For a system including dissipation the time evolution of an operator X is in general given by

$$\dot{X} = \frac{i}{\hbar}\left[H_{sys}, X\right] + L^\dagger X L - \frac{1}{2}\left(X L^\dagger L + L^\dagger L X,\right) \tag{76}$$

where L is the dissipator. Therefore, we can describe the time evolution of the resonator fields taking into account the whole dynamics system by choosing $L = c_{out}$ and we get

$$\begin{aligned} \dot{a} &= \frac{i}{\hbar}\left[H_a, a\right] + \frac{i}{\hbar}\left[H_{int}, a\right] - \frac{1}{2}\kappa_a a - \frac{1}{2}\sqrt{\kappa_a \kappa_b} b, \\ \dot{b} &= \frac{i}{\hbar}\left[H_b, b\right] + \frac{i}{\hbar}\left[H_{int}, b\right] - \frac{1}{2}\kappa_b b - \frac{1}{2}\sqrt{\kappa_a \kappa_b} a. \end{aligned} \tag{77}$$

Here the yet unknown interaction Hamiltonian enters which nwe need to choose to reproduce Eq. (75). Comparing Eq. (75) with Eq. (77) leads to

$$\begin{aligned} \frac{i}{\hbar}\left[H_{int}, a\right] &= \frac{1}{2}\sqrt{\kappa_a \kappa_b} b, \\ \frac{i}{\hbar}\left[H_{int}, b\right] &= -\frac{1}{2}\sqrt{\kappa_a \kappa_b} a. \end{aligned} \tag{78}$$

Choosing the ansatz $H_{int} = \lambda a^\dagger b + \lambda^* b^\dagger a$ finally gives

$$\begin{aligned} -\frac{i}{\hbar}\lambda b = \frac{1}{2}\sqrt{\kappa_a \kappa_b} b \quad &\longrightarrow \quad \lambda = i\frac{\hbar}{2}\sqrt{\kappa_a \kappa_b} \\ \frac{i}{\hbar}\lambda^* a = \frac{1}{2}\sqrt{\kappa_a \kappa_b} a \quad &\longrightarrow \quad \lambda^* = -i\frac{\hbar}{2}\sqrt{\kappa_a \kappa_b} \end{aligned} \tag{79}$$

and we can express the interaction Hamiltonian as follows

$$H_{int} = i\frac{\hbar}{2}\sqrt{\kappa_a \kappa_b}\left(a^\dagger b - b^\dagger a\right). \tag{80}$$

If we also want to include losses in between the two resonators we can assume that $b_{in} = \eta a_{out}$, meaning that we introduce an additional dissipator $L = \sqrt{(1-\eta^2)\kappa_a} a$, which is equivalent to adding a beamsplitter into the path between the resonators.

Now we can write down the full Hamiltonian of the system including the qubits

$$\begin{aligned} \frac{H}{\hbar} = &\sum_{i \in \{r_1, q_1, r_2, q_2\}} \delta_i a_i^\dagger a_i + \sum_{i \in \{q_1, q_2\}} \frac{1}{2}\alpha_i a_i^\dagger a_i^\dagger a_i a_i + \frac{1}{2}\left(\Omega_i(t) a_i^\dagger + \Omega_i^*(t) a_i\right) \\ &+ \sum_{i,j \in \{r_1, q_1, r_2, q_2\}} g_{ij} a_i^\dagger a_j, \end{aligned} \tag{81}$$

where g_{ij} is given by

$$g_{ij} = \begin{pmatrix} 0 & g_1 & \frac{i}{2}\sqrt{\kappa_1 \kappa_2} & 0 \\ g_1 & 0 & 0 & 0 \\ -\frac{i}{2}\sqrt{\kappa_1 \kappa_2} & 0 & 0 & g_2 \\ 0 & 0 & g_2 & 0 \end{pmatrix}. \tag{82}$$

6.2 Drive pulse

Having the Hamiltonian we have to derive the conditions for the drive, such that we can achieve a perfect transmission of the photon. The derivation of these conditions is analogous to [23]. The state of the system can be described by

$$|\Psi(t)\rangle = \alpha_1(t)\,|f0g0\rangle + \alpha_2(t)\,|g0f0\rangle + \beta_1(t)\,|g1g0\rangle + \beta_2(t)\,|g0g1\rangle\,. \tag{83}$$

The condition for the perfect state transfer without any reflection can be expressed as $c_{out}\,|\Psi\rangle = 0$, which directly leads to the condition $\beta_1 + \beta_2 = 0$. For now we assume that the system consists of two perfectly identical resonator-qubit systems, in particular this means that $\kappa = \kappa_a = \kappa_b$ and $g_1 = g_2 = g$, also we set $\hbar = 1$. Now we can look at the time evolution of the system given by

$$|\dot{\Psi}(t)\rangle = -iH_{int}\,|\Psi(t)\rangle\,, \tag{84}$$

where

$$\begin{aligned} H_{int} =& i\tilde{g}_1(t)\left(|g\rangle_1\langle f|_1\,a_1^\dagger - |f\rangle_1\langle g|_1\,a_1\right) + i\tilde{g}_2(t)\left(|g\rangle_2\langle f|_2\,a_2^\dagger - |f\rangle_2\langle g|_2\,a_2\right) \\ &+ \frac{i}{2}\kappa\left(a_1^\dagger a_2 - a_2^\dagger a_1\right), \end{aligned} \tag{85}$$

now also includes the effective coupling Hamiltonian (Eq. (49)). Here the effective couplings are proportional to the drive applied to the corresponding system $\tilde{g}_i(t) \propto g\Omega_i(t)$. This allows us to get the evolution of the coefficients from

$$\begin{aligned} |\dot{\Psi}(t)\rangle =& \dot{\alpha}_1(t)\,|f0g0\rangle + \dot{\alpha}_2(t)\,|g0f0\rangle + \dot{\beta}_1(t)\,(|g1g0\rangle - |g0g1\rangle) \\ =& \tilde{g}_1\,(\alpha_1(t)\,|g1g0\rangle - \beta_1(t)\,|f0g0\rangle) + \tilde{g}_2\,(\alpha_2(t)\,|g0g1\rangle + \beta_1(t)\,|g0f0\rangle) \\ &- \frac{\kappa}{2}\beta_1(t)\,(|g1g0\rangle + |g0g1\rangle)\,, \end{aligned} \tag{86}$$

leading to

$$\dot{\alpha}_1(t) = -\tilde{g}_1(t)\beta_1(t) \tag{87}$$

$$\dot{\alpha}_2(t) = \tilde{g}_2(t)\beta_1(t) \tag{88}$$

$$\dot{\beta}_1(t) = \tilde{g}_1(t)\alpha_1(t) - \frac{1}{2}\kappa\beta_1(t) = -\tilde{g}_2(t)\alpha_2(t) - \frac{1}{2}\kappa\beta_1(t). \tag{89}$$

From the last equation we can derive a relation between $\tilde{g}_1(t)$ and $\tilde{g}_2(t)$

$$\tilde{g}_2(t) = \frac{\kappa\beta_1(t) - \tilde{g}_1(t)\alpha_1(t)}{\alpha_2(t)}. \tag{90}$$

Besides that we also have the normalization condition

$$|\alpha_1(t)|^2 + |\alpha_2(t)|^2 + 2\,|\beta_1(t)|^2 = 1. \tag{91}$$

The problem now is to find drive pulses that fulfil these conditions. As we are trying to mimic a time reversed process for the second resonator we can restrict the solutions by assuming

$$\tilde{g}_2(t) = \tilde{g}_1(-t) \tag{92}$$

$$\alpha_1(t) = \alpha_2(-t). \tag{93}$$

This shows that the photon is shaped symmetrically as it implies $\beta_1(t) = \beta_1(-t)$, which can be seen by looking at the derivative

$$\frac{\mathrm{d}}{\mathrm{d}t}\beta_1(-t) = -\dot{\beta}_1(-t) = -\tilde{g}_1(-t)\alpha_1(-t) + \frac{1}{2}\kappa\beta_1(-t). \tag{94}$$

If we now choose the second half of the drive pulse $\Omega_1(t)$ for $t \geq 0$, the first half ($t < 0$) of the pulse is determined by Eq. (90) and the condition given by Eq. (92). Therefore, we can solve the problem by solving the two inhomogeneous differential equations (87) and (89). The corresponding initial conditions can be derived from the normalization condition Eq. (91) for $t = 0$

$$|\alpha_1(0)|^2 + |\beta_1(0)|^2 = \frac{1}{2} \tag{95}$$

and are given by

$$|\alpha_1(0)| = \sqrt{\frac{1}{2\left(1 + \frac{4g_1^2(0)}{\kappa^2}\right)}} \tag{96}$$

$$|\beta_1(0)| = \sqrt{\frac{\frac{4g_1^2(0)}{\kappa^2}}{2\left(1 + \frac{4g_1^2(0)}{\kappa^2}\right)}}. \tag{97}$$

6.2.1 Symmetric drive pulse

These equations can now be solved for different drive pulses. In general we would also like to keep the photon pulse as short as possible. Nevertheless, it cannot decay faster than $e^{-\kappa t/2}$, since the decay rate κ limits the photon emission rate, setting a lower bound for the slope of the pulse. Therefore, in contrast to the example chosen in [23], we choose a drive proportional to

$$\tilde{g}_1(t) = \frac{\kappa}{2\cosh\left(\frac{t\kappa}{2}\right)}, \tag{98}$$

for $t \geq 0$. Solving the differential equations with respect to this coupling leads to

$$\alpha_1(t) = \frac{1}{2\cosh\left(\frac{\kappa t}{2}\right)} e^{-\frac{\kappa t}{2}}, \tag{99}$$

$$\beta_i(t) = \frac{1}{2\cosh\left(\frac{\kappa t}{2}\right)}. \tag{100}$$

By plugging these equations into Eq. (90) it follows directly that the drive pulse is symmetric in time and therefore the couplings are given by

$$\tilde{g}_i(t) = \frac{\kappa}{2\cosh\left(\frac{t\kappa}{2}\right)}. \tag{101}$$

Another nice feature of this drive pulse is that the shape of the photon is proportional to the shape of the drive as $\tilde{g}_i(t) = \kappa\beta(t)$ and thus offers the possibility to generate short photon pulses. The time evolution of the coefficients is shown in Fig. 36. As discussed earlier, we need a symmetric shape of the photon to achieve ideal quantum state transmission. In combination we would like to keep the photon pulse as short as possible.

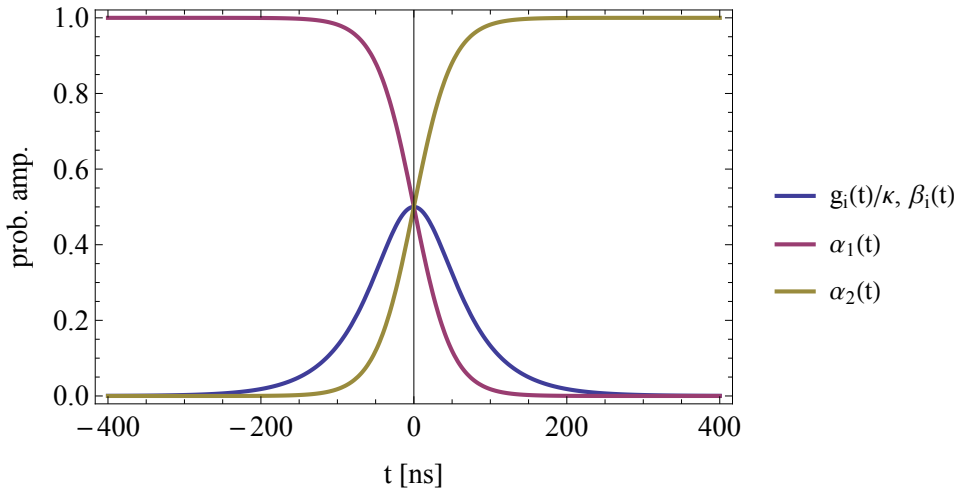

Figure 36: Time evolution of the coefficients of $|\Psi(t)\rangle$ for $\kappa = 40$MHz and a symmetric drive pulse proportional to $\tilde{g}_i(t)$ as defined in Eq. (101).

6.3 Simulations

Given everything that is required to describe the system theoretically we can simulate the process by solving the time dependent master equation

$$\dot{\rho}(t) = -i\left[H(t), \rho(t)\right] + \sum_i L_i \rho(t) L_i^\dagger - \frac{1}{2}\left(\rho(t) L_i^\dagger L_i - L_i^\dagger L_i \rho(t)\right), \tag{102}$$

where $H(t)$ is given by Eq. (81) and the L_i are the dissipators in our system. The only dissipator we consider for now is given by $L_1 = c_{out} = \sqrt{\kappa}(a_1 + a_2)$.

For our simulations we have several parameters which we can set to a fixed value or sweep during the simulations. We assume that the system consists of two perfectly identical samples, one for emitting and one for absorbing the photon. For now we also only consider a symmetric drive, as this provides the shortest photon shape. Besides the parameters of the samples, that is, the anharmonicity α, the couplings κ, g and the qubit-resonator detuning Δ, we also have to set the dimensions of the Hilbert space for qubits (dim_a) and resonators (dim_r) and the total duration of the drive pulse t_{max}. These have a large impact on the actual run time of the simulations, as they determine the dimensions of the density matrix and the time interval for which the master equation needs to be solved.

As mentioned in Sec. 3, we also need to correct for the difference of the AC-stark shift of the two energy levels, which enters as a phase factor $e^{i\phi(t)}$ for the drive in the rotating frame Hamiltonian. Otherwise, the two energy levels would not be perfectly on resonance which reduces the efficiency of the shaping scheme. Therefore, we determine the time-dependent energy difference between the $|f0\rangle$ and $|g1\rangle$ state for time steps dt and interpolate the total energy difference with respect to time in order to get the time dependent phase correction

$$\phi(t) = \int_0^t E_{f0}(\tau) - E_{g1}(\tau) \mathrm{d}\tau \approx dt \sum_{\tau=1}^{t/dt} E_{f0}(\tau) - E_{g1}(\tau), \tag{103}$$

which is then added to the drive. The time dependent energies are approximated by finding the closest eigenvectors and eigenenergies for the Hamiltonian at time t, with

respect to the density matrix corresponding to the states. Again we have a trade off between the accuracy and the run time of the simulations determined by the size of the time step dt. The last parameter we can choose is given by the amplitude of the drive Ω_0.

The simulations are done using *Mathematica*, where we define the Hamiltonian and the density matrices and implement the desired functions for estimating the eigenenergies as well as the phase correction. The parameters are loaded from an external file at the beginning of each iteration and after calculating the phase correction the time dependent density matrix is approximated by numerical integration of the master equation.

Finally we can determine the time dependent population of the various states ($|f1\rangle_{1,2}$, $|f1\rangle_{1,2}$, $|e1\rangle_{1,2}$, $|e0\rangle_{1,2}$, $|g1\rangle_{1,2}$, $|g0\rangle_{1,2}$) which we evaluate at times $t = 0$ to t_{max} in steps of 1 ns. These results are then stored in an external file, such that we can not only compare the final population of the $|f0\rangle_2$ state, but also can plot the complete time evolution of the system.

6.3.1 Unrealistic parameters

We started the simulations by taking into account two energy levels of the resonators and three of the qubits. The time steps for the phase corrections were set to $dt = 0.5$ ns and we fixed $\kappa/2\pi = 6$ MHz and $g/2\pi = 60$ MHz. For the first runs we chose some unrealistic values for the detuning $\Delta \in [4, 8]$ GHz and the anharmonicity $\alpha = 3.6$ GHz, in order to achieve high efficient state transfer without too much tuning of the parameters. By sweeping Δ, t_{max} and the amplitude of the drive Ω_0 we could easily reach 98.9% final population of the $|g0f0\rangle$ state.

In order to see if our simulation gives reasonable results we also compared it with a simulation done by solving the Schroedinger equation, where the effective, non-hermitian Hamiltonian taking into account the dissipation is given by [46]

$$H_{eff} = H - i\frac{1}{2}c_{out}^{\dagger}c_{out}. \tag{104}$$

As presented in Fig. 37 both methods give comparable results, showing that both descriptions are in good agreement.

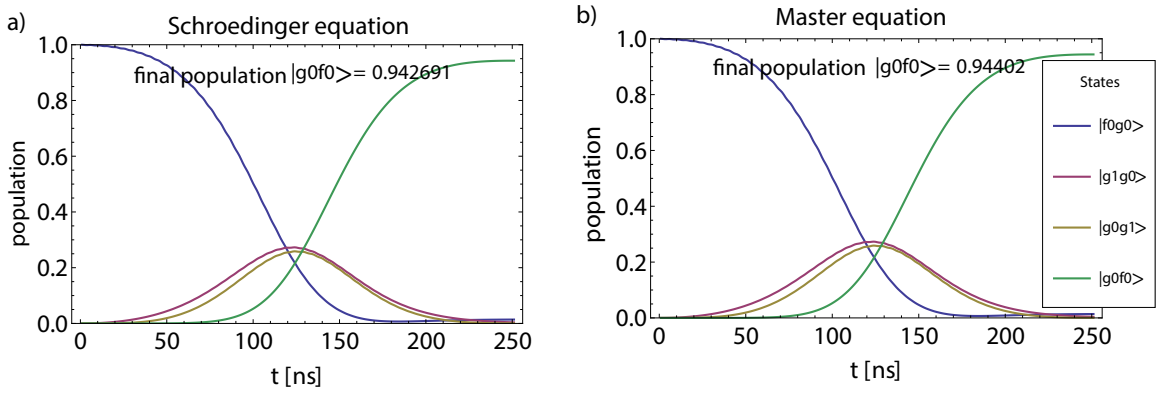

Figure 37: Comparison of the simulations using a) the Schroedinger equation and b) for the master equation for identical parameters. The graphs indicate the population of $|f0g0\rangle$ (blue), $|g1g0\rangle$ (red), $|g0g1\rangle$ (yellow) and $|g0f0\rangle$ (green).

parameter	value or range
dt	0.5 ns
dim_r	2
dim_q	4
$\alpha/2\pi$	300 MHz
$\kappa/2\pi$	6 MHz
$g/2\pi$	60 MHz
$\Delta/2\pi$	[1.3, 2] GHz
$\Omega_0/2\pi$	[50, 160] MHz
t_{max}	[250, 325] ns

Table 5: Values chosen for the simulations.

parameter	value or range
dt	0.5 ns
dim_r	2
dim_q	4
$\alpha/2\pi$	430 MHz
$\kappa/2\pi$	20 MHz
$g/2\pi$	50 MHz
$\Delta/2\pi$	[0.9, 1.1] GHz
$\Omega_0/2\pi$	[280, 460] MHz
t_{max}	[250, 325] ns

Table 6: Values chosen for the simulations.

6.3.2 Realistic parameters

In order to learn something about the process fidelity of the state transfer we need to go to more realistic parameters, which can be realized in our CQED systems. The parameters we have chosen for the next step of the simulations are summarized in Tab. 5. Note that we now also included four energy levels of the qubit, aiming for more accurate results.

After running the simulations with 249 different combinations of Δ, Ω_0 and t_{max} it was found that the maximal final population was 95% for the $|g0f0\rangle$ state. This shows that we should be able to realize high efficient state transfer in a CQED system using the proposed photon shaping scheme in combination with the chosen setup.

6.3.3 Sample parameters

The next step for the simulations was not only to consider realistic, but actual parameters of a fabricated sample. Therefore, we used the values of the design for the sample, which was used in the first run of measurements, as parameters for the simulations.

To get a first impression for the right intervals of the swept parameters, we start with simulations of random sets of these. From this we localize the interesting region and choose our intervals for a systematic sweep. The parameters are summarized in Tab.6.

In Fig. 38 we present a part of the results from over 1000 simulations done for these

parameters. The plots show the final population of the $|g0f0\rangle$ state depending on the parameters Δ, Ω_0 and t_{max}. In addition, the time evolution of the state populations for best result, leading to a final population of 84.7%, is given.

In parallel to the systematic sweep of parameters, we also simulated the efficiency for more than 2000 random sets of parameters. However, we could not reach higher values than with the systematic approach. As we are only reaching 84.7%, we tried to understand what limits the efficiency of the state transfer. Besides the Purcell effect, which leads to an overall decay in the system, an insufficient correction for the AC Stark effect would also cause a reduction of the maximal efficiency.

Therefore, we thought about a different way of approximating the phase, where the drive frequency is varied in order to find the frequency shift corresponding to the position of the energy level anti-crossing. This gives the change in the energy difference of the two states and by adding the constant offset due to the initial splitting of the energy levels, we can again interpolate the total energy difference with respect to time to get the time dependent phase correction. Nevertheless, implementing this new method for determining the phase due to the AC-stark shift did not lead to better results in terms of efficiency.

Subsequently we tried to use an asymmetric drive as derived in Appendix A using the factor k/κ, which determines the asymmetry as another sweeping parameter. Due to the asymmetry of the drive we needed to calculate two phase corrections, since we now have to apply the time reversed drive at the second qubit. Again we did simulations for more than 4000 sets of different parameter combinations, showing that the highest efficiency of 85.2% is still reached for the symmetric drive ($k = \kappa/2$).

Finally we could improve the result by additionally varying the initial value of the energy level splitting between the two states for the AC-Stark shift correction. Leading to the best obtained efficiency of 90.5%.

After deciding to modify the design of our samples, in order to reduce the coupling $g = 39\,\mathrm{MHz}$, we checked with some simulations if this affects the efficiency of the process. As expected we could reach again 89.3% population of $|g0f0\rangle$ with a small number of iterations, showing that the changes done to the sample do not have a big impact on the success probability.

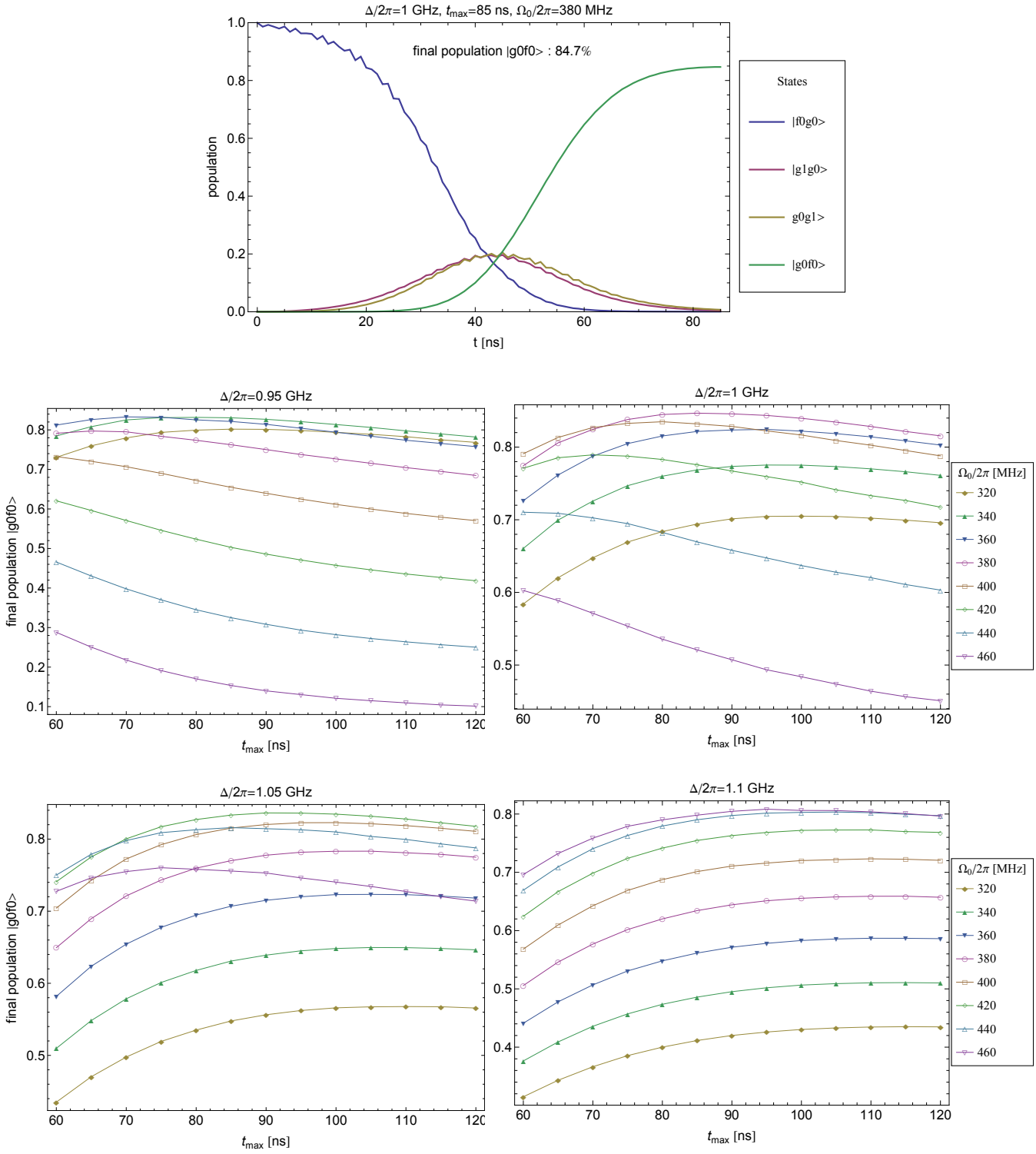

Figure 38: Time resolved population of the states for the highest state transfer efficiency for the given parameters and a cutout of the systematic sweep of Δ, Ω_0 and t_{max} for the parameters of sample 1. The four plots show the final population of the $|g0f0\rangle$ state for different values of Δ (specified at the top of each plot), dependent on t_{max} and Ω_0.

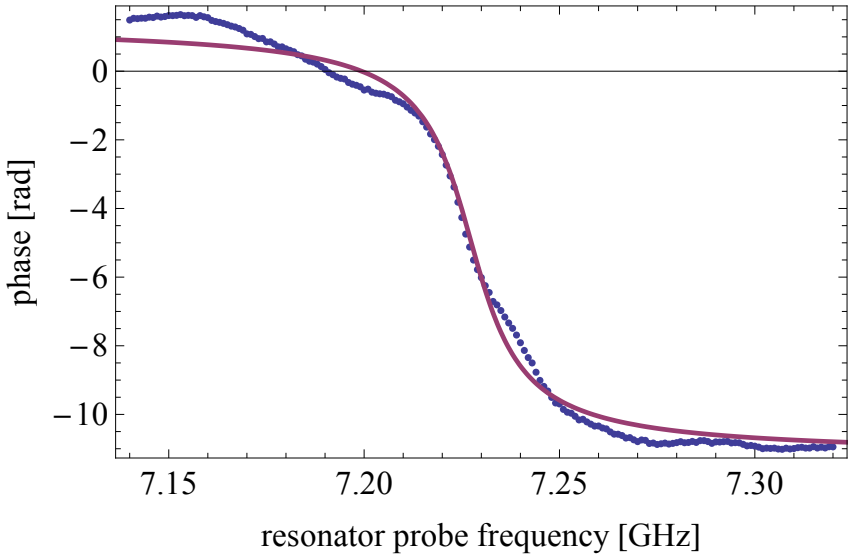

Figure 39: Reflection measurement of the two resonators (blue points) shown in combination with a theoretical fit (red), we can see the expected phase jump of 4π as both resonators are at the same frequency.

7 Experiment

In this section we will summarize the measurements, which were done using the two sample setup. All measurements were analyzed using *Mathematica*. First we will briefly introduce the standard measurements for characterizing the resonator and qubit frequencies as well as for determining the qubit lifetimes. In the following we show how we can characterize the samples in our new setup and specify the parameters of our system. Finally we present some first results on the photon shaping experiment using two slightly different methods.

7.1 Standard measurements

7.1.1 Resonator probe

To determine the resonator frequency we apply a probe tone to the resonator input and sweep the frequency. By measuring the phase of the reflected signal we can determine the resonator frequency. As discussed earlier the resonance results in a phase shift of 2π per resonator and we can fit the phase of a complex Lorentzian to the measurement data, see Fig. 39. As expected we get a phase jump of 4π. For the fit we assumed that both resonators are at the same frequency. To reliably determine the phase we use a reference signal by splitting the applied tone outside the dilution refrigerator. This allows to avoid the phase randomization of the microwave generator due to the change of the frequency.

7.1.2 Qubit spectroscopy

In analogy to the resonator probe tone we can also apply a probe tone at the gate line of the qubits, performing the so-called qubit spectroscopy. It allows to determine the transition frequency from $|g\rangle$ to $|e\rangle$ as well as higher order transitions if the applied power is strong enough. To measure this transition we again sweep the frequency of the microwave tone applied to the gate line of the qubit, while probing the resonator at its

resonance frequency. Due to the dispersive shift we can detect the change of the qubit state when driving the transition.

7.1.3 Rabi

To determine the energy relaxation time of our qubits we use so-called Rabi oscillations. Once we have determined the transition frequency ω_{ge} we can apply a pulse to the gate line using either a gated microwave generator or an IQ-mixer in combination with an arbitrary waveform generator. The latter method is better suited as it allows to use Gaussian pulses. In the first step one sweeps the amplitude of the applied pulse to find the value which corresponds to a π pulse, meaning a full swap of the excitation from the ground to the first excited state. After determining the amplitude we can measure the energy relaxation time by preparing the system in the excited state and measuring the residual population after different waiting times τ. The corresponding pulse scheme is shown in Fig. 40a). We expect to see an exponential decay with a decay rate $1/T_1$. By fitting the data we can extract T_1 (see Fig. 40b).

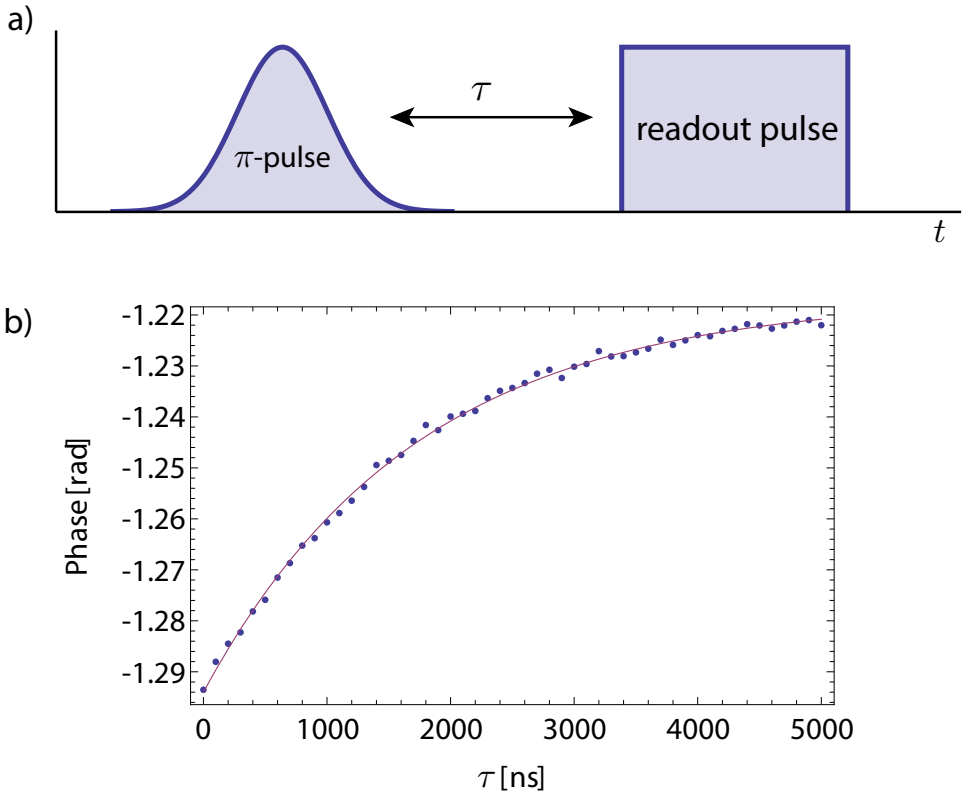

Figure 40: a) the pulse scheme for an energy relaxation measurement and b) a measurement (blue points) together with the theoretical fit (purple) for T_1 of the second design (sample A).

7.1.4 Ramsey

To extract the frequency of the qubit more precisely and to determine the dephasing time T_2 of the qubit we use a so-called Ramsey measurement. Here the qubit is prepared in a

superposition state by applying this time only a $\pi/2$ rotation to the qubit. After some time τ we apply again a $\pi/2$ pulse to swap the qubit excitation fully to the excited state. Also here we expect an exponential decay with a decay rate $1/T_2$. In addition we can detune the frequency of the preparation pulses which leads to sinusoidal oscillations of the measured signal due to the fact that the qubit Bloch vector in the rotating frame precesses around the z axis, causing the final excited state population to oscillate as a function of the waiting time τ. This allows us to correct the drive frequency as the frequency of the oscillations should be equal to the detuning from the ideal drive frequency.

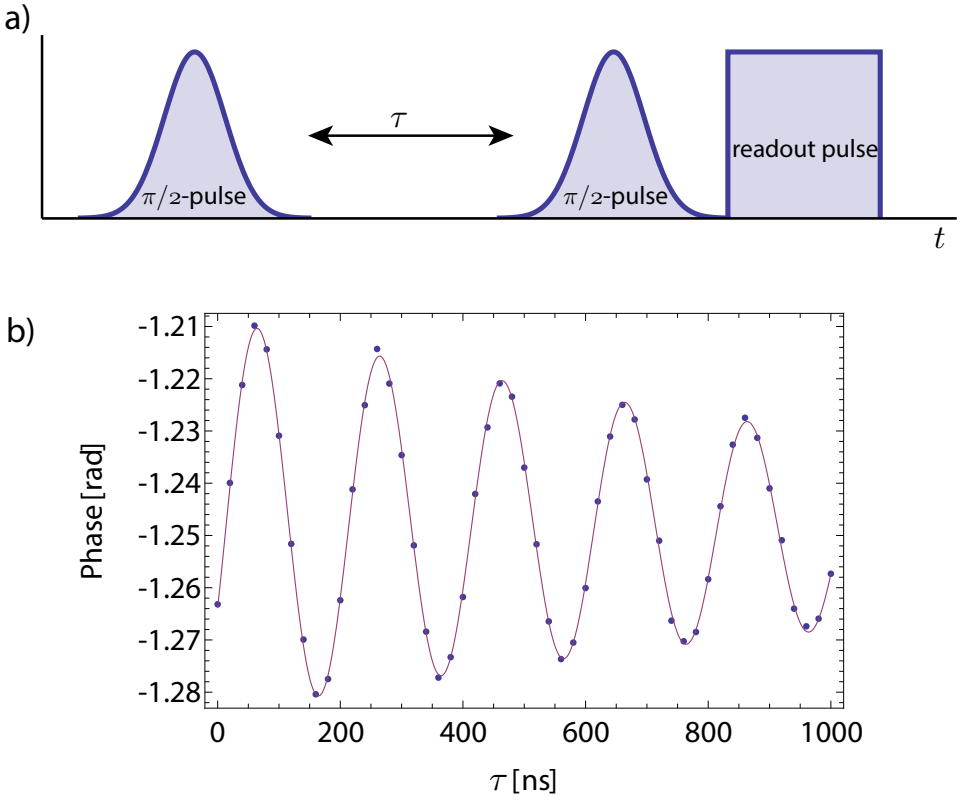

Figure 41: a) the pulse scheme for a measurement of the dephasing time and b) a measurement (blue points) together with the theoretical fit (purple) for T_{2ge} of the second design (sample A).

7.2 Sample characterization

7.2.1 Fitting avoided crossings - method 1

In the first run of experiments done with the new two sample setup we planned to test the setup and show that we can individually control and measure the samples. Subsequently we wanted to continue with the photon shaping experiments.

After the first cooldown of the system, spectroscopy measurements showed only one qubit and one resonator. In addition, we saw jumps in the qubit frequency of the working sample while changing the applied magnetic field. The origin of these jumps is not fully understood, but might be due to trapped vortices or current loops on the superconducting chip.

We decided to warm up the system in order to see if we can get rid of this jumping behavior of sample B. In addition we took a closer look at sample A again, trying to find the reason why it was not visible in our measurements. We decided to remove the airbridges above the resonator as these might have been collapsed, in addition we found a piece of dirt, probably bond wire, lying across one of the coupling capacitors of the resonator, which was also removed.

After cooling down the system again we could now see both of the samples, unfortunately the qubit frequency of sample B was still jumping while continuously changing the applied magnetic field. Therefore, we concentrated on determining some of the characteristic parameters of our samples. Besides getting familiar with all the equipment and the measurement software, this offered the chance to study the standard methods for sample characterization and to realize these using reflection measurements.

In order to determine the resonator frequency and the coupling constant g we measured avoided crossings for both of our samples. This is done by measuring the phase of the reflected signal while sweeping the coil voltage and the resonator frequency. This effectively realizes a two dimensional sweep of qubit and resonator frequency and we therefore expect to see a behaviour similar to the simulations presented in Sec. 4.4.1. Due to the fact that we have removed the airbridges across one of the resonators, the resonator frequencies of our two samples differed by more than 100 MHz. Therefore, it was possible to look at each resonator individually, without taking into account the second sample at all.

For the analysis of the data we first localized the position of the resonances for each voltage, which is done by looking at the change of the phase between each voltage step. We chose this method because the derivative of the phase of a Lorentzian is given by a Lorentzian peak, which is easy to fit. The positions of the resonances are indicated by the orange dots in Fig. 42.

Having the position of the resonances we can fit the dressed frequencies close to the crossing, which are given by

$$\omega_{1,2} = \frac{\Delta}{2} + \omega_r \pm \sqrt{\left(\frac{\Delta}{2}\right)^2 + g^2}, \tag{105}$$

where for the measurement Δ can be expressed as $\Delta(V) = \beta(V - V_c)$. Here V_c gives the position of the crossing and β is a scaling factor giving the change of the qubit frequency per Volt. Using V_c, β, ω_r and g as fitting parameters we can get an estimate for the parameters of our system. The fit of the dressed frequencies is given by the red line in Fig. 42 and the fitted values are given in Tab. 7. These are in good agreement with the designed ones with the exception of the resonator frequency of sample A, which can be understood as a consequence of replacing the airbridges with wire bonds, as mentioned earlier.

The second, smaller crossing right next to the main crossing in Fig. 42 can be understood by simulating the system including non-zero thermal population of the higher qubit states, which shows that this is the crossing of the $gf/2$ transition.

7.2.2 Fitting avoided crossings - method 2

For the run with the second design of the qubits both samples were fabricated without airbridges and we managed to get two resonators at approximately the same frequency.

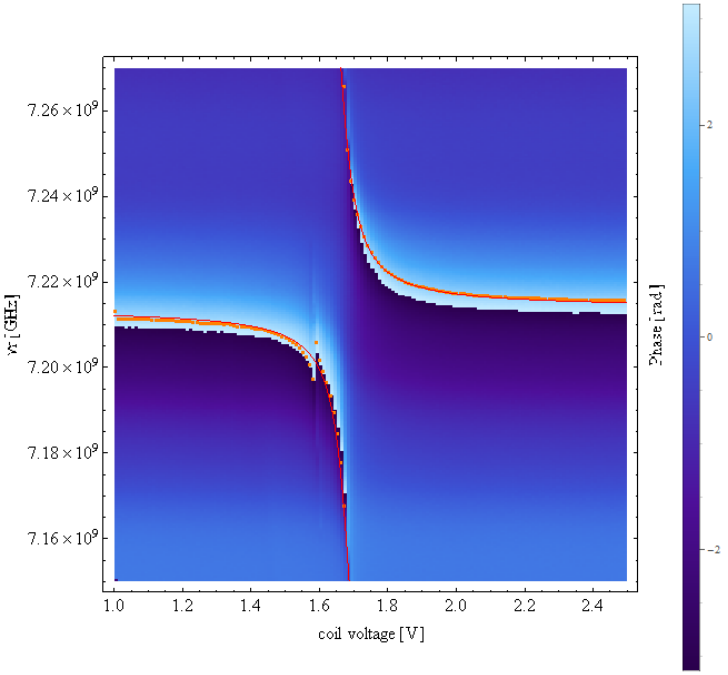

Figure 42: Avoided crossing of resonator and qubit measured with sample A. The orange dots indicate the fitted position of the resonances and the red line shows the fit of the dressed frequencies.

	Sample A	Sample B	Design
$g/2\pi$ [MHz]	46.8	50.6	48
$\omega_r/2\pi$ [GHz]	7.214	7.080	7.0

Table 7: Values of the parameters obtained from fitting the avoided crossings. The deviation of the resonator frequency of sample A is a consequence of the removed airbridges.

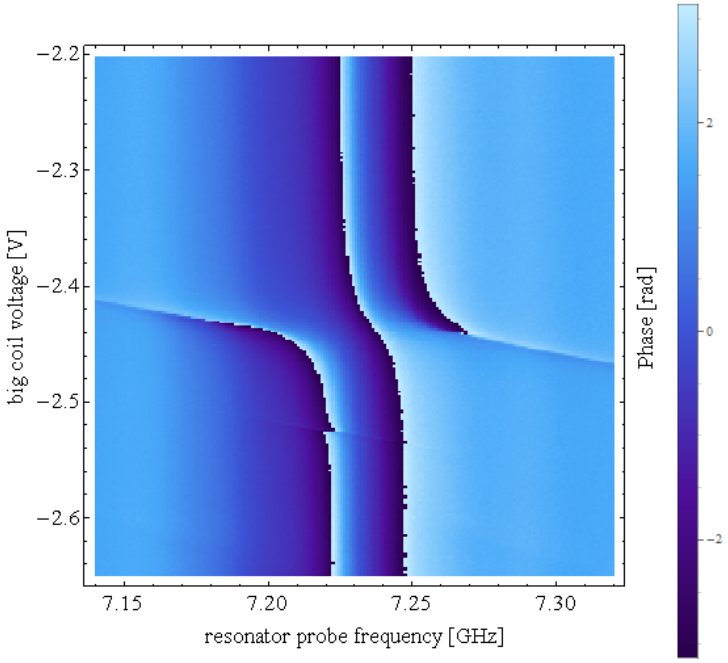

Figure 43: An avoided crossing of one of the qubits with the resonator, where now both resonators are at approximately the same frequency.

Therefore, we used a slightly different method for fitting the data, as we wanted to only look at the sample where the qubit is actually crossing the resonator. A plot of one of the crossings is given in Fig. 43.

We started by taking a reference measurement where the qubits are both far detuned from the resonators (Fig. 39). The phase obtained in this measurement was then subtracted from the measurement of the crossing. In this way we can eliminate the phase contribution from the resonator whose qubit is far detuned.

In the following we fitted the sine and the cosine of the phase ϕ to the theoretical value given by input-output theory. In contrast to directly fitting the phase this allows to circumvent possible problems with 2π phase discontinuities. The expression for the phase is in principle the same as derived in Sec. 4.4.1, with the difference that we have now also included a relaxation term for the qubit, which is assumed to decay at a rate Γ. This leads to the expression for the reflection coefficient given by

$$r = \frac{4g^2 + i(\Gamma + 2i(\omega_q - \omega)(2(\omega_r - \omega) + i\kappa)}{4g^2 + i(\Gamma + 2i(\omega_q - \omega)(2(\omega_r - \omega) - i\kappa)}. \tag{106}$$

We also need to subtract the phase coming from the bare resonator to compensate for the subtraction of the reference signal. This is given by setting $\omega_q = \Gamma = 0$. Now we can fit the data by minimizing the squared difference of the sine and cosine of the phases

$$Min\left[(\cos\phi_{fit} - \cos\phi_{meas})^2 + (\sin\phi_{fit} - \sin\phi_{meas})^2\right]. \tag{107}$$

The parameters that we used to fit the data are the coupling g and κ, the resonator frequency ω_r, the position of the crossing V_c and again also β which is defined as before and gives the frequency change of the qubit per unit voltage. Therefore, the qubit frequency can be expressed as $\omega_q(V) = \Delta(V) + \omega_r = \beta(V - V_c) + \omega_r$. The qubit decay rate was

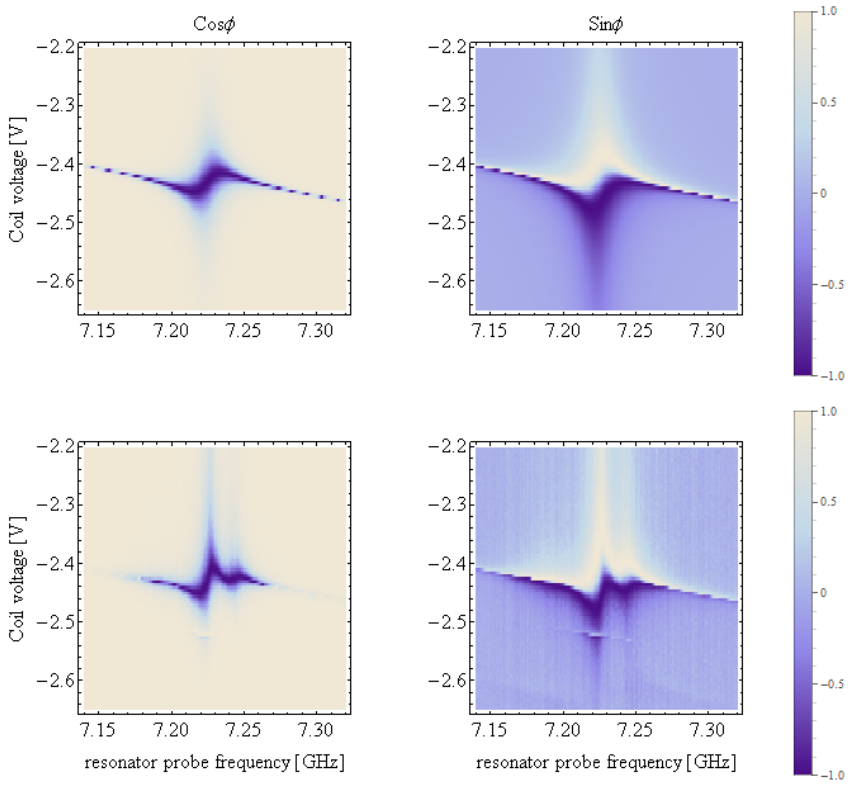

Figure 44: The fitted cos and sin of the phase (upper row), in comparison with the measurement data (lower row).

fixed to $\Gamma = 10^{-3}\,1/\text{ns}$. A result of the fit is shown in Fig. 44, where the upper row shows the fit and the lower row the measured data. In Addition we used the small crossing of the $gf/2$ transition to get an estimate for E_C. Here we used the fact that the distance between the two crossings is given by $\alpha/2$. Thus, we can use the scaling factor β to get the anharmonicity out of the positions of the two crossings. Subsequently we can then use this to approximate E_C and E_J at the crossing by minimizing

$$\left[(E_g(E_C,E_J)+E_f(E_C,E_J)-2E_e(E_C,E_J)-\alpha_{meas})^2+(E_e(E_C,E_J)-E_g(E_C,E_J)-\omega_q)^2\right], \tag{108}$$

where in this case $\omega_q = \omega_r$ since we are at the crossing. The values that we determined for the two samples out of fitting the crossings are given in Tab. 8 and are in quite good agreement with the designed values, again with the exception of the resonator frequencies which were shifted due to fabrication of the resonators with wirebonds instead of airbridges.

7.2.3 Qubit coherence times

Qubit design 1 As part of the characterization we also determined the energy relaxation T_1 and the dephasing T_2 times of the qubits by performing standard Rabi and Ramsey measurements. For the T_1 time of the $|f\rangle$ state we need to correct for the subsequent relaxation of the $|e\rangle$ state, using calibration measurements. The coherence times are determined at the sweetspot of the qubits. For sample B, which is jumping while

	Sample A	Sample B	Design
$g/2\pi$ [MHz]	35	37	39
$\kappa/2\pi$ [MHz]	24	18	20
$\omega_r/2\pi$ [GHz]	7.224	7.229	7.0
E_C [MHz]	406	392	404

Table 8: Values of the parameters obtained from fitting the avoided crossings. The deviation of the resonator frequency is a consequence of the the fabrication without airbridges.

	Sample A	Sample B
T_1 [ns]	1203	514
T_2 [ns]	1895	755
T_{1f} [ns]	334	305
T_{2gf} [ns]	228	206

Table 9: Measured coherence times for the qubits of design 1.

sweeping the coil voltage, we stopped a spectroscopy versus magnetic field measurement at a moment where the qubit was approximately at its sweetspot, resulting in a transition frequency of $\omega_q^B = 8.21\,\text{GHz}$. This was necessary because the jumps occur randomly and not in a reproducible fashion. Nevertheless, the qubit is stable as long as we do not change the coil voltage. For Sample A the maximal qubit frequency is given by $\omega_q^A = 8.22\,\text{GHz}$. The results of the measurements are summarized in Tab. 9. There is a great difference between the coherence times of the two samples for the ground state, which is assumed to be correlated with the jumping behavior of the qubit and the fact that we cannot be sure that the qubit is at its sweetspot. Due to the relatively low coherence times for the $|f\rangle$ state we decided to adjust the qubit design as discussed in Section 5.2.1.

Qubit design 2 The idea for the second design was to improve the coherence times of the qubit, as especially the coherence times of the $|f\rangle$ state were quite low for the first sample design. For the new sample the qubit sweetspot frequencies were given by $\omega_q^A = 8.67\,\text{GHz}$ and $\omega_q^B = 9.05\,\text{GHz}$. Due to the higher detuning the resulting dispersive shift of the resonator is smaller which leads to the fact that we need to average significantly more to be able to resolve the qubit. As a consequence we were not able to determine reliable values for the coherence times of the $|f\rangle$ state of the qubit of Sample B. The results presented in Tab. 10 show that we the effect of the changes in the design on the coherence times of the $|e\rangle$ state is very small, but for the $|f\rangle$ state we can actually see an improvement. In particular it seems that now T_{2gf} is mainly limited by T_{1f}.

7.2.4 Coil matrix

In order to be able to tune the qubits independently to arbitrary frequencies, we need to know which combinations voltages corresponds to which fluxes in the SQUID loops of our samples. Therefore, we perform qubit spectroscopy dependent on the magnetic field. As our qubits have a high detuning and are hard to resolve at higher frequencies, as mentioned earlier, we focused on the regions close to the resonator and voltage ranges

	Sample A	Sample B
T_1 [ns]	1721	1769
T_2 [ns]	1427	1119
T_{1f} [ns]	473	-
T_{2gf} [ns]	788	-

Table 10: Measured coherence times for the qubits of design 2. For Sample B it was not possible to get reliable data for the f state, possibly due to the large detuning.

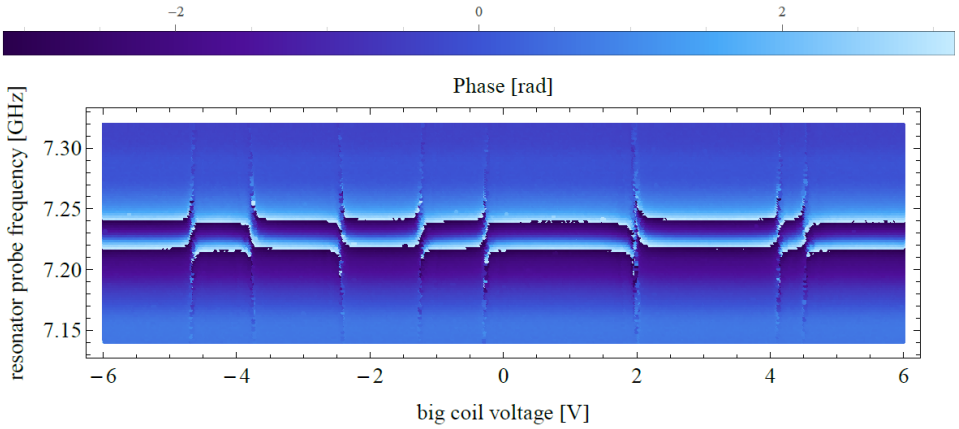

Figure 45: Sweep of the resonator probe frequency versus the voltage of the big coil. One can clearly identify that there are two working qubits crossing the resonators by looking at the directions of the crossings.

where we would expect a qubit to be in the regions. These were determined by a sweep of the resonator probe frequency and the magnetic field, whose results are shown in Fig. 45, and a rough qubit spectroscopy with only one of the qubits. This allowed us to determine which of the crossings belong to which qubit and therefore, we could zoom into the regions of interest.

After having measured the qubit spectroscopy for both samples and both coils, we fitted the dressed qubit frequencies to the data poinst. For this we first approximated the bare qubit frequency by

$$\omega_q = \sqrt{8E_C E_J \sqrt{\cos\left(\frac{\pi(V-V_0)}{V_p}\right) + \lambda}} - E_C, \tag{109}$$

where we used Eq. (27) and introduced an asymmetry for the SQUID loop, which improved the fit. In addition we have expressed the magnetic flux in terms of the coil voltage where V_0 represents a constant flux offset and V_p denotes the periodicity of the qubit frequency as a function of the voltage.

The dressed frequency is then given by

$$\omega_q^{dressed} = \frac{\omega_q + \omega_r}{2} \pm \sqrt{\left(\frac{\omega_q - \omega_r}{2}\right)^2 + g^2 \frac{\omega_q}{\omega_r}}. \tag{110}$$

In order to avoid over fitting we fixed some of the parameters in advance. Namely, we set

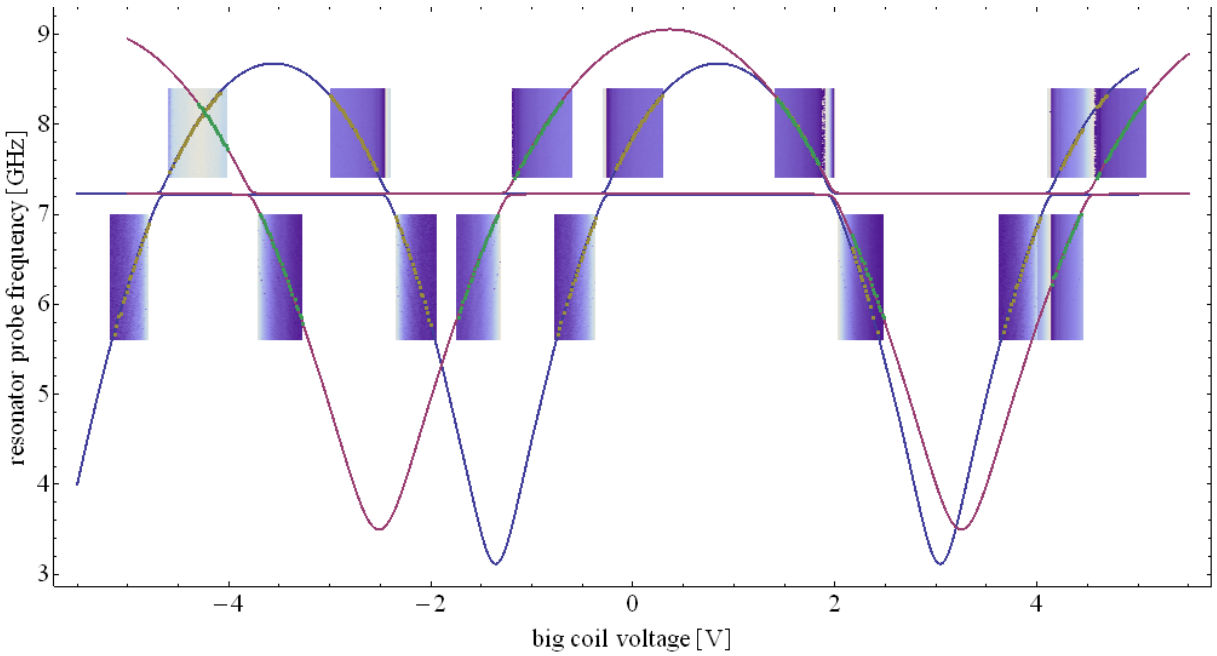

Figure 46: The data of the big coil sweep together with a fit for the dressed qubit frequencies. The blue curve and the yellow data points correspond to the qubit of sample A, whereas the red curve and the green data points correspond to the qubit of Sample B. The density plots show the qubit spectroscopy measurements in phase to determine the frequencies of the qubits as a function of the coil voltages.

E_C, g and ω_r to the values which we determined by fitting one of the avoided crossings (Tab. 8). This leaves use with the fitting parameters V_0, V_p, E_J and λ. The data for the sweep of the big coil together with the fitted qubit frequencies is shown in Fig. 46. The lower bound of the qubit frequencies indicates that the SQUID loops are asymmetric and we can actually compare the positions of the avoided crossings with the data shown in Fig. 45, which are in good agreement.

Now that we know the parameters for coils we can calculate the so-called coil matrix, which allows us to tune the qubit frequencies to arbitrary, independent values within the available range. For that we use the relation between the flux and the applied voltage for each sample and each coil obtained in the previous step. For example the flux on qubit A for a voltage applied on the big coil (coil 1) is given by

$$\Phi_A = \frac{\pi}{V_p^{(A1)}} V_1 + \frac{\pi V_0}{V_p^{(A1)}}, \tag{111}$$

Where the constant term gives a constant flux offset Φ_{0A}. This allows us now to caculate the flux dependence on the voltage of both coils by considering the vector equation

$$\begin{pmatrix} \Phi_A \\ \Phi_B \end{pmatrix} = M \begin{pmatrix} V_1 \\ V_2 \end{pmatrix} + \begin{pmatrix} \Phi_{0A} \\ \Phi_{0B} \end{pmatrix}, \tag{112}$$

where

$$M_{ij} = \frac{\pi}{V_p^{(ij)}}, \tag{113}$$

for $i = A, B$ and $j = 1, 2$. Now we can calculate the fluxes that we want to apply to the qubits by using the dressed frequency functions to solve for the flux corresponding to

	Sample A	Sample B
$\chi/2\pi$ [MHz]	1.8	2.2
$\kappa/2\pi$ [MHz]	21	17
$\omega_r/2\pi$ [GHz]	7.225	7.227

Table 11: The dispersive shift χ as well as the two additional fitting parameters.

the chosen qubit frequency and therefore we can get the voltage values by substituting everything into the equation

$$\begin{pmatrix} V_1 \\ V_2 \end{pmatrix} = M^{-1} \begin{pmatrix} \Phi_A - \Phi_{0A} \\ \Phi_B - \Phi_{0B} \end{pmatrix} \tag{114}$$

Thus, we have full control of sweeping our qubits frequencies independently by setting the correct coil voltages.

7.2.5 Dispersive shift and photon number

Another important quantity to characterize is the dispersive shift χ of the resonator, as this allows us to estimate the input power needed to excite on average one photon in the resonator in its steady state. To get the dispersive shift, we first measure the resonator spectrum for the qubit being in the $|g\rangle$ and in the mixed state (by strongly driving the qubit).

The two measurements are then subtracted from each other and fitted to the theoretical expected change of the phase, given by

$$f(\omega) = \arg\left[\frac{(\omega_r - \omega) + \frac{i}{2}\kappa}{(\omega_r - \omega) - \frac{i}{2}\kappa}\right] - \arg\left[\frac{(\omega_r - \chi - \omega) + \frac{i}{2}\kappa}{(\omega_r - \chi - \omega) - \frac{i}{2}\kappa}\right]. \tag{115}$$

As fitting parameters we used χ, κ and ω_r giving us another estimate for the resonator frequency and the decay rate. The values are presented in Tab. 11 and the dispersive shift is of the order of MHz. The other two parameters are slightly different in comparison to the values obtained from the avoided crossing (Tab. 8), showing that we still have some uncertainty about the actual values.

After getting an estimate for the dispersive shift we can now estimate the input power needed to populate the resonator with one photon on average. As the photon number in the resonator shifts the qubit frequency, we can estimate the power for one photon by performing qubit spectroscopy while sweeping the power of the resonator probe. The measurement of sample A is shown in Fig. 47, where the red points indicate the fitted qubit frequency. The power is obtained by fitting the qubit frequency to

$$\omega_q(p) = \omega_q^0 + 2\chi\frac{p}{p_0}, \tag{116}$$

where p_0 denotes the one photon power and ω_q^0 is the bare qubit frequency. Fitting this with ω_q^0 and p_0 as fit parameters we obtain $p_0 \approx -20.1\,\mathrm{dBm}$ for both samples.

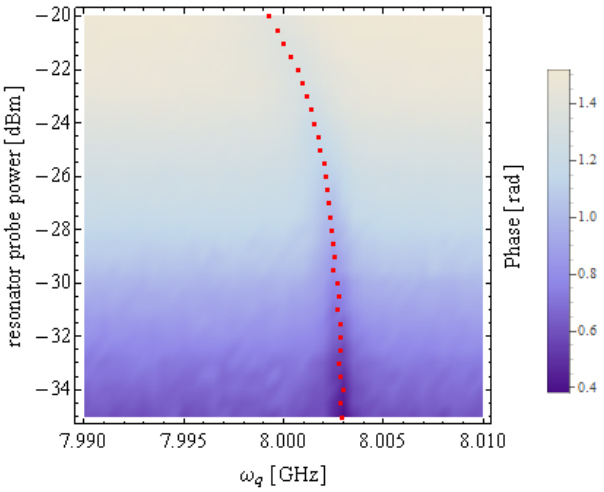

Figure 47: The AC-Stark shift of the qubit frequency due to the increasing power of the resonator probe for sample A, the red points correspond to the fitted qubit frequency.

7.3 Photon shaping

7.3.1 Polariton photon shaping

After the characterization of the two samples, we focused on Sample A, due to its better characteristics and stability with respect to coil voltage sweeps. In the next step we wanted to realize photon shaping to verify that we can shape and measure single photons within the new setup configuration. As it turned out we did not have enough power available at the input of the charge line to drive the second-order transition. We have therefore decided to try a modified version, using a first-order transition. Later we figured out that a wirebond connecting the launcher of the gate line to the PCB was broken causing the problems with the drive power. Still we continued our attempts to realize photon shaping using a first-order transition.

In order to do this we tuned the qubit and the resonator into resonance, which allows us to use the polariton states for our photon shaping procedure. We then prepare the qubit in the $|f\rangle$ state and apply the drive between the $|f0\rangle$ and the $|-,1\rangle$ states. The latter decays fast into the ground state by emitting a photon. A schematic of the procedure is given in Fig. 48.

The preparation of the $|f0\rangle$ state can be done by using a two photon transition from $|g\rangle$ to $|f\rangle$. To determine the corresponding transition frequency $\omega_{gf/2}$ we perform qubit spectroscopy with relatively high power to see the $gf/2$ transition. Now we can sweep the power of the transition pulse to realize Rabi oscillations, which allows us to determine the drive power corresponding to the full swap of the excitation.

After the system is prepared in the f state we can use again a spectroscopy measurement to find the frequency required to drive the system from $|f0\rangle$ to $|1,-\rangle$. Also here we use Rabi oscillations to determine the correct power for a full swap of the excitation. The last thing we have to consider is how to measure the single photon. If we want to measure the amplitude of the photon voltage we cannot prepare our system in the initial state $|f0\rangle$, but instead in a superposition state $(|g0\rangle + |f0\rangle)/\sqrt{2}$. This is due to the fact that the mean voltage $V \sim \langle a + a^\dagger \rangle$ of a Fock state is zero. As a consequence of this we need to measure the averaged emitted power if we want to observe a full photon.

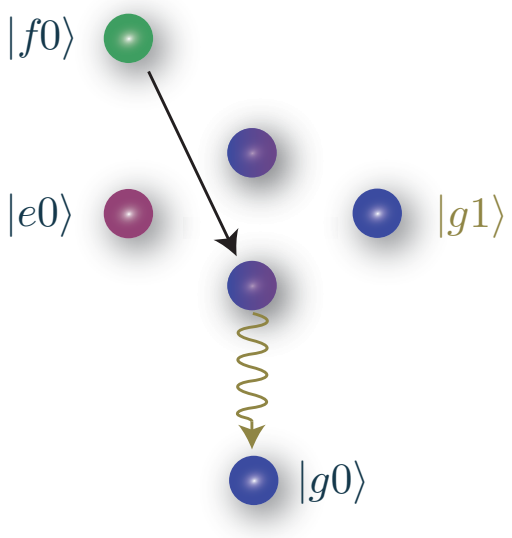

Figure 48: Schematic of the photon shaping method using one of the polariton states.

In Fig. 49a) a sweep of the $|f0\rangle \rightarrow |1,-\rangle$ drive amplitude is shown. Here we did not only measure the photon but also probe the resonator to resolve the qubit state after the emission of the photon. The first slice of the sweep as well as the slice indicated by the white dashed line are given in Fig. 49b). It is clearly visible that there is no photon if the drive amplitude is chosen to be 0, while there is a photon if we go to higher drive amplitudes. In addition we can see the change of the qubit state by looking at the resonator probe, where the different amplitudes correspond to the difference in the dispersive shift of the resonator due to the qubit state. The drive chosen for this experiments is of a simple Gaussian shape and the data is digitally filtered using a broadband Chebyshev filter in combination with a 4 point square filter.

After we successfully realized a single peaked photon we also wanted to generate a double-peaked single photon. This can be achieved by using two drive pulses, where the first one only transfers approximately half of the population from the $|f0\rangle$ state to the $|-,1\rangle$ state. Subsequently, a second, stronger and longer pulse is used to transfer all of the residual population, allowing to obtain a single photon with a two-peaked temporal shape. For these measurements we recorded the power as a function of time, which allows us to observe the photon also when we start with the initial state $|f0\rangle$. A measurement of a such a double-peaked single photon is given in Fig. 50. Here we can also see one problem of this shaping method. Due to the fact that we only use a first-order transition the $|f0\rangle$ state also naturally decays into the polariton state, leading to a competing photon-emission channel. In the measurement this is clearly visible as an exponentially decaying background signal indicated in Fig. 50 by a dashed line. Such a double-peaked photon would allow for time bin entanglement, which can also be used to encode a qubit state.

7.3.2 Second order photon shaping

In the last part of this work we tried to realize photon shaping using the second order transition within the new setup. We chose to work with sample A, as the detuning of the

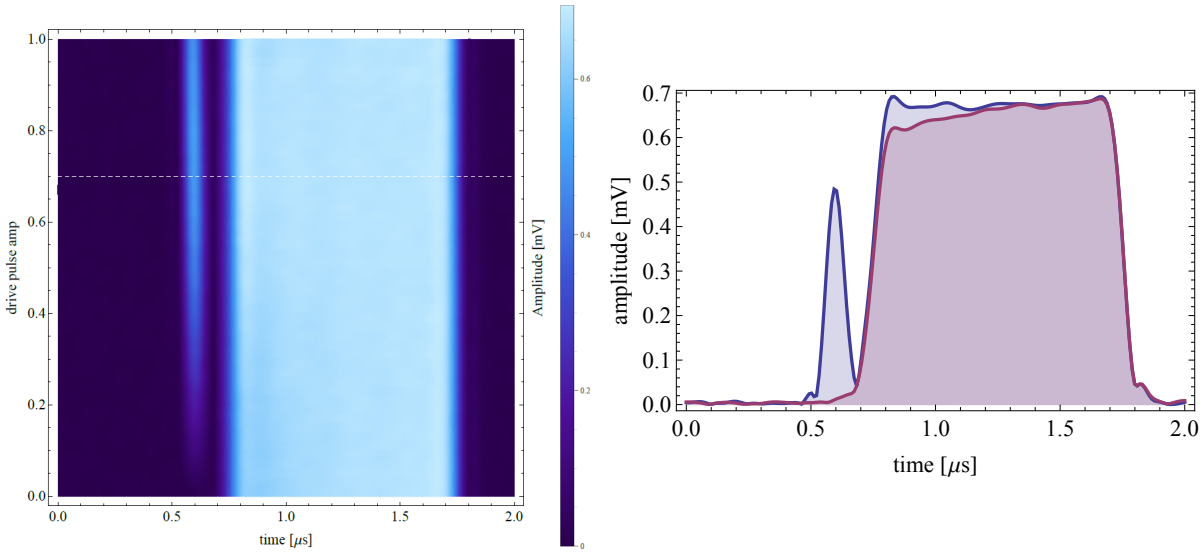

Figure 49: The plot in a) shows the change of the measurement time trace as the drive pulse amplitude is varied. The single photon and the resonator probe signal are measured in amplitude. In b) the first slice with zero drive amplitude (red) together with the slice indicated in a) by the white dashed line (blue) is given. One can clearly see the photon as well as the change of the qubit state indicated by the resonator probe.

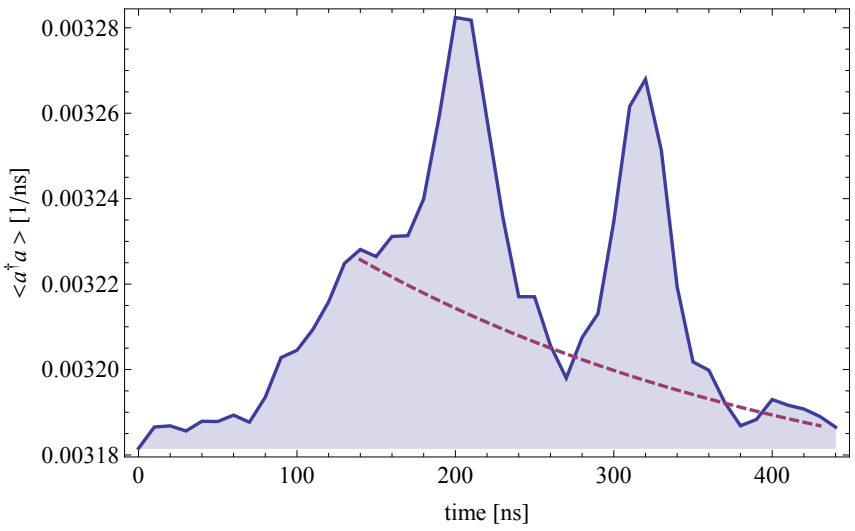

Figure 50: A double-peaked single photon measured in units of power per time. The red dotted line indicates the background signal due to the natural decay of the $|f0\rangle$ state.

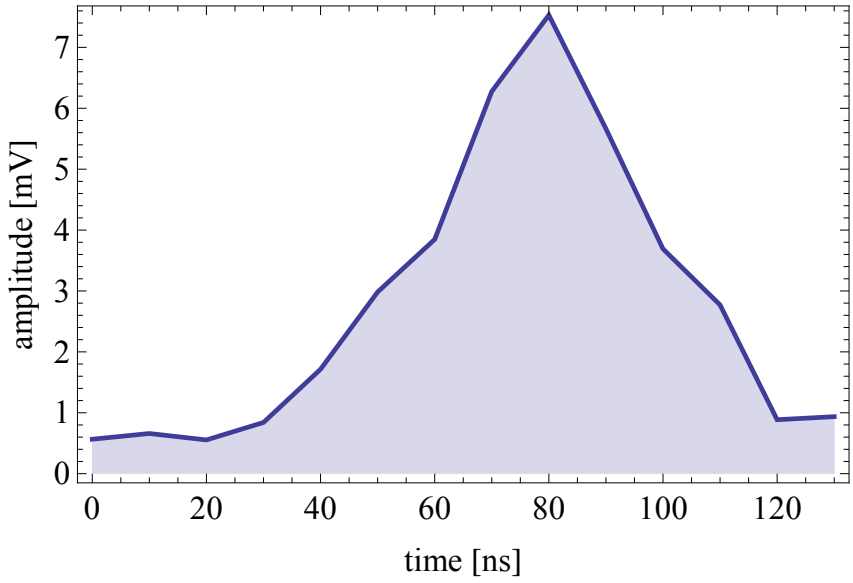

Figure 51: A single photon shaped using the second-order transition.

qubit is lower, leading to lower drive frequencies. Additionally in the final experiments involving both samples this will be the emitting one, as the photon can only travel from sample A to sample B, but not in reverse. For the process we use an IQ-mixer to prepare the qubit in the $|f\rangle$ state. This is done by using the right sideband for the transition pulse from $|g\rangle$ to $|e\rangle$ and the left sideband for the pulse from $|e\rangle$ to $|f\rangle$, where the transition frequencies are $\omega_{ge} = 8.639\,\mathrm{GHz}$ and $\omega_{ef} = 8.218\,\mathrm{GHz}$. A second IQ-mixer is then used to generate the drive pulse for the $|f0\rangle$ to $|g1\rangle$ transition, which is measured to be at $\omega_{f0g1} = 9.627\,\mathrm{GHz}$ and therefore in quite good agreement with the theoretically expected value of $\omega_{ge} + \omega_{ef} - \omega_r = 9.630\,\mathrm{GHz}$.

For the drive pulse we chose a slightly different drive than for the simulations given by

$$\Omega(t) = \Omega_0 \sin^2\left(\frac{\pi t}{T}\right) e^{i\phi(t)}, \tag{117}$$

which has similar characteristics but does not require an arbitrary cutoff.

We can tune the pulse amplitude Ω_0, the pulse duration T and the phase $\phi(t)$. The latter one needs to be adjusted to compensate for the AC-Stark shift dependent on the drive amplitude. The parameters T and Ω_0 need to be calibrated such that the photon shape is symmetric. The phase due to the AC-Stark shift can be approximated to be proportional to the square of the drive amplitude $|\Omega(t)|^2$ and we can sweep the proportionality factor as well as vary the detuning of the drive frequency to stabilize the phase of the single photon [43].

During the experiment we encountered problems with stabilizing the phase of the single photon, which might be due to the fact, that the photon is reflected at the second sample before we can measure it. As the frequency of the photon is quite close to the resonance frequency of the second resonator this could lead to an additionally acquired phase.

Nevertheless we could shape and measure single photons using the new setup. An example of a measured photon is given in Fig. 51.

8 Discussion and conclusion

8.1 Results

Throughout this work we have designed and built a solid state setup which allows to exchange a single photon between two distant samples connected by a coaxial cable. We realized an experimental setup of a two node quantum network which allows to measure quantum state transfer using single shaped photons.

After a brief introduction into superconducting qubits and circuit QED, we have given a description of the photon shaping method used in our experiments. We presented a microwave induced second-order coupling, which is fully controlled by the amplitude and the phase of an applied microwave drive and therefore does not need any other tuneable parameter. That is one advantage of our scheme compared to others realized for CQED systems [40, 42].

The setup was developed under the constraints of having a system that allows to exchange a single photon but does not couple the two samples directly. This was achieved by using a circulator in between the two samples, which also enables us to measure both samples through one detection line in reflection. Before installing the new setup inside the dilution refrigerator it was tested using dipstick measurements in liquid helium.

We have shown that it is theoretically possible to reach a high state transfer fidelity, using simulations of the system including the shaping method and the two sample setup as it was installed into the dilution refrigerator. Here we also took care about the constraints on our drive pulses and presented analytic solutions of a simplified system used to choose a reasonable shape of the drive pulse for the full master equation simulations. By optimizing the AC-Stark shift correction we could finally reach around 90 % population transfer, where the main limitation seems to be given by the sample parameters.

In the first experiments measured within the new setup we have shown that we have full control over the individual samples. We presented how the two samples can be characterized using slightly modified methods compared to the standard characterization measurements. In addition we modified the qubit design to get better coherence times, where we also estimated an upper bound for T_1 using an equivalent microwave circuit for our qubit-resonator system.

Finally we showed that it is possible to shape single photons using the microwave induced coupling, first by using a first-order transition and one of the polariton states and subsequently with the second order-method transition as presented in the theory part.

This shows, that we have a working setup for realizing quantum state transfer using single shaped photons by using a microwave induced second order coupling between the resonator and the qubit.

8.2 Outlook

To be able to efficiently realize quantum state transfer we still need to work on the sample design and fabrication to get two nicely working, identical samples with good coherence times. Having this, we could realize quantum state transfer between two distant nodes of a quantum network for the first time in a solid state setup, by shaping and absorbing single photons.

In addition we would like to look at the time-bin entanglement of a double peaked, single photon, which would allow to encode a qubit in time bins [50]. In contrast to encoding the qubit states according to $|g\rangle \rightarrow |0\rangle$ and $|e\rangle \rightarrow |1\rangle$ this method allows to detect if the photon was lost during the transfer as the qubit is encoded only in the arrival time, which means that there is always a photon present if the transfer was successful. In addition this type of entanglement allows also for a larger Hilbert space as we can use more than two time-bins.

Finally a setup as presented in this thesis could be used to realize entanglement distribution [51] and would enable for teleportation experiments over larger distances as well as for example loophole-free Bell-tests. Also it could server as a basis for developing quantum repeaters which would allow for quantum state transfer over even larger distances [52].

It would also be interesting to investigate the discussed photon shaping schemes in other types of qubits, which would allow for higher anharmonicities. As the simulations with higher anhamonicity showed, this would enable for higher state transfer efficiency. One interesting candidate would be the Fluxonium qubit [53], which is insensitive to offset charges like the transmon but allows for larger anharmonicity.

This shows that there is still a lot of interesting experiments that can be realized using such a setup and it will be interesting to go on investigating such a system and realize the next steps towards a quantum network.

A Asymmetric drive pulse

Besides the symmetric drive pulse we also wanted to look at an asymmetric drive, where we can tune the asymmetry in order to see if this allows for a more efficient state transfer.

To derive the conditions for the asymmetric drive, we used the formalism of quantum trajectories, which turns out to be more convenient than solving the equations given above. The emitting part of our system can be described by an initial state

$$|\psi(t)\rangle = \alpha(t)\,|f0\rangle + \beta(t)\,|g1\rangle\,, \tag{118}$$

where $|g1\rangle$ can decay at a rate κ into $|g0\rangle$ by emitting a photon. After emitting the photon the system is trapped in the $|g0\rangle$ state, as the drive in the system is off resonant from any transition involving that state. Therefore the evolution of the state vector is given by the stochastic Schroedinger equation

$$\frac{\mathrm{d}}{\mathrm{d}t}\,|\psi(t)\rangle = -i\psi\left[H(t) - i\frac{\kappa}{2}\,|g1\rangle\,\langle g1|\right]|\psi(t)\rangle\,, \tag{119}$$

where the emission of the photon enters as a dissipative term, resulting in a non-unitary evolution. To get the probability amplitude for emitting a photon in $[t,\, t+\mathrm{d}t]$ we look at the time derivative of the probability of the system not being decayed into $|g0\rangle$, which is given by $\langle\psi(t)|\psi(t)\rangle$, leading to

$$\frac{\mathrm{d}}{\mathrm{d}t}\,\langle\psi(t)|\psi(t)\rangle = \left(\frac{\mathrm{d}}{\mathrm{d}t}\,|\psi(t)\rangle\right)^{\dagger}|\psi(t)\rangle + \langle\psi(t)|\left(\frac{\mathrm{d}}{\mathrm{d}t}\,|\psi(t)\rangle\right) = -\kappa\,|\beta(t)|^2\,. \tag{120}$$

Thus, the probability amplitude is given by $\langle g1|\psi(t)\rangle\,\sqrt{\kappa\mathrm{d}t}$. This allows us to write down the state of the system in combination with the propagating field which is given by

$$|\Psi(t)\rangle = |\psi(t)\rangle\otimes|0\rangle + |g0\rangle\otimes\sqrt{\kappa}\int_0^t \beta(\tau)a_{out}^{\dagger}(\tau)\,|0\rangle\,\mathrm{d}\tau, \tag{121}$$

where $a_{out}^{\dagger}(t)$ creates a photon in the propagating field, which is emitted in the time interval $[t, t+\mathrm{d}t]$. In the end we want to emit a single photon with a given shape $f(t)$, where the final state after the process is given by

$$|\Psi_f\rangle = |\psi(t_f)\rangle\otimes|0\rangle + |g0\rangle\otimes\sqrt{\kappa}\int_0^{t_f} f(\tau)a_{out}^{\dagger}(\tau)\,|0\rangle\,\mathrm{d}\tau. \tag{122}$$

By comparing this to Eq. (121) we get the condition

$$\sqrt{\kappa}\beta(t) = f(t), \tag{123}$$

giving a direct relation between the shape of the photon and the probability amplitude of the $|g1\rangle$ state.

In a last step we want to express this condition now in terms of the properly normalized state vector

$$|\psi_n(t)\rangle = \frac{|\psi(t)\rangle}{\sqrt{\langle\psi(t)|\psi(t)\rangle}}. \tag{124}$$

From Eq. (120) we know that

$$\frac{\mathrm{d}}{\mathrm{d}t}\langle\psi(t)|\psi(t)\rangle = -|f(t)|^2, \tag{125}$$

allowing us to reformulate the condition, giving

$$\sqrt{\kappa}\,\langle g1|\psi_n(t)\rangle = \frac{f(t)}{\sqrt{1-\int_0^t |f(\tau)|^2 \mathrm{d}\tau}}. \tag{126}$$

Thus we can choose a photon shape $f(t)$ and determine the coefficients $\alpha(t)$, $\beta(t)$ and the drive $\Omega(t)$.

For the state

$$|\psi_n(t)\rangle = \cos\frac{\theta(t)}{2}\,|f0\rangle + \sin\frac{\theta(t)}{2}\,|g1\rangle \tag{127}$$

and the interaction Hamiltonian

$$H(t) = i\frac{\Omega(t)}{2}\left(|g1\rangle\langle f0| - |f0\rangle\langle g1|\right), \tag{128}$$

we can derive the condition for the drive depending on the coefficients of the normalized state, leading to

$$\Omega(t) = \dot{\theta} + \kappa \sin\frac{\theta(t)}{2}\cos\frac{\theta(t)}{2}. \tag{129}$$

As discussed earlier, we need a symmetric and fast decaying shape of the photon, in order to achieve efficient quantum state transmission. It turns out that these criteria are satisfied by the following function

$$|f(t)| = \frac{\sqrt{k}}{\sqrt{2}\cosh kt}, \tag{130}$$

where $k \leq \kappa/2$. For the case of $k = \kappa/2$, $|f(t)|$ is proportional to the shape of the photon of the symmetric drive pulse. Now we can use Eq. (126) to determine the coefficients of the wave function, leading to

$$\sin\frac{\theta(t)}{2} = \sqrt{\frac{k}{\kappa}}\frac{e^{\frac{kt}{2}}}{\sqrt{\cosh kt}}, \tag{131}$$

$$\cos\frac{\theta(t)}{2} = \frac{\sqrt{\cosh kt - \frac{k}{\kappa}e^{kt}}}{\sqrt{\cosh kt}}. \tag{132}$$

By looking at the time derivative of one of these coefficients we get

$$\dot{\theta} = k\sqrt{\frac{k}{\kappa}}\frac{e^{\frac{-kt}{2}}}{\cosh kt\sqrt{\cosh kt - \frac{k}{\kappa}e^{kt}}} \tag{133}$$

and according to Eq. (129) the drive pulse is given by

$$\Omega(t) = k\frac{\gamma(t) + \gamma(t)^{-1}}{\cosh kt}, \tag{134}$$

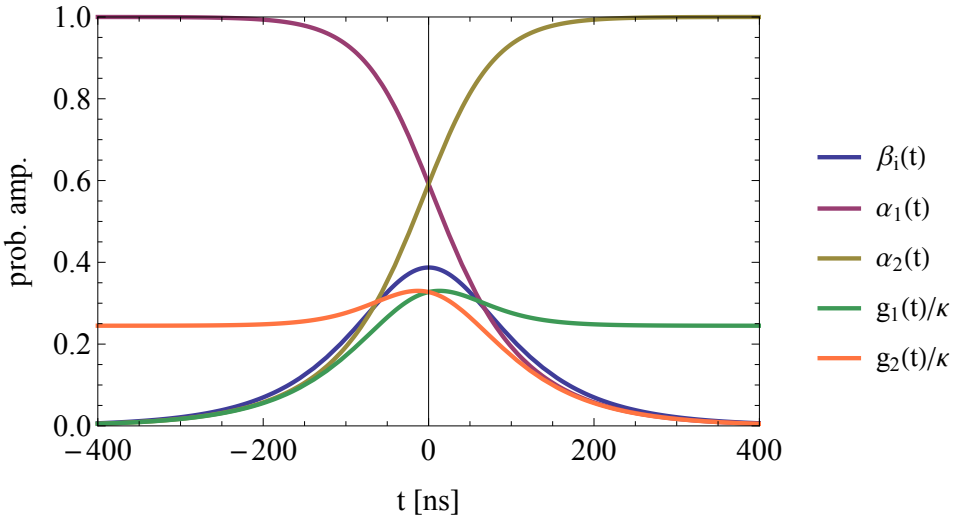

Figure 52: Time evolution of the coefficients of $|\Psi(t)\rangle$ for $\kappa/2\pi = 40\text{MHz}$ and $k = 0.3\,\kappa$ for an asymmetric drive pulse proportional to $g_i(t)$

where

$$\gamma(t) = e^{\frac{kt}{2}} \sqrt{\frac{\kappa}{k} \cosh kt - e^{kt}}. \tag{135}$$

Now we can derive the expressions for the wavefunction coefficients

$$\alpha(t) = \cos\frac{\theta(t)}{2} \sqrt{\langle\psi(t)|\psi(t)\rangle} = \frac{1}{\sqrt{2}} e^{-\frac{kt}{2}} \frac{\sqrt{\cosh kt - \frac{k}{\kappa} e^{kt}}}{\cosh kt}, \tag{136}$$

$$\beta(t) = \frac{f(t)}{\sqrt{\kappa}} = \frac{1}{\sqrt{2}} \frac{\sqrt{\frac{k}{\kappa}}}{\cosh kt}, \tag{137}$$

which give us the time resolved evolution of the state and in addition allows us to compare the results with the conditions derived from [23]. Comparing Eq. (85) and Eq. (128) we can express the coupling as

$$\tilde{g}_1(t) = \frac{\Omega(t)}{2} = k \frac{\gamma(t) + \gamma(t)^{-1}}{2 \cosh kt}. \tag{138}$$

Now we can easily convince ourselves, that these coefficients solve Eq. (87) and (89), showing that the derivation is consistent with the conditions for the drive.

The time evolution of the coefficients together with the couplings for $k = 0.3\,\kappa$ is given in Fig. 52. One can see that the photon is longer and that we now need to apply different drive pulses to the two qubits due to the asymmetry and the condition $g_1(t) = g_2(-t)$.

List of Figures

References

[1] H.J. Kimble. The quantum internet. Nature, 453:1023-1030, 2008

[2] R.P. Feynman. Simulating physics with computers. Int. J. Theor. Phys., 21:467-488, 1982

[3] D. Deutsch. Quantum theory, the Church-Turing principle ant the universal quantum computer. Proc. R. Soc. Lond. A, 400:97-117, 1985

[4] D. Deutsch and R. Jozsa. Rapid solution of problems by quantum computation. Proc. R. Soc. Lond. A, 439:553-558, 1992

[5] L.K. Grover. A fast quantum mechanical algorithm for database search. Proceedings of the twenty-eighth annual ACM symposium on Theory of computing, pages 212-219, 1996

[6] P.W. Shor. Polynomial-time algorithms for prime factorization and discrete logarithms in a quantum computer. SIAM Journal on Computing, 26:1484-1509, 1997

[7] R.L. Rivest, A. Shamir and, L. Adleman. A Method for Obtaining Digital Signatures and Public-Key Cryptosystems. Communications of the ACM, Volume 21 Issue 2, pages 120-126, 1978

[8] C.H. Bennett and G. Brassard. Quantum cryptography: public key distribution and coin tossing. International Conference on Computers, Systems & Signal Processing, Volume 1, pages 175-179, 1984

[9] A.K. Ekert. Quantum Cryptography Based on Bell's Theorem. Phys. Rev. Lett., 67:661-663, 1991

[10] C.H. Bennett and S.J. Wiesner. Communication via One- and Two-Particle Operators on Einstein-Podolsky-Rosen States. Phys. Rev. Lett., 69:2881-2884, 1992

[11] C.H. Bennett, G. Brassard, C. Crépeau, R. Jozsa, A. Peres, and W.K. Wootters. Teleporting an Unknown Quantum State via Dual Classical and Einstein-Podolsky-Rosen Channels. Phys. Rev. Lett., 70:1895-1899, 1993

[12] D.P. Di Vincenzo. The Physical Implementation of Quantum Computation. Fortschr. Phys. 48:771-783, 2000

[13] H. Häffner, C.F. Roos, R. Blatt. Quantum computing with trapped ions. Physics Reports 469:155-203, 2008

[14] P.Kok, W.J. Munro, K. Nemoto, T.C. Ralph, J.P. Dowling, and G.J. Milburn. Linear optical quantum computing with photonic qubits.Rev. Mod. Phys. 79:135-174, 2007

[15] J.J. Jones. Quantum computing with NMR. Process in Nuclear Magnetic Resonance Spectroscopy, 59:91-120, 2011

[16] C. Kloeffel and D. Loss. Prospects for Spin-Based Quantum Computing in Quantum Dots. Annu. Rev. Cond. Mat. Phys., 4:51-81, 2013

[17] M.H. Devoret and R.J. Schoelkopf. Superconducting Circuits for Quantum Information: An Outlook. Science, 339:1169-1174, 2013

[18] H. Walter, B.T.H. Varcoe, E.-G. Englert and T. Becker. Cavity quantum electrodynamics. Rep. Prog. Phys., 69:1325-1382, 2006

[19] A. Blais, R.-S. Huang, A. Wallraff, S.M. Girvin, and R.J. Schoelkopf. Cavity quantum electrodynamics for superconducting electrical circuits: An architecture for quantum computation. Phys. Rev. A, 69:062320, 2004

[20] A. Wallraff, D.I. Schuster, A. Blais, L. Frunzio, R.-S. Huang, J. Majer, S. Kumar, S.M. Girvin & R.J. Schoelkopf. Strong coupling of a single photon to a superconducting qubit using circuit quantum electrodynamics. Nature, 431:162-167, 2004

[21] A. Wallraff, D.I. Schuster, A. Blais, L. Frunzio, J. Majer, M.H. Devoret, S.M. Girvin, and R.J. Schoelkopf.Approaching unit visibility for control of a superconducting qubit with dispersive readout. Phys. Rev. Lett., 95,060501, 2005

[22] J. Majer, J.M. Chow, J.M. Gambetta, J. Koch, B.R. Johnson, J.A. Schreier, L. Frunzio, D.I. Schuster, A.A. Houck, A. Wallraff, A. Blais, M.H. Devoret, S.M. Girvin, and R.J. Schoelkopf. Coupling superconducting qubits via a cavity bus. Nature, 449;443-447, 2007

[23] J.I. Cirac, P. Zoller, H.J. Kimble, and H. Mabuchi. Quantum State Transfer and Entanglement Distribution among Distant Nodes in a Quantum Network. Phys. Rev. Lett., 78:3211-3224, 19997

[24] B.D. Josephson. Possible new effects in superconductive tunneling. Phys. Lett., 1:251-253, 1962

[25] B.D. Josephson. The discovery of tunneling supercurrents. Rev. Mod. Phys., 46:251-254, 1974

[26] J. Bardeen, L.N. Cooper, and J.R. Schrieffer. Theory of Superconductivity. Phys. Rev., 108:1775-1204, 1957

[27] M.H. Devoret, A. Wallraff, and J.M. Martinis. Superconducting Qubits: A Short Review. arXiv:cond-mat/0411174, 2004

[28] J. Koch, T. M. Yu, J. Gambetta, A.A. Houck, D.I. Schuster, J. Majer, A. Blais, M.H. Devoret, S.M. Girvin, and R.J. Schoelkopf. Charge-insensitive qubit design derived from the Cooper pair box. Phys. Rev. A, 76:042319, 2007

[29] R.G. Hulet, E.S. Hilfer, and D. Kleppner. Inhibited Spontaneous Emission by a Rydberg Atom. Phys. Rev. Lett., 55:2137-2140, 1985

[30] E.M. Purcell. Spontaneous Emission Probabilities at Radio Frequencies. Phys. Rev., 69:681, 1946

[31] W.E. Lamb and R.C. Retherford. Fine Structure of the Hydrogen Atom by a Microwave Method. Phys. Rev., 72:241-243, 1947

[32] J.M. Fink, M. Goeppl, M. Baur, R. Bianchetti, P.J. Leekm A. Blais and A. Wallraff. Climbing the Jaynes-Cummings ladder and observing its $\sqrt{n}$ nonlinearity in a cavity QED system. Nature (London), 454:315-318, 2008

[33] A. Fragner, M. Goeppl, J.M. Fink, M. Baurm R. Bianchetti, P.L. Leek, A. Blais, A. Wallraff. Resolving Vacuum Fluctuations in an Electrical Circuit by Measuring the Lamb Shift. Science, 322:1357-1360, 2008

[34] http://www.eccosorb.com/Collateral/Documents/English-US/CR.pdf

[35] C. Eichler, et al. In preparation.

[36] L. Steffen, Y. Salathe, M. Oppliger, P. Kurpiers, M. Baur, C. Lang, C. Eichler, G. Puebla-Hellmann, A. Fedorov and A. Wallraff. Deterministic quantum teleportation with feed-forward in a solid state system. Nature, 500:319-322, 2013

[37] M. Stobińska, G. Alberg and G. Leuchs. Perfect excitation of a matter qubit by a single photon in free space. Euro. Phys. Lett., 86:14007, 2009

[38] S. Ritter, C. Nölleke, C. Hahn, A. Reiserer, A. Neuzner, M. Uphoff, M. Mücke, E. Figueroa, J. Bochmann and G. Rempe. An elementary quantum network of single atoms in optical cavities. Nature, 484:195-200, 2012

[39] A.N. Korotkov. Flying qubits with nearly perfect transfer efficiency. Phys. Rev. B, 84:014510, 2011

[40] Y. Yin, Y. Chen, D. Sank, P. J. J. O'Malley, T. C. White, R. Barends, J. Kelly, E. Lucero, M. Mariantoni, A. Megrant, C. Neill, A. Vainsencher, J. Wenner, A. N. Korotkov, A. N. Cleland, and J. M. Martinis. Catch and Release of Microwave Photon States. Phys. Rev. Lett., 110:107001, 2013

[41] S. J. Srinivasan, A. J. Hoffmann, J. M. Gambetta, and A. A. Houck. Tunable Coupling in Circuit Quantum Electrodynamics Using a Superconducting Charge Qubit with a V-Shaped Energy Level Diagram. Phys. Rev. Lett., 106:083601, 2011

[42] S. J. Srinivasan, N. M. Sundaresan, D. Sadri, Y. Liu, J. M. Gambetta, T. Yu, S. M. Girvin and A. A. Houck. Time-Reversal Symmetrization of Spontaneous Emission for High Fidelity Quantum State Transfer. arXiv:1308.3471v1, 2013

[43] M. Pechal, C. Eichler, S. Zeytinoğlu, S. Berger, A. Wallraff, and S. Filipp. Microwave-controlled generation of shaped single photons in circuit quantum electrodynamics. arXiv:1308.4094, 2013

[44] S. Zeytinoğlu, M. Pechal, S. Berger, A. A. Abdumalikov, A. Wallraff and S. Filipp. In preparation.

[45] C. W. Gardiner and M. J. Collett. Input and output in damped quantum systems: Quantum stochastic differential equations and the master equation. Phys. Rev. A, 31:3761-3774, 1985

[46] P. Zoller and C. W. Gardiner. Quantum Noise in Quantum Optics: the Stochastic Schroedinger Equation. arXiv:quant-ph/9702030, 1997

[47] J. M. Martinis, K. B. Cooper, R. McDermott, M. Steffen, M. Ansmann, K.D. Osborn, K. Cicakm S. Oh, D. P. Pappas, R. W. Simmondsm and C. C. Yu. Decoherence in Josephson Qubits from Dielectric Loss. Phys. Rev. Lett., 95:210503, 2005

[48] J. M. Martinis, M. Ansmann, and J. Aumentado. Energy Decay in Superconducting Josephson-Junction Qubits from Nonequilibrium Quasiparticle Excitations. Phys. Rev. Lett., 103:097002, 2009

[49] G. Catelani, S. E. Nigg, S. M. Girvin, R. J. Schoelkopf, and L. I. Glazman. Decoherence of superconducting qubits caused by quasiparticle tunneling. Phys. Rev. B, 86:184514, 2012

[50] J. Brendel, N. Gisin, W. Tittel, and H. Zbinden. Pulsed Energy-Time Entangled Twin-Photon Source for Quantum Communication. Phys. Rev. Lett., 82:2594-2597, 1999

[51] N. Roch, M. E. Schwartz, F. Motzoi, C. Macklin, R. Vijay, A. W. Eddins, A. N. Korotkov, K. B. Whaley, M. Sarovar, and I. Siddiqi. Observation of measurement-induced entanglement and quantum trajectories of remote superconducting qubits. arXiv:1402.1868, 2014

[52] H.-J. Briegel, W. Dür, J. I. Cirac, and P. Zoller. Quantum Repeaters: The Role of Imperfect Local Operations in Quantum Communication. Phys. Rev. Lett., 81:5932-5935, 1998

[53] V. E. Manucharyan, J. Koch, L. I. Glazman, M. H. Devoret. Fluxonium: Single Cooper-Pair Circuit Free of Charge Offsets. Science, 326:113-116, 2009

Acknowledgements

First of all, I would like to thank Prof. Dr. Andreas Wallraff for giving me the opportunity to join the Quantum Device Lab to conduct my Master's Thesis. He offered me the chance to work on state of the art research in the fascinating field of Quantum Computation and Communication, for which I am truly thankful.

My greatest thanks go to my supervisor Marek Pechal for his support and patience to answer all my questions. He introduced me to the world of photon shaping and spent a lot of time helping me to understand quantum optics as well as setting up the measurements. I had a great time working with him and enjoyed the various discussions about interesting (physical) problems.

Not only for fabricating our qubits, but also for helping me with their design, I would like to thank Dr. Farruh Abdumalikov, who in addition was always willing to help me with theoretical and experimental problems. Furthermore, I am very grateful to Dr. Stefan Filipp for the discussions and the advice he gave me throughout my work as well as for asking the right questions to make me think about what I was doing. The same is true for Dr. Christopher Eichler, who developed the parametric amplifier used for this work and did the photo lithography for our samples.

For helping me with the various Cleansweep and FPGA problems, I would really like to thank Yves Salathé, who has spent a lot of time, searching for the right solutions. I am also thankful to Anna Hambitzer, who shared the fridge with me and was willing to get up at crazy times to efficiently use the measurement time.

Moreover, everybody in the group, but especially my office D17, helped me to enjoy my time in the Lab and I am happy for getting the chance to work with all of you.

My special thanks go to my family for supporting me throughout the whole time and for keeping me grounded. I am really happy that we are all still so close to each other. Not to forget all my friends in Switzerland and Germany, who always helped me to enjoy my stay and to relax from time to time.

Last but not least, I want to thank the Foundation of German Business (*Stiftung der Deutschen Wirtschaft*), for their support, which gave me the opportunity to study at ETH Zurich.

ETH

Eidgenössische Technische Hochschule Zürich
Swiss Federal Institute of Technology Zurich

Declaration of originality

The signed declaration of originality is a component of every semester paper, Bachelor's thesis, Master's thesis and any other degree paper undertaken during the course of studies, including the respective electronic versions.

Lecturers may also require a declaration of originality for other written papers compiled for their courses.

I hereby confirm that I am the sole author of the written work here enclosed and that I have compiled it in my own words. Parts excepted are corrections of form and content by the supervisor.

Title of work (in block letters):

Design and characterization of a two sample setup for photon shaping

Authored by (in block letters):

For papers written by groups the names of all authors are required.

Name(s):	**First name(s):**
Huthmacher	Lukas

With my signature I confirm that

- I have committed none of the forms of plagiarism described in the 'Citation etiquette' information sheet.
- I have documented all methods, data and processes truthfully.
- I have not manipulated any data.
- I have mentioned all persons who were significant facilitators of the work.

I am aware that the work may be screened electronically for plagiarism.

Place, date	**Signature(s)**
Zurich, 28.03.2014	L. Huth

For papers written by groups the names of all authors are required. Their signatures collectively guarantee the entire content of the written paper.